



Alcock, Benjamin Thomas (2018) *Solar electron and radio propagation in the turbulent solar corona*. PhD thesis.

<https://theses.gla.ac.uk/9013/>

Copyright and moral rights for this work are retained by the author

A copy can be downloaded for personal non-commercial research or study, without prior permission or charge

This work cannot be reproduced or quoted extensively from without first obtaining permission in writing from the author

The content must not be changed in any way or sold commercially in any format or medium without the formal permission of the author

When referring to this work, full bibliographic details including the author, title, awarding institution and date of the thesis must be given

Enlighten: Theses

<https://theses.gla.ac.uk/>
research-enlighten@glasgow.ac.uk

Solar Electron and Radio Propagation in the Turbulent Solar Corona

Benjamin Thomas Alcock, M.Phys.

Astronomy and Astrophysics Group
School of Physics and Astronomy
Kelvin Building
University of Glasgow
Glasgow, G12 8QQ
Scotland, U.K.



University
of Glasgow

Presented for the degree of
Doctor of Philosophy
The University of Glasgow
January 2018

This thesis is my own composition except where indicated in the text.
No part of this thesis has been submitted elsewhere for any other degree
or qualification.

Copyright © 2018 by Benjamin Alcock

April 23, 2018

To Jenni, Mum, Dad, and Jeff.

Abstract

During a solar flare, ambient electrons are accelerated up to extremely high energies, producing a myriad of electromagnetic emission. Downwards travelling electron beams generate Hard X-rays (HXR) via interactions with the dense chromospheric plasma, while upwards propagating beams generate Langmuir waves which, in turn, cause the production of type-III radio emission. This thesis is concerned with analysing observations and simulations of flare emission in order to learn about both the accelerated beam and the medium through which it travels. Firstly, a comparison of in-situ detections of flare-accelerated electrons and inferred solar electrons is made, revealing differences in the populations. Electron transport along a turbulent magnetic field is simulated, and for the first time we find that, using constraints from HXR data, we are able to match simulations to observations at 1 AU. Secondly, the effects of small and large-scale density inhomogeneities on the passage of low-frequency (32 MHz) radio photons is investigated. Monte-Carlo radio ray tracing simulations are used, and images from an observer at 1 AU are created. The effects of different heliospheric density and scattering profiles on produced images are analysed, and output images are compared to recent radio imaging results. We find that significant fluctuation and asymmetry levels produce apparent motion and growth of imaged radio sources, matching observations. Finally, we use multi-spacecraft observations to locate the emission sources of several heliospheric (≤ 2 MHz) radio bursts. Significant enhancement of the source emission distance compared with predictions is found, and ray tracing simulations are used to model this. We find that significant density fluctuations in the heliosphere are able to produce outwards shifts of apparent sources, in good agreement with observations.

Contents

List of tables	v
List of figures	vi
Preface	ix
Table of Symbols	xi
1 Introduction	1
1.1 The Sun	2
1.1.1 Solar Interior	2
1.1.2 Solar Atmosphere	3
1.2 Solar Flares	4
1.2.1 Particle Acceleration	5
1.3 Hard X-ray Emission	8
1.3.1 Thermal Emission	11
1.3.2 Non-Thermal Thick-Target Emission	11
1.3.3 Non-Thermal Thin-Target Emission	12
1.3.4 HXR Spectral Evolution	13
1.4 Radio Emission	13
1.4.1 Beam-Plasma Interactions	14
1.4.2 Wave-Wave Interactions	16
1.4.3 Radio Observations	17
1.5 The Interplanetary Medium	25
1.5.1 Magnetic Field	25

1.5.2	Electron Density	26
1.6	Particle and Wave Transport in the Heliosphere	29
1.6.1	Particle Propagation Through a Magnetic Field	29
1.6.2	Wave Propagation Through a Plasma	30
1.6.3	Ray Tracing	32
1.7	Instrument Overview	35
1.7.1	Wind	35
1.7.2	STEREO	37
1.7.3	RHESSI	37
2	Pitch Angle Scattering of Flare Electrons in the Inner Heliosphere	41
2.1	Background	41
2.2	Event Selection and Data Analysis	44
2.2.1	Electron Analysis	45
2.2.2	HXR Spectral Analysis	47
2.3	Interplanetary Transport of Flare Electrons	49
2.3.1	Transport Model	51
2.3.2	Injection Profile	53
2.3.3	Numerical Scheme	54
2.4	Numerical Simulation Verification	55
2.4.1	Diffusion Term	56
2.4.2	Source Term	56
2.4.3	Focusing Term	59
2.5	Model Comparison and Results	60
2.5.1	Time-Intensities	61
2.5.2	Spectral Shifts	68
2.5.3	Average Scattering Properties	70
2.6	Summary	71

3	Studying the Time Evolution of a Low-Frequency Type-IIIb Radio Source	73
3.1	A Typical Type-III Burst	73
3.1.1	Typical Burst Features	73
3.1.2	Typical Electron Properties	75
3.2	Type-IIIb Background	76
3.3	LOFAR Overview	78
3.4	16 th of April 2015 Event	78
3.5	Testing the Effects of Scattering	81
4	Ray Tracing Simulations of Solar Radio Bursts in the Corona	83
4.1	Background	83
4.2	Ray Tracing Scheme	85
4.2.1	Numerical Scheme	86
4.2.2	Initial Source Parameters	87
4.2.3	Background Density Model	89
4.2.4	Asymmetric Density Models	90
4.2.5	Density Fluctuation Model	92
4.2.6	Anisotropy	93
4.2.7	Absorption	94
4.3	Results	96
4.3.1	Simulation Verification	96
4.3.2	Imaging Scheme	98
4.3.3	Centroid and Area Variation	98
4.4	Summary and Conclusions	107
5	Multilateration of Observed and Simulated Low-Frequency Type-III Radio Burst Sources	110
5.1	Background	110
5.2	Multilateration Technique	112

5.3	Data Analysis	114
5.3.1	Event Selection and Radio Analysis	114
5.3.2	Positioning the Sources	116
5.3.3	Beam Speed	117
5.4	Monte Carlo Simulations	118
5.5	Results and Discussion	120
5.5.1	Density Model Comparison	120
5.5.2	Excitor Speed	122
5.6	Summary and Conclusions	126
6	Conclusions	132
6.1	Electron Transport and Scattering	132
6.2	Coronal Radio Imaging	134
6.3	Heliospheric Radio Multilateration	136
6.4	Closing Statement	137
	Bibliography	139

List of tables

1.1	Table listing instruments used within this thesis, showing particle species and energy/ frequency range covered.	35
5.1	Average beam speeds calculated for all events. Uncertainties are given by the standard error.	123

List of figures

1.1	Bremsstrahlung diagram	10
1.2	Solar radio emission distances. From Gary & Hurford (1989)	14
1.3	Langmuir wave generation	15
1.4	Solar radio classifications. From Dulk (1985)	18
1.5	Example type-III burst	19
1.6	Solar radio images at different frequencies	23
1.7	Coronal density profiles	27
1.8	Ray tracing description	33
2.1	Electron dropouts observed by Wind on the 20 th of February 2002.	46
2.2	Time delay methods calculated for the 25 th of April 2002 event.	48
2.3	RHESSI photon flux (with thick target fit) and inferred electron spectrum.	50
2.4	Soft-hard-soft velocity spectral index example.	55
2.5	Analytical and numerical comparisons for a simplified pitch-angle scattering model.	57
2.6	Analytical and numerical comparisons for an advection equation with source term.	58
2.7	Analytical and numerical comparisons for a focussed diffusion equation.	59
2.8	Overview plots for impulsive events.	63
2.9	Overview plots for impulsive events.	64
2.10	Overview plots for impulsive and gradual events.	65
2.11	Overview plots for gradual events.	66
2.12	Delay timing comparison for all events.	67

2.13	Background subtracted peak-flux electron spectra comparisons for all events.	69
2.14	Simulation parameter box plot.	70
3.1	Example type-III (Reid & Kontar, 2017) and type-IIIb bursts (Kontar et al., 2017).	74
3.2	Type-IIIb striae profiles, from Kontar et al. (2017).	79
3.3	Type-IIIb source parameters observed during the 2015-04-16 event. From Kontar et al. (2017).	81
4.1	Emission patterns for fundamental rays.	88
4.2	Coronal density model comparison.	90
4.3	Asymmetric coronal density models.	91
4.4	Scattering strength as a function of distance from the source and fluctuation level.	93
4.5	Anisotropic \mathbf{k} -vector geometry.	95
4.6	Comparison of analytical and numerical ray wavenumber values.	97
4.7	Rays showing the passage of multiple photons through plasmas with varying levels of density fluctuations.	99
4.8	Imaging scheme geometry used in simulations.	100
4.9	Time-slice images, showing fitted gaussian parameter variation.	101
4.10	Source parameter variation with fluctuation level.	103
4.11	Centroid shift as a function of viewing angle.	104
4.12	Comparison of isotropic and anisotropic scatter images.	106
4.13	Image snapshots for asymmetric density + isotropic scattering, showing fitted source size and distance changes.	108
5.1	Spacecraft and radio source positions.	113
5.2	Example sources located using TDOA method.	115
5.3	Dynamic spectra for STEREO-A/B and Wind, and fitted normalised intensity in separate frequency channels.	116

5.4	Radio source positions for the 2011-11-23 event.	117
5.5	Electron beam speed comparison for the 2014-05-27 event.	119
5.6	Comparison of Type-III source distances for the 2011-11-23 event with density models.	121
5.7	Simulated Type-III source locations for a density fluctuation level of 4%.	122
5.8	Comparison of median Type-III source distances with predictions from density models.	123
5.9	Simulated dynamic spectra for several scattering levels.	125
5.10	Simulated dynamic spectra for several viewing angles.	127
5.11	Simulated electron beam speed obtained via multilateration.	128
6.1	Apparent source area as a function of frequency.	136

Preface

This thesis deals with study of the effects of small and large scale magnetic and density fluctuations on the propagation of solar flare accelerated electrons, and subsequently emitted radio waves. Particular focus is paid on replicating observed phenomena, such as shifted electron peak-flux spectra, motion of imaged sources, and delaying of radiation arrival at Earth.

Chapter 1 begins with a brief overview of the Sun and particle acceleration within a solar flare, before focussing on the physics of the generation of X-ray and type-III radio emission. A short review of solar radio emission is given, describing the different types of emission and several imagers used to study them. The mathematical framework for modelling the passage of flare accelerated electrons and radio waves through the heliosphere is described, before concluding with a short description of instruments used within this work.

Chapter 2 introduces observations of electron populations which feature differences with respect to expectations from solar electromagnetic emission. Observations are analysed to determine parameters of the electron populations, and simulations of > 27 keV electron transport from a Sun to a near-Earth spacecraft are described. The chapter then looks at the different scattering parameters required to best match observations, and concludes by determining some average transport properties.

Chapter 3 is an overview of recent radio observations. The chapter begins with a short description of a typical type-III burst, before moving on to discuss a feature commonly observed in type-III bursts. The findings of a recent paper are then summarised, with the main questions raised by the paper outlined.

Chapter 4 then works to replicate the findings of this paper via simulations of radiowave transport through the heliosphere. The physical and mathematical framework of radio transport through a fluctuating medium is discussed, and the effects of small and large scale density features on resultant observations are analysed. The chapter ends with a discussion of the density models which best match observations.

Chapter 5 moves further from the Sun, looking at tracking solar radio emission sources as they travel through the corona. A method to locate the source of emission with multiple spacecraft is described, and applied to multiple events in order to find statistical trends. Simulations of low-frequency burst transport are then employed to determine the background properties of the corona, through which the radiowaves pass.

Chapter 6 concludes the thesis by briefly discussing the findings of each chapter, before looking with greater depth at the effects of the research presented within this thesis on the field as a whole. The chapter ends by discussing future directions which can be applied to this work, with regard to planned spacecraft missions.

Table of Symbols

Unless explicitly stated, all quantities within this thesis are quoted in *cgs* units.

$f(t, z, \mu, v)$	1D Electron phase space density [$e^- \text{ s}^{-1} \text{ cm}^{-1} (\text{cm s}^{-1})^{-1}$] (Chapter 2)
$D_{\mu\mu}$	1D pitch-angle diffusion coefficient [s^{-1}] (Chapter 2)
λ_{\parallel}	Parallel mean-free path [cm] (Chapter 2)
θ	Electron pitch-angle: the angle between an electron's velocity vector and magnetic field [rad] (Chapter 2)
μ	Electron pitch-angle cosine ($\mu = \cos \theta$; Chapter 2)
f_{pe}, ω_{pe}	Electron plasma frequency [MHz] and angular plasma frequency [10^6 rad s^{-1}] (Chapter 4 & 5)
n_e	Electron plasma density [cm^{-3}] (Chapter 4 & 5)
ρ	Plasma refractive index (Chapter 4)
$r, \mathbf{r}(x, y, z)$	Ray position and position vector [cm] (Chapter 4 & 5)
$k, \mathbf{k}(x, y, z)$	Wavenumber and wavevector [cm^{-1}] (Chapter 4 & 5)
T_x, T_y, T_z	Cartesian ray direction cosine components (Chapter 4)
k_B	Boltzmann's constant [erg K^{-1}]
T_e	Electron temperature [K]
m_e	Electron mass [g]
c	Speed of light in a vacuum [cm s^{-1}]
G	Newton's gravitational constant [$\text{cm}^3 \text{ g}^{-1} \text{ s}^2$]
e	Electron charge [esu]

Chapter 1

Introduction

In the year 774 AD, the Anglo-Saxon Chronicle notes that *“This year the Northumbrians banished their king, Alred, from York at Easter-tide; and chose Ethelred, the son of Mull, for their lord, who reigned four winters. **This year also appeared in the heavens a red crucifix, after sunset; the Mercians and the men of Kent fought at Otford; and wondrous serpents were seen in the land of the South-Saxons.**”* (Ulwencreutz, 2008). Undoubtedly, the cause of this sighting could not be fully understood at the time; however, by studying the abundances of different isotopes present in bodies from this period the causes can now be determined.

Studies of carbon-14 abundances in Japanese cedar trees (Miyake et al., 2012), German oak trees (Usoskin et al., 2013) and beryllium-10 abundances in Antarctic ice cores (Usoskin et al., 2013) revealed large spikes¹ in isotope abundance around 774-5 AD. Analysis of further isotopes commonly produced in solar-terrestrial events (Mekhaldi et al., 2015) have led to the hypothesis that both the large increases in isotope abundance and the (possibly auroral) sightings in England and across Europe could have been caused by an extremely strong solar flare.

Climate models have demonstrated that an event of this scale could affect the mean temperature by $\sim 2 - 3$ K in the northern hemisphere winters (Sukhodolov et al., 2017); although this effect would be regional, and would only last for around a

¹Around 20 times the background carbon-14 level.

year. However, given continuous technical advancement and the increasingly complex technology used today, a similarly large event occurring now would have drastic effects on Earth's satellite system; radio and wireless systems; airlines; power networks; and pipelines (Daglis, 2005). As such, understanding the origin of, transport to, and impact of solar radiation at Earth is of vital importance.

The subject of this thesis is the observation and modelling of the products of solar flares; namely, high energy (> 27 keV) electrons measured near Earth, hard X-ray (HXR) bursts produced at the Sun, and type-III radio bursts generated in interplanetary space. Large and small scale variations in both the solar magnetic field and the background plasma density affect the transport of these particles and waves, leading to a different distribution observed at 1 AU to that present within the solar flare. In this chapter, we introduce the basic physical mechanisms in solar flares, before looking further into the acceleration and release of electrons during the flare. The generation of HXR and type-III bursts are described, and the subsequent transport and scattering of the flare electrons and electromagnetic waves through the Interplanetary Medium (IPM) are explained. Finally, a brief overview of the instrumentation and data analysis tools used in this thesis is given.

1.1 The Sun

The source of a large fraction of the radiation experienced at Earth, the Sun is an incredibly complex body. Here, the structure of the solar interior and exterior (atmosphere) shall be briefly introduced, in order to explain the acceleration and subsequent generation of high energy particles and electromagnetic waves.

1.1.1 Solar Interior

The Sun's interior can be described by multiple distinct layers, each representing a different temperature and pressure domain. At the centre is the core, extending to around $0.25 R_{\odot}$ with a density of $\sim 150 \text{ g cm}^{-3}$ (Stix, 2004) and temperatures of up

to 15 MK (Reames, 2017). Due to the extremely high pressures within the solar core, the bulk of the Sun’s energy is released here², which rises upwards through the solar interior to the Sun’s surface. Outside of the core lies the radiative zone, stretching from the edge of the core to $\sim 0.7R_{\odot}$. Here, the energy released in the core is transferred closer to the Solar surface via radiation. The density and temperature both drop to around 0.2 g cm^{-3} and 2 MK (Ambastha, 2010), respectively. Within the radiative zone, there is near-uniform rotation rates at every solar latitude.

At the edge of the radiative zone, once the density and temperature drop to low enough levels that radiation is insufficient to transfer the energy of the core outwards, lies the tachocline. This thin layer (around $0.04 R_{\odot}$ thick) separates the radiative zone from the convection zone, where the poles rotate at a much slower angular rate than the solar equator. This difference in rotation regimes causes a large shear force in the tachocline, potentially building up the Sun’s magnetic field to extremely high levels (Thompson et al., 1996).

The final region of the solar interior is the convection zone, occupying the final $\sim 0.3R_{\odot}$ of the interior (Rempel, 2011). Within this region, the dominant method of energy transfer from the core to the surface is convection of plasma. As the plasma rises from the tachocline, it takes the magnetic field with it and drags it upwards to the solar surface (Rempel, 2011), where it rises outwards to the solar atmosphere.

1.1.2 Solar Atmosphere

The solar atmosphere is defined at the photosphere - the visible surface of the Sun, named from the Greek word photos (meaning “light”). Here the temperature is around 4000 – 6000 K, with a hydrogen number density of around 10^{16} cm^{-3} (Machado et al., 1978). Upwards of the photosphere is the chromosphere, so named because of the red $H\alpha$ emission visible to the naked eye during solar eclipses (from the Greek word “chroma”, meaning colour). Around 2000 km thick and comprised mostly of hydrogen

²Assuming the Sun’s luminosity arises primarily from nuclear processes within the core, the energy release is $\sim 4 \times 10^{33}$ ergs every second (Kippenhahn et al., 2012).

and helium, the chromospheric temperature slowly rises to around 2×10^4 K at the top of the chromosphere, while the electron density rapidly drops from 10^{15} cm^{-3} to around 10^{11} cm^{-3} . Due to the increasing temperature, the level of ionisation of hydrogen and helium atoms increases closer to the chromospheric surface.

Above the chromosphere sits the transition region; a thin (~ 200 km thick) region which separates the chromosphere from the upper solar atmosphere - the corona. The temperature of the transition region rises rapidly to over 1 MK and the electron density drops to around 10^9 cm^{-3} . While the cause of this extreme temperature rise is still not fully understood, its effects are clear to see: below the transition region helium is partially ionised and gravity dominates the motion and shape of structure, whereas above the transition region helium becomes fully ionised, and magnetic forces dominate the motion and shapes of structures (Stix, 2004).

The solar corona extends outwards from the edge of the transition region to interplanetary space, where the solar wind and Coronal Mass Ejections (CMEs) transport solar particles away from the Sun. As the Sun rotates, magnetic field lines get pulled out into a spiral shape called the Parker Spiral, along which particles ejected from solar flares travel.

Due to the differing temperature and pressure regimes at every height of the solar atmosphere, a variety of emission and absorption mechanisms allow photons of varying energies to be seen across the atmosphere. Thus, by properly understanding the heights at which specific frequencies are formed, the entire atmosphere can be probed down to the solar surface.

1.2 Solar Flares

Solar flares are extremely energetic magnetic reconfigurations, occurring impulsively in the Solar atmosphere (Priest & Forbes, 2002; Benz, 2008). As described above, the Solar magnetic field is anchored in the convection zone, and extends upwards into the corona. As the magnetic footpoints are moved about in the turbulent convective zone, the field is twisted and sheared, building up and storing energy. Eventually a critical

energy threshold will be reached, at which time the magnetic field will reconfigure to a simpler state, releasing a huge amount of energy (up to 10^{32} ergs; [Shibata & Magara, 2011](#)) in a short time and within a localised region in the Solar Corona. In the energy release region (the acceleration region), around 5–50% of the stored magnetic energy can go into accelerating the ambient plasma to extremely high velocities ([Emslie et al., 2004, 2012](#); [Aschwanden et al., 2017](#)).

1.2.1 Particle Acceleration

Once the energy has been released from the magnetic field, a large portion of it goes into accelerating the plasma present in the acceleration region. Due to having $\sim 1/1836^{\text{th}}$ of the mass of a proton, the local electron population is accelerated to relativistic and near-relativistic velocities. There are three main modes for particle acceleration during solar flares, which are: Direct Current (DC) electric field acceleration, shock acceleration, and stochastic acceleration. As the focus of this thesis is on the transport of particles *after* acceleration, the acceleration processes shall only briefly be mentioned here, and a more thorough overview can be found in [Aschwanden \(2005\)](#).

DC Electric Field Acceleration

DC field acceleration models can be broadly divided by the electric field strength, the magnetic geometry surrounding the field, and the time variability of the electric field itself ([Aschwanden, 2005](#)). When situated in a DC field, electrons and ions become accelerated in different directions. If the velocities of the accelerated particles reach a high enough level, then the accelerating force will dominate over any collisional damping forces, and the particles will experience runaway acceleration - resulting in particles of superthermal velocities. The Dreicer electric field is given as (e.g. [Holman, 1985](#)),

$$E_D = \frac{e \ln \Lambda}{\lambda_D^2}, \quad (1.1)$$

where e is the electron charge, $\lambda_D = v_{Te}/\omega_{pe}$ is the electron Debye length, and

$\ln \Lambda = \ln |\lambda_D/b_{min}|$ is the Coulomb logarithm, accounting for all possible deflections of an electron off of an ion with distances of closest approach between b_{min} and λ_D .

Acceleration of particles by DC fields weaker than this limit (*Sub-Dreicer* DC fields) requires an extremely large distance (~ 10 Mm) over which particles are accelerated. This large distance is required to ensure that enough of the particle distribution experiences runaway acceleration, producing the observed HXR emission. Models of sub-Dreicer fields have been applied to solar flares by [Holman \(1985\)](#), but there are some problems with sub-Dreicer acceleration models. Firstly, long current sheets are unstable to tearing mode instabilities, and so would break down rapidly. Sub-Dreicer fields would also show a larger delay in acceleration for the highest energy particles compared to lower energy particles due to the slow gain in particle energy, while little delay is observed ([Aschwanden, 2005](#)). If the field energy is above the Dreicer limit (*Super-Dreicer* DC fields), then all particles with velocities above the thermal velocity experience runaway acceleration. Within this model, much shorter distances are required for particle acceleration, due to the higher fraction of the particle population being accelerated.

As stated above, DC fields can also be generated around regions of magnetic reconnection. Acceleration near a magnetic X-point has been studied extensively in the context of both Sweet-Parker type current sheets and Petschek type current sheets. Acceleration of particles near X-points has been shown to form a powerlaw in the particle energy spectrum (e.g. [Fletcher & Petkaki, 1997](#); [Zharkova & Gordovskyy, 2005](#); [Wood & Neukirch, 2005](#)), as seen observationally. One downside of X-point acceleration models are the extremely high electric field strengths required to accelerate particles within a short time, due to the difficulty of magnetically trapping particles.

A consequence of the tearing-mode instability in long (e.g. Sweet-Parker style) current sheets is the formation of magnetic islands - called magnetic O-points ([Furth et al., 1963](#)). Acceleration can occur surrounding these O-points (see [Kliem, 1994](#); [Gontikakis et al., 2007](#); [Gordovskyy et al., 2010](#), for example), and due to the geometry of the magnetic field the rate of particle trapping is increased, allowing for acceleration of particles to relativistic energies even with reduced electric field strengths.

Stochastic Acceleration

Another method by which particle acceleration can occur is via stochastic acceleration by the magnetic field component of low-frequency magneto-acoustic waves (Miller et al., 1997; Schlickeiser & Miller, 1998; Zharkova et al., 2011). Originally proposed by Fermi (1949), this model describes particle scattering from agents moving towards each other with velocities $\pm v_a$, gaining velocity $2v_a$. If L is the separation of the scattering centres, and v is the particle velocity, then the particle acceleration rate is $a \approx 2v_a/(L/v)$. Assuming that the scattering happens on a short enough timescale that L remains roughly constant, the particle energy can be seen to grow exponentially with time, as $E \approx 1/2m_e e^{4v_a t/L}$. This cohesive acceleration process is called *first-order Fermi acceleration*. If the scattering agents are moving randomly rather than coherently, then particles can experience both energy loss and energy gain. Due to the random nature of the scattering, there is still a net increase in particle energy for a fraction of the population, proportional to $(v_a/v)^2 D_{\mu\mu}$. Here $D_{\mu\mu}$ is the diffusion coefficient, describing the diffusion of the population due to multiple small-scale scatterings (§1.6.1). This second case is called *second-order Fermi acceleration*.

Within a solar flare, there are two sources of scattering agent: cascading MHD turbulence (Miller et al., 1996), or plasma wave turbulence (Hamilton & Petrosian, 1992; Pryadko & Petrosian, 1997, 1998, 1999). In the MHD turbulence model, the scattering agents are constituted of magnetic compressions created by fast-mode MHD waves, which propagate at an angle to the magnetic field. Within some inertial, range the MHD turbulence cascades from low to high wavenumber, and particle resonance with any wave will result in an energy transfer between the particle and the waves, putting the particle in resonance with a neighbouring wave (Miller et al., 1996). Through this mechanism, electrons can easily be accelerated from pre-flare thermal energies up to relativistic energies in a continuous spectrum.

The second form of stochastic acceleration occurs from plasma wave turbulence, where a presupposed level of turbulence in the ambient plasma accelerates the particles up to high energies. This model has both advantages and disadvantages over DC field

acceleration. One advantage is that very short timescales are required to accelerate particles to high energies, well matching predictions from X-ray observations. However, a draw-back of the model is the lack of radio observations from the flare site, which would be predicted from plasma waves decaying into transverse radio waves.

Shock Acceleration

In a similar manner to Stochastic Acceleration, particles can also be accelerated via repeated magnetic mirrorings off a travelling shock wave. If the particles pass the shock front a single time then this is a form of *first-order Fermi acceleration*, but if the shock front is more diffuse (meaning that particles scatter back and forth over the shock) then Shock Acceleration is a form of *second-order Fermi acceleration*. Although particle energy gains and losses are possible, [Fermi \(1949\)](#) argued that the increased probability of a “head-on” collision between a particle and the shock front meant that a net gain in particle energy occurs. Termination shocks have been observed in solar flares by [Chen et al. \(2015\)](#), and have been shown to produce a power-law spectrum by e.g. [Blandford & Ostriker \(1978\)](#); [Cargill \(1991\)](#), consistent with observations.

However, while the presence of shocks is known within flares, and they are able to produce the observed spectrum of non-thermal particles, there is a large shortcoming in shock acceleration models. Shocks are only able to accelerate already high energy particles to relativistic energies, requiring some primary process to produce particles of high enough energies to be accelerated. Although the efficiency of the shock acceleration is increased in quasi-perpendicular (i.e. shock normal is *almost* orthogonal to the shock velocity vector) shocks, there is little evidence for these forms of shocks at the top of flaring loops ([Zharkova et al., 2011](#)).

1.3 Hard X-ray Emission

The main X-ray emission mechanism for photon energies of $\epsilon \sim 10 - 300$ keV is bremsstrahlung emission; the emission of photons from electrons which Coulomb collide with free electrons and ions, and are elastically scattered. Although the two $e - e$ and

$e - i$ emission spectra differ, in this thesis only $e - i$ collisions are considered, as they dominate for beam energies of < 300 keV (Haug, 1975; Kontar et al., 2007).

As a moving electron passes near another electron or an ion, it will be deflected by the other particle's electric field by some angle θ_D (e.g. see Figure 1.1). In the simplest bremsstrahlung model, the travelling electron passes close to a stationary heavy ion. Under the assumption that the ions have a high enough atomic number (Z), the collisional cross-section for small-angle scattering is given by the Rutherford formula

$$\sigma_R = \frac{4\pi Z e^2}{m_e^2 v^4} \int_{b_{min}}^{b_{max}} \frac{db}{b}, \quad (1.2)$$

where v is electron speed, m_e is electron mass, e is the electron charge, Z is the mean ion charge, and b is the closest distance of approach between the electron and the ion, neglecting any scattering. If the travelling electron were to continue undeflected, then the integral would yield

$$\int_{b_{min}}^{b_{max}} \frac{db}{b} = \ln \left| \frac{\lambda_D}{b_{min}} \right| = \ln \Lambda, \quad (1.3)$$

also known as the Coulomb logarithm.

The amount of HXR emission from a flare is proportional to the number of collisions between the source electrons and ions. Hence, the HXR intensity $I(\epsilon)$ (scaled for the $1/r^2$ drop-off at a distance R) is given by

$$I(\epsilon) = \frac{1}{4\pi R^2} \int_{\epsilon}^{\infty} \int_V Q(E, \epsilon) F(E, \mathbf{r}) n(\mathbf{r}) dE d^3\mathbf{r}, \quad (1.4)$$

where $n(\mathbf{r})$ is the plasma number density in the emitting region, $Q(E, \epsilon)$ is the bremsstrahlung emission cross-section, $F(E, \mathbf{r})$ is the electron spectrum as a function of electron energy E and position \mathbf{r} .

For non-relativistic (or near-relativistic) electron-ion bremsstrahlung, there are two commonly used forms of the cross-section, given by the Kramers form (Kramers, 1923),

$$Q(E, \epsilon) = Z^2 \frac{\sigma_0}{E\epsilon}, \quad (1.5)$$

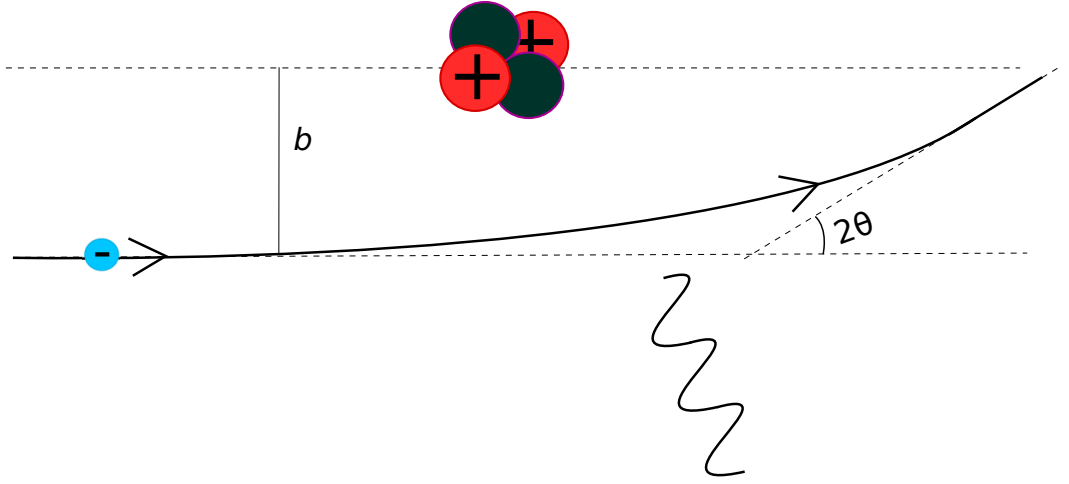


Figure 1.1: An electron Coulomb collides with a heavier ion, emitting a Hard X-Ray due to its change in momentum. The distance of closest approach, neglecting collisional deflections, is denoted by the impact parameter b .

and the Bethe-Heitler cross-section (Bethe & Heitler, 1934),

$$Q(E, \epsilon) = Z^2 \frac{\sigma_0}{E\epsilon} \ln \left| \frac{1 + \sqrt{1 - \frac{\epsilon}{E}}}{1 - \sqrt{1 - \frac{\epsilon}{E}}} \right|. \quad (1.6)$$

Here $\sigma_0 = (8\alpha/3)(m_e c^2)r_0^2 = 7.9 \times 10^{-25} \text{ cm}^2 \text{ keV}$, $\alpha = e^2/(\hbar c) \sim 1/137$ is the fine structure constant, m_e is the electron mass, c is the speed of light, and $r_0 = e^2/(m_e c^2) = 2.82 \times 10^{-13} \text{ cm}$ is the classical electron radius.

Both of these formulae are non-relativistic simplifications of the full cross-section, found as formula 3BN in Koch & Motz (1959). For electrons of energies above ~ 30 keV, relativistic effects must be taken into account (Haug, 1997). An analytic form of the full relativistic cross-section was derived by Haug (1997), and has been used in all fitting of spectra in this thesis.

If we are only concerned with the spectral shape of the event, and not the positional information, then a spatially integrated form of Equation 1.4 can be taken, e.g. Brown (1971)

$$I(\epsilon) = \frac{1}{4\pi R^2} \int_{\epsilon}^{\infty} \langle \bar{n} V \bar{F}(E) \rangle Q(E, \epsilon) dE, \quad (1.7)$$

where $\bar{n} = (1/V) \int_V n(\mathbf{r}) d^3 \mathbf{r}$ is the number of particles per unit volume, and $\bar{F}(E) =$

$(1/\bar{n}V) \int_V n(\mathbf{r})F(E, \mathbf{r})d^3\mathbf{r}$ [$e^- \text{ cm}^{-2} \text{ s}^{-1} \text{ keV}^{-1}$] is the mean electron flux spectrum (Brown et al., 2003). The parameter $\langle \bar{n}V\bar{F}(E) \rangle$ is the density-weighted mean electron flux.

By taking the observed HXR spectrum $I(\epsilon)$, and either forward fitting a cross-section model or inverting Equation 1.7, the value $\langle \bar{n}V\bar{F}(E) \rangle$ can be inferred, and hence the source mean electron spectrum $\bar{F}(E)$ can be calculated. For further reading, Kontar et al. (2011) gives an overview of different methods used to calculate the electron spectrum from the observed photon spectrum.

1.3.1 Thermal Emission

Typically the HXR emission in a flare is from one of two sources, the thermal distribution of electrons, or an additional non-thermal distribution which has reached high energies through the acceleration methods described in Section 1.2.1. The lower energy emission ($< 10 - 20 \text{ keV}$) is usually dominated by emission from an electron distribution in thermal equilibrium, and the HXR emission is best fit with an isothermal exponential function,

$$I(\epsilon, \mathbf{r}) \propto \frac{n^2(\mathbf{r})V(\mathbf{r})}{\epsilon T^{1/2}(\mathbf{r})} e^{-\epsilon/(k_B T(\mathbf{r}))}, \quad (1.8)$$

where T [K] is the average temperature of the emitting electrons, and the value $n^2(\mathbf{r})V$ is also called the emission measure (EM). Converting this to the density-weighted mean electron flux yields the distribution (e.g. Battaglia & Kontar, 2013),

$$\langle \bar{n}V\bar{F}(E) \rangle \propto EM \frac{E}{\sqrt{m_e(k_B T)^3}} e^{-E/(k_B T)}. \quad (1.9)$$

1.3.2 Non-Thermal Thick-Target Emission

Alternatively, HXR emission can come from an electron population accelerated to energies far above the thermal energy. Generally, it is seen that a single or broken power-law can well fit the photon flux above $\sim 20 \text{ keV}$ (e.g. see Holman et al., 2011, for a review). Hence, an observed HXR spectrum of

$$I(\epsilon) \propto \epsilon^{-\gamma}, \quad (1.10)$$

implies a density-weighted mean electron flux spectrum of

$$\langle \bar{n}V\bar{F}(E) \rangle \propto E^{-\delta}, \quad (1.11)$$

where γ and δ are the observed photon and inferred electron spectral indices, respectively. The relationship between the spectral indices depends upon the scattering cross-section chosen, and hence there are two models of HXR emission used in this thesis to determine the solar electron spectral index.

If the target is sufficiently dense, the travelling electrons will lose all of their energy via Coulomb collisions, producing large amounts of non-thermal emission (Brown, 1971). This model is valid for emission from dense areas of the solar atmosphere, such as chromospheric footpoint emission. In this model, the photon spectral index is given as

$$\gamma = \delta + 1. \quad (1.12)$$

1.3.3 Non-Thermal Thin-Target Emission

If the electron beam travels through a much less dense region of the solar atmosphere (e.g. at the top of a coronal loop, near the acceleration region), then the thick-target model is not valid for fitting the observed spectra. Instead, it must be assumed that the beam electrons do not lose all of their energy to the target, and hence continuously produce emission during transport. In the thin-target model, the photon spectral index is given as (e.g. Datlowe & Lin, 1973; Krucker et al., 2007; Battaglia & Benz, 2008)

$$\gamma = \delta - 1. \quad (1.13)$$

1.3.4 HXR Spectral Evolution

During a flare, the non-thermal component of HXR observations generally follows a characteristic *hard-soft-hard* spectral variation, whereby the photon spectrum will flatten near the peak of the flare, before steepening during the declining phase (e.g. Parks & Winckler, 1969; Battaglia & Benz, 2006; Benz, 2008; Holman et al., 2011).

A number of things can affect the HXR spectrum, such as trapping of high energy particles within the coronal loop, changes in the efficiency of the acceleration mechanism, or a change in the ratio of thermal/ non-thermal emission observed (Aschwanden, 2005). While the variation in the relative contributions of thermal/ non-thermal emission can have a large effect on the HXR spectral index at lower energies, Aschwanden (2005) showed that the higher energy spectral index varies by a much smaller amount. Hence, it is likely that any change in spectral index at high X-ray energies is due to an intrinsic property of either the injected electrons, or a change in the acceleration efficiency.

1.4 Radio Emission

Coulomb collisions are not the only method by which travelling electron beams can generate bursts of electromagnetic energy. Propagating electron beams will also produce a myriad of radio emission, classified as either *coherent* or *incoherent* emission (Benz, 2008). Incoherent emission can come in two forms: free-free bremsstrahlung emission at microwave frequencies, or gyroemission produced by electrons gyrating in a magnetic field, while coherent emission can either be produced via plasma emission, or electron cyclotron maser emission. Figure 1.2 shows the characteristic radio frequencies as a function of distance from the photosphere. The primary concern of this thesis is the emission from outwards streaming flare electrons which emit at distances of $> 1R_{\odot}$ from the photosphere. Hence, this research focuses on one form of emission only - *coherent plasma emission*.

Plasma emission is a three-stage process, first proposed by Ginzburg & Zhelezni-

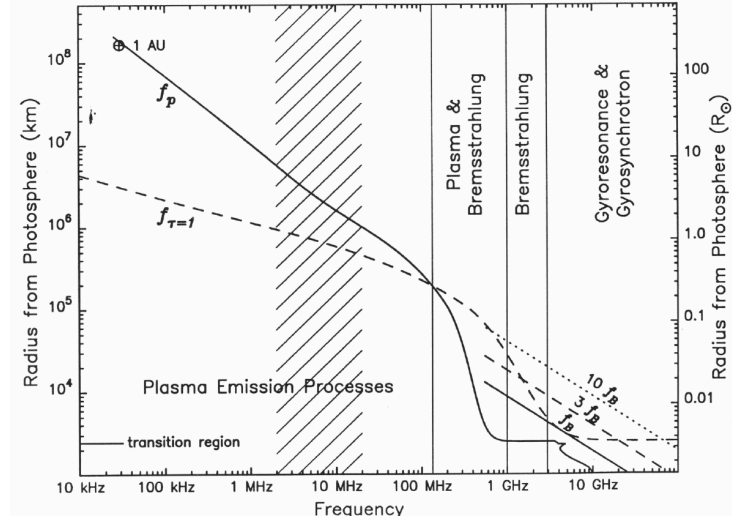


Figure 1.2: Hypothetical distance/ frequency plot of radio emission, showing the different emission types from different locations. From Gary & Hurford (1989).

akov (1958) and subsequently expanded upon by Zheleznyakov & Zaitsev (1970a,b). An overview of the emission mechanism and observations can be found in McLean & Labrum (1985), and here the basic processes will be introduced.

1.4.1 Beam-Plasma Interactions

Particle acceleration in a solar flare occurs in a quasi-collisionless plasma, meaning that velocity dispersion will occur, allowing the higher velocity electrons to move ahead of the slow velocity electrons. This will alter the electron velocity distribution far from the flare site, creating a so-called *bump-on-tail distribution* (see Figure 1.3) (Zheleznyakov & Zaitsev, 1970a,b; Zaitsev et al., 1972; Melrose, 1980b; Reid & Ratcliffe, 2014). Due to the positive gradient in velocity space ($\partial f / \partial v_{\parallel} > 0$ where f is the electron phase space density), this distribution is unstable to the *bump-on-tail instability*, whereby Landau resonance causes the “bump” electrons to lose energy. This causes a plateau in the electron distribution, recycling the lost energy by generating longitudinal plasma oscillations (Langmuir waves; Ginzburg & Zhelezniakov, 1958, see Figure 1.3).

Electron Langmuir waves oscillate at the electron frequency f_{pe} , given by

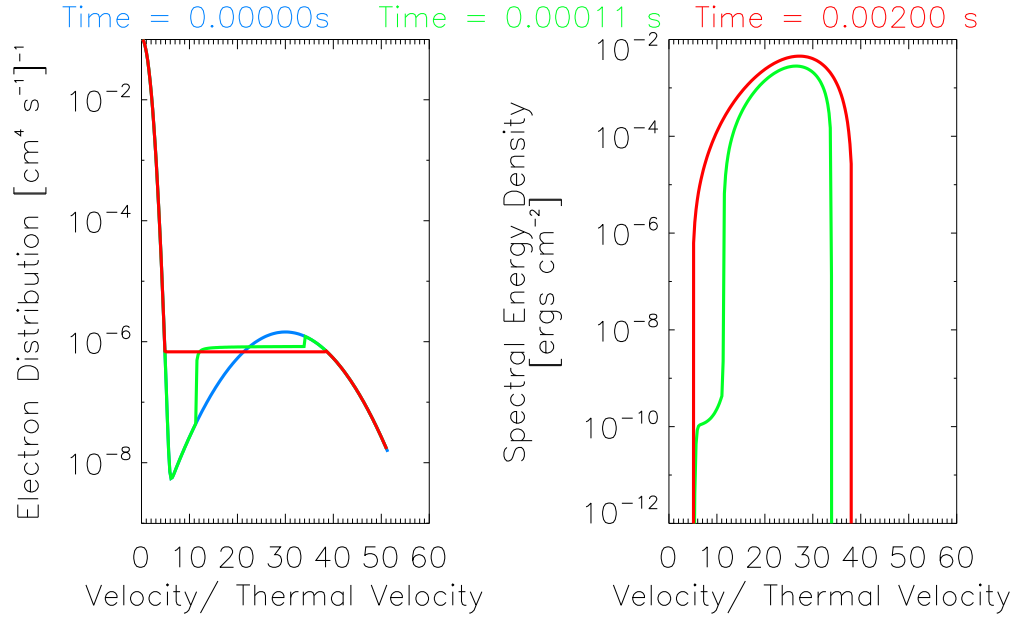


Figure 1.3: **(left)** Electron velocity distribution, showing plateauing of the bump-on-tail distribution with time. **(right)** Langmuir wave spectral energy density distribution, showing growth of wave energy with time. (From H. Reid, personal communication).

$$f_{pe} = \sqrt{\frac{e^2 n_e}{\pi m_e}} \quad (1.14)$$

where n_e is the background electron plasma density. The dispersion relation for Langmuir waves is given by

$$\omega^2 = \omega_{pe}^2 + \frac{3}{2} k^2 v_{th}^2 \quad (1.15)$$

where $\omega = 2\pi f$ is the angular wave frequency, $\omega_{pe} = 2\pi f_{pe}$ is the angular plasma frequency, k is the photon wavenumber, and v_{th} is the electron thermal velocity.

An argument against Langmuir wave generation/collapse being the cause of type-III emission was proposed by [Sturrock \(1964\)](#), and is known as *Sturrock's dilemma*. Assuming that a travelling beam of electrons loses energy to the generation of Langmuir waves at an increasing rate, then at some point the electron beam would have lost all

energy to the waves, and hence could only travel a short distance³. Observations of type-III bursts down to ~ 20 kHz (the plasma frequency at 1 AU) suggest that a different process is causing the type-III emission.

In order to resolve this dilemma, the *beam-plasma structure* was proposed by Zheleznyakov & Zaitsev (1970a). In this scenario, the electron beam and Langmuir waves travel together, with generation of the waves occurring by the faster moving electrons (at the front of the beam), and absorption of the waves occurring by the slower moving electrons (at the back of the beam). In this case, only a fraction of the total beam energy is lost to radiative processes, and the beam is able to propagate to much larger distances. This has been numerically verified by Takakura & Shibahashi (1976); Mel’Nik et al. (1999) for example.

1.4.2 Wave-Wave Interactions

The production of transverse electromagnetic radio emission (T) from Langmuir wave generation is a non-linear process, which involves the interaction of generated Langmuir waves (L) with either ion-sound waves (S) or counter-streaming Langmuir waves (L') (Melrose, 1980b; McLean & Labrum, 1985). These processes can be described by

$$L + S \rightleftharpoons T, \quad (1.16)$$

$$L \rightleftharpoons S + T, \quad (1.17)$$

$$L + L' \rightleftharpoons T, \quad (1.18)$$

which describe the production of transverse electromagnetic (EM) waves via Langmuir + ion-sound convergence (Eqn. 1.16), Langmuir wave decay into ion-sound waves + EM waves (Eqn. 1.17), and the production of EM waves via Langmuir + (counter-streaming) Langmuir convergence (Eqn. 1.18).

For all of these processes, the energy and momentum is conserved. This requires the fulfilment of the equations

³Sturrock (1964) estimated a few metres for the beam to decelerate to zero.

$$\omega_1 + \omega_2 = \omega_3, \quad (1.19)$$

$$\mathbf{k}_1 + \mathbf{k}_2 = \mathbf{k}_3. \quad (1.20)$$

As the frequency of ion-sound waves is much smaller than the plasma frequency, Equations 1.19 and 1.20 ensure that the generated radio waves will be emitted with characteristic frequencies $\omega_T \sim \omega_{pe}$ (Equations 1.16 & 1.17) or $\omega_T \sim 2\omega_{pe}$ (Equation 1.18), producing fundamental (F) and harmonic (H) emission components.

As the plasma frequency is dependent upon the background plasma density, solar radio emission is a useful diagnostic tool which can be used to estimate the conditions of the outer corona and inner heliosphere, where the low background densities ensure that X-ray and ultraviolet emission is too diffuse to be easily detectable.

1.4.3 Radio Observations

Solar radio emission is traditionally classified according to the observed burst frequency drift rate, df/dt (Wild & McCready, 1950, where f is the burst frequency). The first classifications of radio emission were designated, in order of ascending drift rate, as type-I, type-II, and type-III radio emission, and later Type-IV and Type-V bursts were added to this list. Figure 1.4 (Dulk, 1985) shows a diagram of these radio emission classifications, where the increasing frequency drift rate can be clearly seen via the gradients of the type-I, type-II, and type-III shaded areas.

Type II, III, IV, and V radio bursts are due to the propagation of accelerated electrons (McLean & Labrum, 1985), and the frequency drift rate tells us about the radio production mechanism. Type-II bursts are generated by electrons accelerated in shocks (e.g. at the front of a coronal mass ejection), so the frequency drift rate is directly related to the shock velocity. Type-III bursts are caused by high velocity electron beams accelerated in a Solar Flare, and hence the frequency drift of type-III bursts is extremely rapid compared with the slower moving type-II shocks. Type-V bursts feature smaller frequency drift rates, but are found in association with high

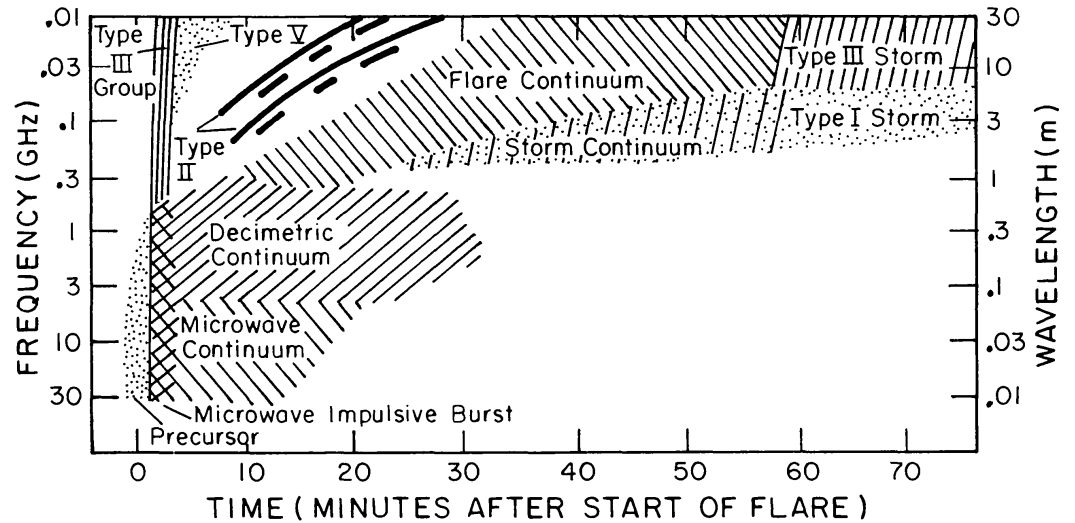


Figure 1.4: Theoretical dynamic spectrum of solar radio burst types that could be produced by solar flares. From [Dulk \(1985\)](#).

frequency type-III bursts (usually following the type-III burst). These are thought to be due to slower moving electron beams. Finally, type-IV bursts are due to emission from trapped electrons, and hence feature little to no frequency drift.

Type-III Characteristics

Type-III bursts typically start between 10-100 MHz ([McLean & Labrum, 1985](#); [Ratcliffe & Kontar, 2014](#)), but have been observed to start at GHz frequencies ([Benz et al., 1983](#)). As the frequency of type-III bursts is inversely proportional to the emission distance from the Sun, the minimum frequency depends upon the maximum distance the flare accelerated electron beam reaches. In several cases, bursts never leave the solar corona, possibly due to the configuration of the magnetic field along which the beam travels. [Reid & Kontar \(2015\)](#) simulated the transport of electrons in a radially expanding magnetic flux tube, and found that the rate of flux tube expansion can greatly affect the distance at which electrons stop generating Langmuir waves, with more rapid flux tube expansion lowering the electron density more rapidly and hence halting the generation of Langmuir waves. However, while most bursts do not exit

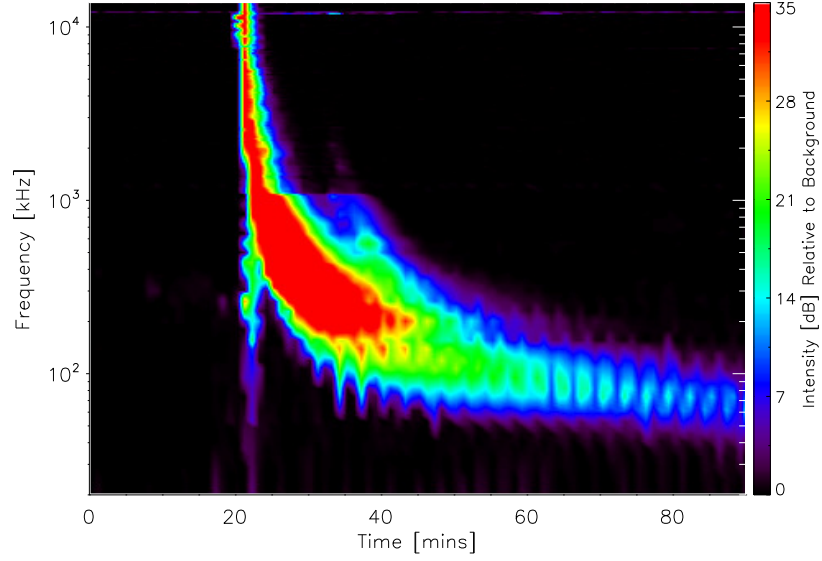


Figure 1.5: Example type-III radio burst, detected with the Wind/ *WAVES* instrument on 2006-01-05. At higher frequencies ($\sim 10^3$ kHz), two bursts can be observed (at ~ 20 mins and ~ 35 mins), while at lower frequencies the bursts merge. The vertical striae seen at low frequencies are likely due to instrumental effects.

the corona, there are multiple examples of bursts which have reached interplanetary space. While there is no hard boundary between the corona and interplanetary space, generally bursts are classified as interplanetary type-IIIs if they are detected below frequencies of around ~ 10 MHz (around $2.6 R_{\odot}$).

The electrons accelerated in a solar flare can reach relativistic or near-relativistic velocities ($\sim 0.05 - 0.6c$ Suzuki & Dulk, 1985; Melnik et al., 2011; Krupar et al., 2015), and hence the frequency drift of type-IIIs is extremely rapid. Alvarez & Haddock (1973) found a frequency drift dependence upon frequency as $df/dt = -0.01f^{1.84}$ via combining observations between 3 MHz – 5 kHz, with results from eight other studies up to 550 MHz. Within a similar frequency range, Melnik et al. (2011) found frequency drift rate relations of $df/dt = -Af + B$ within 10 – 30 MHz, where A was between $0.07 - 0.12 \text{ s}^{-1}$, and B was between $-0.2 - 0.5 \text{ MHz s}^{-1}$.

As mentioned above, type-III bursts can be observed in fundamental/harmonic (F/H) pairs, which are produced near the plasma frequency and double the plasma

frequency, respectively. Varying values for the F/H frequency ratio have been found, such as F:H = 1:1.85 - 1:2.0 (Wild et al., 1954), and 1:1.6 - 1:2 (Stewart, 1974). The deviation from the expected 1:2 ratio is usually attributed to the time delay of the F-component due to its lower group velocity. The F-component of emission is rarely observed above 500 MHz due to strong absorption by the ambient plasma, and hence the H-component often has a higher starting frequency.

Type-III sources tend to grow with decreasing frequency, usually following a $\theta \propto f^{-1}$ relationship (Saint-Hilaire et al., 2013), where θ is the FWHM angular extent of the radio source. Measured θ values have been reported as from 2' at 432 MHz (Saint-Hilaire et al., 2013), down to 50° at 100 kHz (Steinberg et al., 1985). However, the extent upon which scattering and refraction of the radio waves (*propagation effects*) affects the size of the radio source is difficult to discern, as the deconvolution of propagation effects and intrinsic source properties requires extremely high time resolution, high frequency resolution, and high spatial resolution in any instrument.

As type-III bursts are produced near the plasma frequency, the fundamental component should be strongly affected by small variations in the background density of the plasma through which it travels. Early work by Chandrasekhar (1952) on stellar scintillation formed the basis for statistically modelling the passage of radio waves through a turbulent medium. This work was modified for application to the solar corona by Fokker (1965), and has been subsequently used by e.g. Hollweg (1968); Steinberg et al. (1971); Thejappa et al. (2007) to model the propagation of radio waves through the turbulent corona. Arzner & Magun (1999) found that propagation effects can cause a 300 MHz point source to appear with a width of ~ 0.6 -1.7' if viewed at disk centre, and found that the source can appear shifted radially outwards from the true source if viewed closer to the limb. A complication in simulating propagation effects on source images and lightcurves arises from a lack of knowledge of the density profile of the corona, leading to simulations being extremely variable depending upon the background density model and density fluctuation model used. Hence further limits on the density structures within the heliosphere are required to fully understand imaged sources.

Occasionally, type-III bursts can be seen with inverted shapes in dynamic spectra - going from low to high frequencies, or high - low - high frequencies (Labrum & Stewart, 1970). These bursts are called J type and U type bursts, respectively. The common explanation for these bursts is that the beam electrons travel along closed field lines, moving from low to high density regions causing an increase in frequency (Reid & Kontar, 2017). U and J-type bursts are very rare in comparison with “normal” type-III bursts, and they are almost always observed at harmonic frequencies - although the F-component has been observed. A similar feature, where pairs of bursts with opposite frequency drifts appear, can occasionally be observed in type-II bursts, such as recent observations by Carley et al. (2015).

Radio Imaging

While large amounts of information about the radio-producing electron population can be determined simply from the measured dynamic spectrum, the lack of spatial detail complicates analysis featuring co-temporal events. In order to locate the spatial position of the radio emission, and hence differentiate between different simultaneous events, imaging techniques are required. A basic overview of a few different solar radio imagers is included here, with particular focus paid to those which image type-III radio bursts.

Typically, solar radio imagers are formed of large arrays of antennas (interferometric arrays), designed to detect radio emission within a specific frequency range. In their simplest form, an incoming radio signal will be recorded at different times across the array, depending upon the position in the sky of the signal, and the size of the radio source. Hence, by using the signal phase across the array, an image of the radio source can be produced. Large baselines and high time resolution allows for the highest spatial resolution to be achieved, producing high quality images across a range of frequencies.

As mentioned above, while type-III bursts typically start at around 10–100 MHz, they have been observed to begin in the GHz range (Benz et al., 1983, 1992). Several GHz radio imagers have been used throughout the history of radiophysics, allowing for

analysis of the gyro-synchrotron producing electron population within a flare.

Possibly the longest running, high frequency full-Sun imager is the Nobeyama Radioheliograph (NoRH; [Nakajima et al., 1994](#), Figure 1.6), which has produced images of the full disk every day since 1992, allowing for regular images of solar flares at GHz frequencies. As a radioheliograph, NoRH images at two fixed frequencies: 17 and 34 GHz, with spatial and temporal resolutions of $10'' / 0.1$ s (17 GHz) and $5'' / 1$ s (34 GHz), respectively. The lower frequency band is capable of measuring the circular polarisation levels, while the higher level frequency band is capable only of measuring intensity. By imaging at these frequencies, NoRH is able to directly probe the electron population present within a flare, allowing for a spatial and energetic comparison with the escaping (type-III producing) electron population.

More recently, solar observations using the Atacama Large Millimetre Array (ALMA; [Wedemeyer et al., 2016](#); [Shimojo et al., 2017](#), Figure 1.6) have begun. While ALMA is principally an astronomical observatory (not solar specific), adaptations to its filtering have allowed for observations of the Sun between the frequencies of $\sim 90 - 250$ GHz, observing down to the photosphere, where the optical thickness approaches unity. Finally, within the GHz range, the Very Large Array (VLA) has produced solar images of frequencies of 1.5 and 5 GHz, which have been used, for example, to compare the positions of gyro-synchrotron emission with HXR burst locations ([Kundu et al., 1981](#)) or to study the detailed shapes of solar active regions at microwave frequencies ([Alissandrakis et al., 1991](#)).

While GHz radio imagers are used within a flare context to study the (gyro-synchrotron) electron population present within a flare, several lower frequency radio imagers have also been used to track the outwards propagating electron beams. From 1967 to 1984, the Culgoora Radioheliograph (CRH; [Wild, 1967](#)) allowed for unprecedented observations of escaping electron beams at select frequencies. Originally operating at 80 MHz (with a beam-width of $3.8'$), subsequent 42.25 MHz ([Sheridan et al., 1973](#), beam-width $7.5'$), 160 MHz (beam-width $1.9'$), and 327.4 MHz (beam-width $0.93'$ [Sheridan et al., 1983](#)) channels were added, allowing for the tracking of electrons through the solar corona and the study of the solar brightness temperature

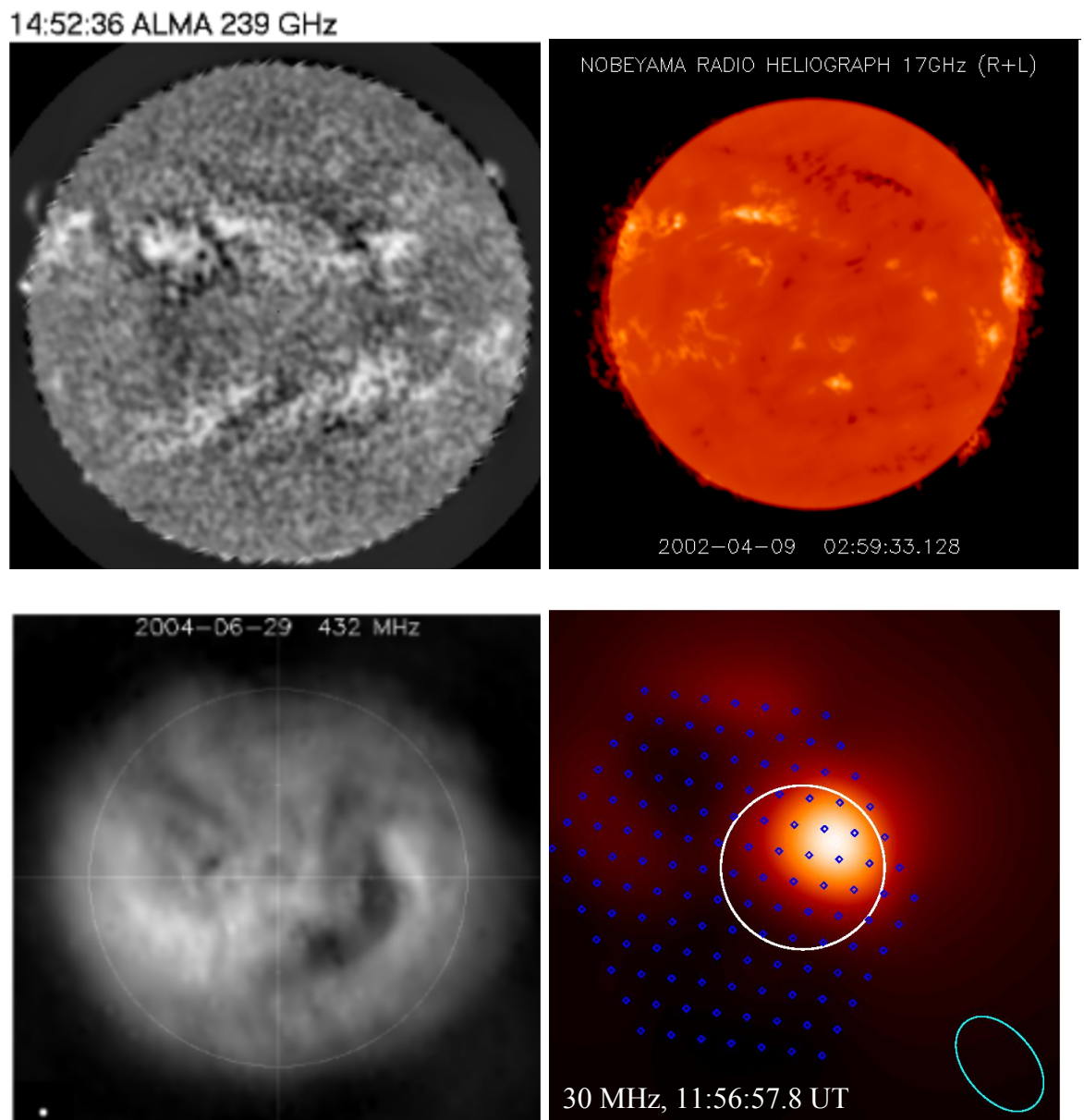


Figure 1.6: Full-Sun radio images at different frequencies, showing: (**top left**) ALMA (239 GHz; [Alissandrakis et al., 2017](#)); (**top right**) Nobeyama Radioheliograph (17 GHz; from the NoRH website); (**bottom left**) Nançay Radioheliograph (432 MHz; [Mercier & Chambe, 2012](#)); (**bottom right**) LOFAR (30 MHz; N. Sharykin, personal communication). The white point and blue oval in NRH and LOFAR images show beam size, and the blue diamonds in the LOFAR image show beam locations.

out to a height of $\sim 1R_{\odot}$ from the solar surface. Most of the findings from CRH's 17 year run are summarised by [McLean & Labrum \(1985\)](#).

Within a similar frequency range (150-450 MHz), the Nançay Radioheliograph (NRH; [Kerdraon & Delouis, 1997](#), Figure 1.6) has produced regular full-Sun images between $1.25' - 5.5'$ resolution (at 164 MHz and 432 MHz respectively). Statistical studies of type-III bursts using NRH have been performed, for example finding strong and weak correlations between radio flux and solar cycle, and source size and solar cycle respectively ([Saint-Hilaire et al., 2013](#)), and challenging the assumption that every type-III radio burst features a HXR counterpart ([Reid & Vilmer, 2017](#)).

While radioheliographs such as CRH and NRH allow for excellent imaging at single frequencies, limitations of single frequency imaging mean that another instrument is required to measure the dynamic spectrum, allowing for proper comparisons. The LOw Frequency ARray (LOFAR; [van Haarlem et al., 2013](#), Figure 1.6) operates within a frequency range of $\sim 30-90$ MHz, allowing for imaging of the type-III radio burst far out into the solar atmosphere. By using a tied-array imaging technique with high spatial, temporal, and frequency resolution, the passage of multiple type-III bursts was tracked by [Morosan et al. \(2014\)](#), revealing non-radial motion of the radio source. Imaging of type-III U and J bursts has allowed for a limiting of the accelerated beam and background plasma parameters which cause the bursts ([Reid & Kontar, 2017](#)), while a comparison type-III source positional and size variations with dynamic spectral properties has allowed for a deconvolution of radio source properties from radiowave propagation effects ([Kontar et al., 2017](#)); allowing for limits on the coronal density turbulence to be placed.

At lower frequencies (≤ 10 MHz), Earth's atmosphere prevents incoming radiation from reaching ground based detectors, and hence, spaceborne instruments are required to study the lowest frequency radio bursts. A consequence of this is the lack of imaging at frequencies lower than ~ 15 MHz, leading to difficulties in properly tracking the flare electron population out into the heliosphere. However, alternative methods can be used to overcome this, and locate the emission position of bursts, such as triangulation (e.g. [Fainberg et al., 1972](#); [Reiner et al., 1998](#); [Krupar et al., 2014](#)) or multilateration (e.g.

[Weber et al., 1977](#)) via multi-spacecraft observations.

1.5 The Interplanetary Medium

The atmosphere outside of the Sun is known as the Interplanetary Medium, and features both large and small scale gradients in density and magnetic field strength as the solar wind streams away from the Sun.

1.5.1 Magnetic Field

As the solar wind moves away from the solar surface into interplanetary space, the solar magnetic field is dragged out with the particles, forming an Archimedean spiral due to the Sun's rotation. As mentioned previously, this magnetic field structure is called the Parker Spiral (PS), after it was first proposed by [Parker \(1958\)](#). Charged particles subsequently released during solar flares will escape into this field structure and be guided along the magnetic field.

The typical quoted length of a PS field line at Earth (radial distance 1 AU) is 1.2 AU, as predicted by the simple PS model. However, while the large scale open magnetic field is well described by a simple PS, close to the corona smaller scale closed magnetic structures can be seen in the form of loops, streamers, and prominences. These are highlighted by the ambient plasma, which remains trapped within the structures, emitting in EUV wavelengths. The typical magnetic field strength within a sunspot is around 1000 G, while within a coronal loop this decreases to between 1-10 G ([Aschwanden, 2005](#)). By using multiple methods to measure the magnetic field strength within the corona, [Dulk & McLean \(1978\)](#) derived the empirical relationship $B(r) = 0.5(r/R_{\odot} - 1)^{-1.5}$ G, where $B(r)$ is the coronal magnetic field strength, and r is the radial distance from the photosphere. The magnetic field strength continues to decrease along open field structures, resulting roughly in a $B \propto r^{-2}$ relation far away from the Sun. At Earth, the measured magnetic field is around $10\text{-}30 \times 10^{-5}$ G.

The interplanetary magnetic field is a turbulent medium, with regions of high and

low magnetic field randomly placed along the length of a PS. Typically, the magnetic field fluctuations are thought of as parallel (to the magnetic field) fluctuations and perpendicular (to the field) fluctuations - called *slab* and *2D* fluctuations respectively. Measurements of magnetic field fluctuations show a roughly powerlaw shape within an inertial range, with powerlaw index values measured at ~ -1.66 (Podesta et al., 2007), close to the Kolmogorov spectral index of $-5/3$. At smaller wavelengths, the spectrum becomes steeper, dropping to a powerlaw with spectral index roughly -2.33 (Bruno & Telloni, 2015). This continues until around the proton gyroradius scale, where the spectrum becomes steeper again.

Studies of the slab-to-2D turbulence ratio in solar wind by Dasso et al. (2005) revealed that generally fast solar wind features slab magnetic fluctuations, while slow solar wind features 2D fluctuations. Similarly, studies of magnetic turbulence as a function of distance (using Helios 1 and 2; Ruiz et al., 2011) show a general shift from quasi-parallel to quasi-perpendicular fluctuations with increasing heliocentric distances. As such, when modelling purely 1D turbulence along the field line, it is reasonable to assume that the fluctuation amplitude will decrease with distance.

1.5.2 Electron Density

As the solar magnetic field decreases, so too does the background plasma density. A simple model of heliospheric density was derived by Parker (1958), who assumed an isothermal steady flow of plasma from the high temperature corona outwards into interplanetary space. Although this model misses many finer features of the solar wind (due to its simple assumptions), one prediction of the model was an increase of solar wind speed with distance, which was been observationally confirmed at 1 AU (Hewish & Wyndham, 1963, for example).

Empirical density models have been derived by Newkirk (1961); Saito et al. (1977), for example, who used the van de Hulst (1950) method of inverting polarised brightness (pB) images of the solar corona to obtain the background electron density as a function of radius. More recently Leblanc et al. (1998) derived a model of electron density based

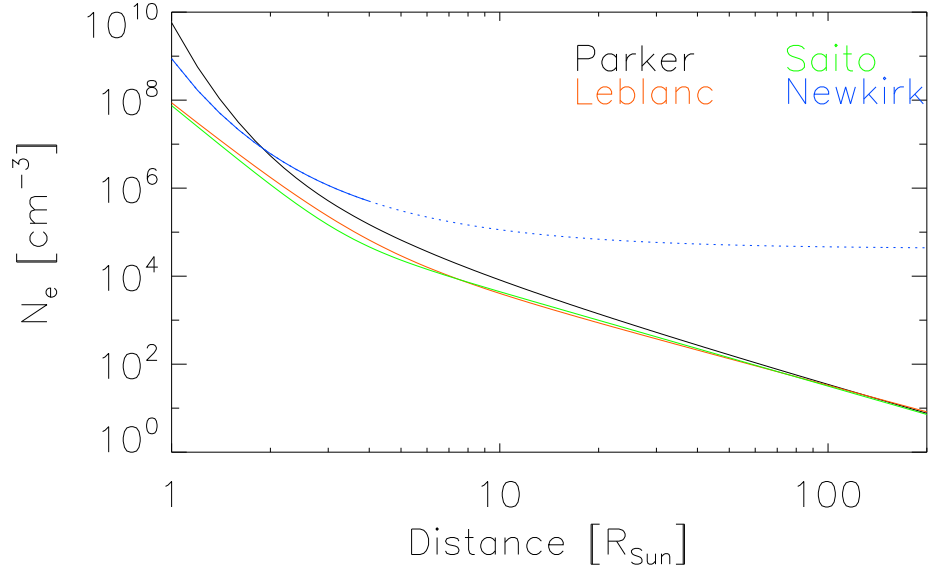


Figure 1.7: Comparison of four popular electron density models from the photosphere out to near Earth. The Newkirk model is a coronal model, and hence is only taken out to $4 R_{\odot}$.

upon type-III radio observations. These four models are described by the equations,

$$n_{e,Parker}(r) = \frac{\alpha}{r^2 v(r)} \quad [\text{cm}^{-3}], \quad (1.21)$$

$$n_{e,Newkirk}(r) = N \times 4.2 \times 10^4 \times 10^{4.32/r} \quad [\text{cm}^{-3}], \quad (1.22)$$

$$n_{e,Saito}(r) = \frac{1.36 \times 10^6}{r^{2.14}} + \frac{1.86 \times 10^8}{r^{6.13}} \quad [\text{cm}^{-3}], \quad (1.23)$$

$$n_{e,Leblanc}(r) = \frac{3.3 \times 10^5}{r^2} + \frac{4.1 \times 10^6}{r^4} + \frac{8 \times 10^7}{r^6} \quad [\text{cm}^{-3}], \quad (1.24)$$

where α is a normalising constant, r is the radial distance from the Sun (in R_{\odot}), $v(r)$ is the velocity profile of the solar wind, and N is the density folding factor accounting for higher ($N > 1$) or lower ($N < 1$) density regions of the corona. A comparison of these four models is given in Figure 1.7, showing a large disparity in both theoretical and measured coronal densities, but general agreement farther out from the Sun.

In addition to the background density profile, there are several high and low density regions surrounding the corona, such as coronal holes (low density) and coronal

streamers (high density). By measuring the ratio of Si VIII and S X intensities, [Dosc hek et al. \(1997\)](#) estimated the line-of-sight integrated densities within a coronal hole at a factor of $\sim 1/2$ lower than normal quiet Sun levels between 1-1.3 R_{\odot} . Similarly, measurements of the Si IX 342/250 Å ratio by [Fludra et al. \(1999\)](#) showed polar coronal hole densities to be $\sim 2/5$ lower than quiet Sun densities between the ranges of 1-1.1 R_{\odot} . In contrast, coronal streamers often feature much higher densities than the background. [Koutchmy & Livshits \(1992\)](#) record streamer densities of $\sim 5 - 10\times$ larger than measured equatorial density, while observations by [Saito & Owaki \(1967\)](#) show enhanced densities of around an order of magnitude compared to [Newkirk \(1961\)](#) model densities.

At smaller scales, the interplanetary medium features a spectrum of density fluctuations. At 1 AU, direct measurements of the mean fluctuation level via scintillation techniques by [Celnikier et al. \(1983\)](#) have shown an amplitude of $\delta n_e/n_e \sim 10\%$. By comparing the broadening of radio sources as they passed through the region of 10-100 R_{\odot} with simulations, [Hollweg & Harrington \(1968\)](#) determined density fluctuation amplitudes of around $\delta n_e/n_e \sim 7\%$, although an assumption of constant fluctuation amplitude within this range was taken.

Observations of a change in flux and size of the Crab Nebula as it passes close to the Sun have been used by [Sasikumar Raja et al. \(2016\)](#) to measure density fluctuation levels closer to the Sun, revealing density fluctuations of amplitudes $\delta n_e/n_e \sim 0.1 - 5\%$ between 10-50 R_{\odot} , with a general increase in fluctuation level with radial distance. Similarly, simulations of electron beam transport and Langmuir wave generation by [Reid & Kontar \(2010, 2013\)](#) have suggested that the fluctuation amplitude should increase with heliocentric distance. Typically, the spectrum of fluctuations follows a Kolmogorov spectrum, with a minimum scale length around the proton inertial scale $l_i = 228/\sqrt{n[\text{cm}^{-3}]}$ km ([Sasikumar Raja et al., 2016](#)). In this thesis, density fluctuations of amplitudes $\delta n_e/n_e \in [0, 10]\%$ down to scale lengths of $l_i = 1$ km are considered.

1.6 Particle and Wave Transport in the Heliosphere

As much of the work presented within this thesis deals with the modelling of solar flare radiation transport from the flare site to Earth, a brief overview of the propagation mathematics is given here.

1.6.1 Particle Propagation Through a Magnetic Field

If the number density of charged particles emitted from the solar atmosphere into the heliosphere is low enough, then their path of motion will be strongly determined by the solar magnetic field (Jokipii, 1966). Under the assumption that the background electric field is low enough to be negligible for particle transport, a particle's motion is defined by the Lorentz equation

$$\mathbf{F} = q\mathbf{v} \times (\mathbf{B}_0 + \delta\mathbf{B}), \quad (1.25)$$

where q , \mathbf{v} are the particle's charge and velocity vector, and $\mathbf{B}_0 + \delta\mathbf{B} = \mathbf{B}$ is the quasi-linear theory (QLT) approximation, describing a magnetic field comprised of mean (\mathbf{B}_0) and fluctuating ($\delta\mathbf{B}$) components.

Particle motion can be defined by the particle's motion along ($v_{\parallel} = v\mu$) and perpendicular ($v_{\perp} = v\sqrt{1 - \mu^2}$) to the field, giving rise to the pitch-angle cosine, μ . If the guiding magnetic field features small-scale fluctuations, then a particle distribution travelling along the field will be scattered by these fluctuations.

Mathematically, this diffusion is described by the pitch-angle diffusion coefficient (e.g. Agueda et al., 2008; Dröge et al., 2014), given by

$$D_{\mu\mu} = \int_0^{\infty} \langle \dot{\mu}(t)\dot{\mu}(0) \rangle dt, \quad (1.26)$$

where $\dot{\mu}$ is the time-derivative of a particle's pitch angle. This is obtained from Equation (1.25) as (e.g. Qin & Shalchi, 2009)

$$\dot{\mu} = \Omega_{ce} \sqrt{1 - \mu^2} \left(\frac{\delta B_x(z)}{B_0} - \frac{\delta B_y(z)}{B_0} \right), \quad (1.27)$$

where $\Omega_{ce} = eB_0/m_e c$ is the electron gyrofrequency. In this example, the electron gyrophase is ignored due to the assumption that the particle's guiding centre remains constant. Substituting Equation (1.27) into Equation (1.26) gives the pitch-angle diffusion coefficient as

$$D_{\mu\mu} = \int_0^\infty \langle \dot{\mu}(t)\dot{\mu}(0) \rangle dt = \int_0^\infty \langle \delta B(t)\delta B(0) \rangle \frac{\Omega_{ce}^2(1-\mu^2)}{B_0^2} dt. \quad (1.28)$$

Finally, the magnetic fluctuations are assumed to form a symmetric turbulence spectrum in wavenumber space, $\langle \delta B \delta B^* \rangle = \dot{W}(k_\parallel)$ which, when inserted into Equation (1.28), gives diffusion coefficient for an arbitrary turbulence spectrum as (Kontar et al., 2014),

$$D_{\mu\mu} = \frac{\pi(1-\mu^2)}{2|\mu|v} \Omega_{ce}^2 \left. \frac{W(k_\parallel)}{B_0^2} \right|_{k_\parallel = \Omega_{ce}/v|\mu|}. \quad (1.29)$$

In this case, only particles which are resonant with fluctuations will scatter, limiting the relevant spatial wavenumber range to $k_\parallel = \Omega_{ce}/v|\mu|$. Using this description, the average distance travelled by a particle between interactions can be calculated. This is given by the mean-free path λ_\parallel , defined as (Schlickeiser, 1989)

$$\lambda_\parallel = \frac{3v}{8} \int_{-1}^1 \frac{(1-\mu^2)^2}{D_{\mu\mu}} d\mu. \quad (1.30)$$

1.6.2 Wave Propagation Through a Plasma

In order to model the propagation of electromagnetic waves through the heliosphere, the wave dispersion relation must be known, and the following demonstrates its derivation. In their differential forms, Maxwell's equations relate a wave's electric and magnetic fields, and are given by (Griffiths, 1962)

$$\nabla \cdot \mathbf{D} = 4\pi\rho_f, \quad (1.31)$$

$$\nabla \cdot \mathbf{B} = 0, \quad (1.32)$$

$$\nabla \times \mathbf{E} = -\frac{1}{c} \frac{\partial \mathbf{B}}{\partial t}, \quad (1.33)$$

$$\nabla \times \mathbf{H} = \frac{1}{c} \left(\frac{\partial \mathbf{D}}{\partial t} + 4\pi\mathbf{J} \right), \quad (1.34)$$

where \mathbf{E} , \mathbf{B}) are the electric and magnetic field components in a vacuum, \mathbf{D} , \mathbf{H} are the respective field components in an electromagnetic medium, ρ_f is the background charge, \mathbf{J} is the current, and c is the wave speed. Here, $\mathbf{D} = \epsilon\mathbf{E} = (1 + 4\pi\chi)\mathbf{E}$ and $\mathbf{B} = \mu_f\mathbf{H}$, where ϵ , χ , & μ_f are the electric permittivity, electric susceptibility, and magnetic permeability.

When travelling through a vacuum, $\epsilon = \mu_f = 1$, and $\mathbf{J} = \rho_f = 0$. However, the heliospheric background is not a perfect vacuum; it features small magnetic and electric fields. If we assume that the magnetic field far from the surface of the Sun is small enough to become negligible to wave propagation (hence $\mu_f = 1$), the background charge is small, and that there are no currents present, then Maxwell's equations become

$$\nabla \cdot \mathbf{D} = 0, \quad (1.35)$$

$$\nabla \cdot \mathbf{B} = 0, \quad (1.36)$$

$$\nabla \times \mathbf{E} = -\frac{1}{c} \frac{\partial \mathbf{B}}{\partial t}, \quad (1.37)$$

$$\nabla \times \mathbf{B} = \frac{1}{c} \frac{\partial \mathbf{D}}{\partial t}. \quad (1.38)$$

By taking the curl of Equation (1.33), the electric field wave equation can be derived:

$$\nabla^2 \mathbf{E} - \frac{\epsilon}{c^2} \frac{\partial^2 \mathbf{E}}{\partial t^2} = 0, \quad (1.39)$$

and using the plane wave assumption ($\mathbf{E} = \mathbf{E}_0 \exp[i(\mathbf{k} \cdot \mathbf{r} - \omega t)]$), a relationship

between wave frequency (ω) and wavenumber (k) is found. However, in order to solve this, the form of the electric permittivity must be known.

Within an electric field, electrons travel as $\mathbf{r} = -e\mathbf{E}/(m_e\omega^2)$, where e , m_e , & ω are electron charge, mass, and angular gyration frequency. If the plasma is assumed to be uniform, then the electric susceptibility is given by $\chi = -n_e e^2/m_e\omega^2$, where n_e is the background electron number density. Given this, the electric permittivity is found as

$$\epsilon = 1 - \frac{4\pi n_e e^2}{m_e\omega^2} = 1 - \left(\frac{\omega_{pe}}{\omega}\right)^2. \quad (1.40)$$

Substituting this into Maxwell's equations and using the plane wave assumption, the dispersion relation for electromagnetic waves travelling in an unmagnetised plasma can be derived as

$$\omega^2 = \omega_{pe}^2 + c^2 k^2. \quad (1.41)$$

Finally, the refractive index (ρ) of waves travelling through an unmagnetised plasma can be determined from the electric permittivity and magnetic permeability, and is given as

$$\rho = \sqrt{\epsilon\mu_f} = \sqrt{1 - \omega_{pe}^2/\omega^2}. \quad (1.42)$$

1.6.3 Ray Tracing

While many methods for modelling electromagnetic wave transport through a plasmas exist, one of the simplest and oldest is the method of *ray tracing* (Budden, 1988). In this scheme, each wave is assumed to have a locally uniform wavefront, and its passage can be described by a ray pointed normal to the wavefront (Figure 1.8).

When travelling through a stratified medium, a ray's path will be altered, resulting in the ray following a curved path towards regions of lower density. This can be described by assessing the transit time of an individual ray

$$t_p = \int \frac{ds}{v_p}, \quad (1.43)$$

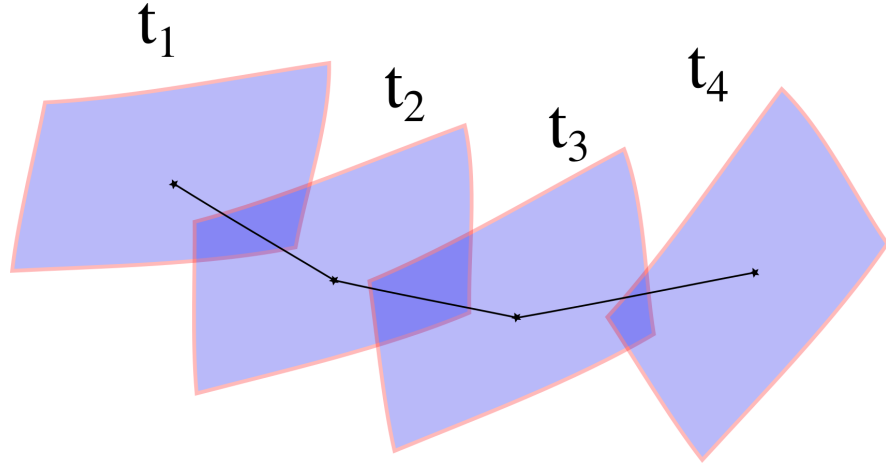


Figure 1.8: Ray tracing basic method. The blue wavefront moves forward in time (t_1 , t_2 , etc), and its path can be described simply by a ray placed on the wavefront, which moves forward along the same path. By adding multiple rays, the entire wavefront can be approximated.

where $v_p = c/\rho(r(s))$ is the phase velocity of the ray, and ds is the infinitesimal path length of the ray. The principle of least action states that the ray will travel along the path that produces the least work; that is, if the path is varied from $\mathbf{r}(s)$ to $\mathbf{r}(s) + \delta\mathbf{r}(s)$, then the ray will follow the path which produces a minimal time increase δt_p . This time variation is described by

$$\delta t_p = \frac{1}{c} \int \delta\rho ds + \rho \delta ds, \quad (1.44)$$

where $\delta\rho = \nabla\rho \cdot \delta\mathbf{r}$, and $\delta ds = ds(d\mathbf{r}/ds \cdot d\delta\mathbf{r}/ds)$. Rearranging Equation (1.44) and taking $\delta t_p = 0$, gives

$$\frac{1}{c} \int \left(\nabla\rho - \frac{d}{ds} \left[\rho \frac{d\mathbf{r}}{ds} \right] \right) \delta\mathbf{r} ds = 0, \quad (1.45)$$

which, assuming that the variation in path $\delta\mathbf{r}$ is non-zero, requires that

$$\frac{d}{ds} \left[\rho \frac{d\mathbf{r}}{ds} \right] = \nabla\rho. \quad (1.46)$$

With this description, the passage of an electromagnetic wave through an increasingly sparse medium can be approximated. This method has been used by Chan-

drasekhar (1952); Fokker (1965); Hollweg (1968), for example, to model ray propagation through a fluctuating plasma.

As before, a QLT approximation can be made to model mean and fluctuating density components. In this method, the background electron density is given as $n_e = n_0 + \delta n_e$, and the refractive index is given by $\rho = \rho_0 + \delta\rho$. Using this form, the fluctuating component of refractive index can be found from Equation (1.42) as

$$\delta\rho = -\frac{1}{2\rho} \left(\frac{f_{pe}}{f} \right)^2 \frac{\delta n_e}{n_0}. \quad (1.47)$$

Each fluctuation in density/refractive index will produce a small variation in ray direction, represented here through the ray direction cosine T . The variance in direction cosine is given by Steinberg et al. (1971) as $\langle \delta T^2 \rangle = 2\sqrt{\pi} \int \frac{\langle \delta \rho^2 \rangle}{\rho^2 h} ds$, where h is the fluctuation scale length. Using Equation (1.47), and approximating the integral as a sum over small step length Δs , the direction variance is given as (Steinberg et al., 1971)

$$\langle \delta T^2 \rangle \approx \frac{\sqrt{\pi}}{2} \left(\frac{f_{pe}}{\rho f} \right)^4 \left(\frac{\delta n_e}{n_0} \right)^2 \frac{\Delta s}{h}. \quad (1.48)$$

Various alterations to this form of scattering have been produced (e.g. Arzner & Magun, 1999; Thejappa et al., 2007), but the general form remains the same. This method gives an extremely simple yet powerful method to trace the path of electromagnetic radiation through arbitrary unmagnetised plasmas, allowing for easy modelling of low-frequency radiation from a solar flare to Earth. This treatment is similar to both stochastic particle transport models (e.g. MacKinnon & Craig, 1991; Agueda et al., 2008; Laitinen et al., 2016) and HXR transport models (e.g. Kontar & Jeffrey, 2010; Jeffrey & Kontar, 2011), which have successfully been used to study the effects of scattering on observed spectra and images.

1.7 Instrument Overview

Observations using the Wind/*3 Dimensional Particle Telescope* (Wind/*3DP*; [Lin et al., 1995](#)), Wind/*WAVES* instrument ([Bougeret et al., 1995](#)), STEREO/*WAVES* instruments ([Bougeret et al., 2008](#)), and Reuven Ramety High Energy Solar Spectroscopic Imager (RHESSI; [Lin et al., 2002](#)) are presented within this thesis. Observations using Wind/*3DP*, Wind/*WAVES*, and RHESSI form the basis for Chapter 2, while the Wind/*WAVES* and STEREO/*WAVES* instruments form the observational basis for Chapter 5. All instruments are spaceborn, and all data was analysed in the Solar SoftWare (SSW) package in the Interactive Data Language (IDL), except for STEREO/*WAVES* data, which was analysed using the TMLib package in IDL.

Spacecraft/ Instrument	Species	Energy/ Frequency Range
Wind/ 3DP (SST Foil)	Electrons	25 - 400 keV
Wind/ WAVES (RAD1+RAD2)	Radio Waves	20 kHz – 13.825 MHz
STEREO/ WAVES (HFR1+HFR2)	Radio Waves	125 kHz – 16.075 MHz
RHESSI	X-rays & γ -rays	3 keV – 20 MeV

Table 1.1: Table listing instruments used within this thesis, showing particle species and energy/ frequency range covered.

1.7.1 Wind

Launched on the 1st of November 1994, the Wind spacecraft is a spin-stabilised satellite which, since 2004, has stayed at Lagrange point 1 (L1) between Earth and the Sun, in order to measure the properties of the Solar Wind before it interacts with Earth's magnetosphere and atmosphere.

3DP

The 3 Dimensional Particle Solid State Telescope (Lin et al., 1995) aboard the Wind spacecraft consists of three pairs of double-ended silicon semi-conductor detectors, measuring > 20 keV electrons and protons. A thin lexan foil covers one end of each telescope, which stops the entry of protons up to ~ 400 keV from penetrating the detector behind, while leaving the electron energy spectrum unchanged. The foil also has 150 nm of Aluminium evaporated onto each side to prohibit sunlight from contaminating the detectors.

Each end of a telescope has a $36^\circ \times 20^\circ$ FWHM field of view, giving a combined view of $180^\circ \times 20^\circ$. During one full rotation, a full 4π steradian view is achieved, and hence the directional data from 48 sectors is used to calculate the pitch angle distribution of observed electrons. To correct for bad bins and low countrate, the 48 sectorised directional intensities are recombined into 8 pitch angle (θ) bins of width 22.5° , allowing analysis of anti-sunward (0°) and sunward travelling electrons (180°). This is achieved by taking the scalar product of the magnetic field vector measured by the spacecraft (\mathbf{B}) and the sector unit normal vector (\hat{s}), giving $\theta = \arccos(-\mathbf{B} \cdot \hat{s})$ (Lin et al., 1995).

The data used is minute-averaged, and covers an energy range of 25 – 400 keV in 6 energy channels, with energy bin widths of $\sim \Delta E/E = 30\%$.

WAVES

The *WAVES* instrument aboard the Wind spacecraft is composed of three orthogonal electric field dipole antennas, one directed along the spacecraft spin axis (called E_z), and two directed in the spin plane (E_x and E_y). The two receiver bands used are Radio Receiver Bands 1 and 2 (*RAD1* and *RAD2*). *RAD1* scans a frequency range of 20 kHz – 1.04 MHz with a resolution of 3 kHz, and *RAD2* scans a range of 1.075 MHz – 13.825 MHz with a resolution of 20 kHz (Bougeret et al., 1995). All data used from the Wind/*WAVES* instrument is minute-averaged.

1.7.2 STEREO

Launched on the 26th of October 2006, the STEREO spacecraft are two identical solar observers, orbiting the Sun. The two spacecraft were launched with different orbital radii to Earth; one with a slightly smaller orbital radius than Earth and one with a slightly larger orbital radius than Earth. This leads to one spacecraft trailing Earth's orbit (STEREO Behind; STEREO-B), and one preceding Earth's orbit (STEREO Ahead; STEREO-A). The angular separation of the two spacecraft increases at around 43.6° per year, and on the 6th of February 2011, the spacecraft were 180° separated, allowing a complete view of the surface of the Sun.

Although similar to the WIND/ *WAVES* instrument in many ways, the STEREO/ *WAVES* instrument features some key differences. Unlike Wind, the STEREO spacecraft are 3-axis stabilised, keeping one side facing the Sun at all times. The three antennae are deployed facing away from the Sun to remove them from the fields of view of solar imagers aboard the spacecraft.

The two receiver bands used in this thesis are the High Frequency Receivers (*HFR1* and *HFR2*), which scan a combined frequency range of 125 kHz – 16.025 MHz. The data used in this work had a time resolution of 38.05s, and a frequency resolution of 50 kHz (Bougeret et al., 2008).

1.7.3 RHESSI

RHESSI (Lin et al., 2002) is a NASA Small Explorer mission, launched on the 5th of February 2002, designed to take spectra and high resolution images from soft X-rays (SXR; 3 keV) up to γ -rays (17 MeV) with good energy resolution. The spacecraft is in orbit around Earth at an altitude of ~ 600 km. The telescope consists of nine cooled segmented germanium detectors, capable of taking spectra with an energy resolution of < 1 keV at 3 keV, increasing to 5 keV at 5 MeV. As an incident photon hits the detector, a small current is produced and a count is measured. By relating the count spectrum to the background spectrum and spectral response matrix, the incident photon spectrum can be reconstructed.

Each detector is split into two components; front, a thin segment which can detect X-rays up to an energy of 250 keV, and rear, a thicker segment which detects the remaining photons up to 20 MeV. To account for extremely high photon flux in strong events, two aluminium disk attenuators can be placed in front of the detectors to absorb the lowest energy photons, leaving the high energy end of the spectrum unchanged. This gives RHESSI an extremely large dynamic range (seven orders of magnitude in intensity and four orders of magnitude in photon energy), allowing SXR observations from microflares up to X-class flares. There are three attenuator states available: A0, A1, and A3, corresponding to no attenuator, thin attenuators only, and thick and thin attenuators.

RHESSI is also capable of high resolution imaging, due to a rotating modulation collimator (RMC) placed in-front of the detectors. The RMC is made of a pair of widely separated grids, made of opaque slats separated by transparent slits. The slits on each grid are parallel to each other, leading to the transmission of an X-ray through the grid pair being dependent upon the photon's incident angle. RHESSI rotates once on its axis every four seconds, giving a modulation pattern in intensity dependent upon both the photon source size and position on the Sun. Via Fourier transformation of the modulation pattern, the X-ray image for a given energy range can be reconstructed (Lin et al., 2002).

RHESSI Data Analysis

One of the advantages of RHESSI is the large number of different data analysis methods. As RHESSI records counts, the data can be re-binned to any desirable form (down to the temporal, spatial, and energetic resolution of the detectors). The photon spectrum can be obtained from observations in the HESSI package in SSW, and can be analysed in the Object Spectral Executive (OSPEX; Schwartz et al., 2002). As mentioned above, the count spectrum (**C**) is related to the incident photon spectrum (**I**) via the background spectrum (**B**) and the spectral response matrix (**SRM**):

$$\mathbf{C} = \mathbf{B} + \mathbf{SRM} \mathbf{I}. \quad (1.49)$$

In every event in this thesis, the background is taken as the pre-flare quiet time, and this is simply subtracted from the count rate before passing the spectrum through OSPEX.

The **SRM** is a combination of many instrumental effects, including: absorption of photons into the thermal blankets, detector coolant windows, or grid-pair; Compton scattering into/out of the detectors; Compton scattering off Earth's atmosphere; noise from the electronics; detector degradation from radiation damage; and the low energy cutoff due to the electronics. These effects can change both the intensity of the measured counts, and the apparent energy of the count (Smith et al., 2002). When fitting the photon spectrum with various emission models, the model is multiplied by the **SRM** before comparison with the observed spectrum. Any free parameters are varied until the goodness-of-fit parameter is minimised, ensuring the best fit is produced.

In this thesis, four fit functions are used to reconstruct the electron spectrum from the observed X-ray spectrum:

- *vth* – Optically thin thermal bremsstrahlung is fit from a single temperature distribution (Equation 1.9). Two free fit parameters were used: temperature (kT [keV]), and emission measure (EM [cm^{-3}]). One fixed fit parameter was used: the relative abundance of iron, nickel, calcium, sulphur, and silicon compared to the abundances found in the Chianti database (e.g. Del Zanna et al., 2015), which was set as 1.
- *thick2* – A thick-target photon source is fit from an isotropic electron distribution (Equations 1.11 & 1.12). Five free fit parameters were used: normalisation flux ($\langle nVF_0 \rangle [10^{34} \text{ electrons cm}^{-2} \text{ s}^{-1}]$), power-law index below the break energy (δ_1), break energy (E_b [keV]), power-law index above the break energy (δ_2), and low-energy cutoff (E_c [keV]). One fixed fit parameter was used: the high energy cutoff (E_h [keV]), which was fixed at 32 MeV.

-
- *thin2* – A thin-target photon source is fit from an isotropic electron distribution (Equations 1.11 & 1.13). The same six fit parameters are used as in the thick-target fit, keeping E_h fixed at the same value.
 - *albedo* – Compton backscattering of X-rays can produce a characteristic bump in the photon spectrum at around 30 keV (Kontar et al., 2006). The albedo pseudo-function corrects for this bump, and here features no free parameters. The only parameter used is the anisotropy measure (ratio of upwards to downwards travelling photons), which is fixed at 1 (isotropic).

Chapter 2

Pitch Angle Scattering of Flare Electrons in the Inner Heliosphere

This work can be found in Alcock, Kontar, & Agueda (submitted to the Journal of Geophysical Research: Space Physics).

2.1 Background

In the simplest model of electron release from a flare acceleration site, particles are released simultaneously into open and closed magnetic field structures, where the escaping (open field) high energy (> 40 keV) particles travel nearly scatter-free to 1 AU. This hypothesis arises from the symmetry of simple magnetic reconnection models, which allow both upwards and downwards motion of accelerated electron beams tied to the magnetic field via the relaxation of the magnetic field in both directions. Under this assumption, the timing and spectral shape of a population of electrons detected in-situ (e.g. by the Wind/*3DP* detector; §1.7.1) should exactly match the inferred solar electron population determined through hard X-ray (HXR) observations (Lin, 1974, 1985; Daibog et al., 1981; Krucker et al., 2007; James et al., 2017). When an energetic electron population is detected near Earth, velocity dispersion analysis was traditionally used to find the release time of the electrons at the Sun, assuming scatter-free

transport (Krucker et al., 1999; Claßen et al., 2003, for example).

However, over the past ~ 15 years, significant findings have challenged this scatter-free paradigm. Several observations of delayed high energy electron arrival at Earth with respect to electromagnetic emission were made (e.g. Krucker et al., 1999; Haggerty & Roelof, 2002). Analysis of these events found a median delay of ~ 10 -15 minutes with respect to the injection time inferred from electromagnetic emission. Secondly, the peak-flux spectrum of near-Earth electrons has been found to be harder than the inferred solar electron spectrum (Krucker et al., 2007, 2009; James et al., 2017), implying that either the detected electron population is not from the HXR producing population, or that some process is altering the electron spectrum during transport.

Multiple theories explaining the late arrival of electrons at 1 AU have been proposed: i) large-scale wandering of the flux tube along which the electron population travels could cause apparent delays of the population at 1 AU (Ragot, 2006); ii) delayed acceleration of the detected high energy electrons could occur in a different position to the acceleration site of the type-III producing electrons (e.g. by a coronal shock above the flare site vs the flare site itself) (Krucker et al., 1999; Haggerty & Roelof, 2002; Klassen et al., 2002); iii) Cane (2003) suggested that the high energy population is delayed through some interaction experienced during transport to 1 AU.

While these explanations have been used to account for the delaying of high energy electrons, the conclusions of early work was based upon radio observations alone, and HXR observations were not accounted for. However, in many delayed events, high energy (> 25 keV) HXR emission is observed concurrent with the type-III burst start, implying simultaneous high and low energy electron injection at the flare site. HXR observations were analysed in Krucker et al. (2007); James et al. (2017), however numerical simulations of electron transport are required to test whether the HXR producing electrons and in-situ detected electrons originate from the same population.

While it is reasonable to assume that the background solar wind is too diffuse to allow for strong collisional scattering of the solar flare electrons, and the > 40 keV electron beam is too diffuse to generate Langmuir waves, further wave-particle interactions could serve to scatter the electron population significantly, affecting both

the arrival time and peak-flux spectrum of the electron population.

As an electron population travels along a magnetic field, micro-scale fluctuations can vary the electron's velocity along the field; diffusing the population over multiple interactions. Provided that $|v|$ does not vary over one scattering, this repeated process is called *pitch-angle scattering*, and has been used to explain the apparent delay of electrons at 1 AU. Using a whistler-wave spectrum to model scattering of electrons, [Vocks & Mann \(2009\)](#) have limited pure pitch-angle scattering delay times to around 1 minute, much shorter than the observed delays of tens of minutes. However, using a different fluctuation spectrum, simulations of electron transport under the influence of pitch-angle scattering have been shown to be extremely successful at reproducing particle flux observations at Earth (e.g. [Dröge et al., 2014](#)). These models have been used to back-trace the population to the Sun to determine the injection history of the electrons ([Agueda et al., 2008, 2009, 2014](#); [Agueda & Lario, 2016](#)).

In [Agueda et al. \(2014\)](#), the inferred electron injection histories were compared with type-III timings, Geostationary Operational Environmental Satellite (GOES) Soft X-ray (SXR) flux, and (where available) 12-25 keV HXR flux. However, while a temporal correlation between HXR lightcurve and injection history of high energy electrons would be expected, in most cases a better correlation with SXR flux was found ([Agueda et al., 2014](#)). This leaves the question open as to whether the electrons observed at 1 AU are part of the same population which produced the HXR burst, as should be expected based upon radio and HXR burst timings.

While previous work focusses on matching the time-intensity and anisotropy of in-situ detected electrons to models to derive the injection history of particles at the Sun, we seek to test the theory that the HXR producing, type-III producing, and observed electrons are all from the same population. This theory is tested by using inferred properties of electrons (i.e. timings, spectra) at the Sun to initialise simulations, and comparing the predicted flux at 1 AU with observations.

In this chapter, we model the transport of solar flare electrons to a near-Earth spacecraft using a momentum and distance dependent form of scattering, and include the effects of adiabatic focussing. We use inferred electron spectra at the Sun and

injection timings from solar flare HXR observations to initialise simulations, and compare the near-Earth time-intensity, anisotropy, and spectrum, in order to constrain the scattering parameter space. Through direct comparison between simulations and observation, a mean distance and momentum dependence of electron mean-free path is obtained, and compared to previous studies.

In Section 2.2 we introduce the methods used to analyse events, and discuss the numerical model used to transport electrons from the Sun to a near-Earth satellite in Section 2.3. We go on to compare the results of our simulations to observations in Section 2.5. Finally, in Section 2.6 we discuss the results of our work, and draw conclusions as to the state of the interplanetary medium at the time of the solar flares analysed.

2.2 Event Selection and Data Analysis

An initial list of 28 electron events at 1 AU was selected, of which 16 had previously been studied by [Krucker et al. \(2007\)](#). From these 28 events, the list was narrowed down using the Reuven Ramaty High Energy Solar Spectroscopic Imager (RHESSI; [Lin et al., 2002](#), see §1.7.3). Although RHESSI is capable of detecting X-ray and γ -ray bursts from 3 keV – 20 MeV, we only used 10 keV – 100 keV HXR observations to infer the properties of solar energetic electrons, due to high background at higher energies.

We applied the criterion that, for an event to be comparable with simulations, the high energy component of each observed HXR burst associated with an in-situ measurement must be ≤ 1 minute long. To check connection between HXR bursts and in-situ electron measurements, we limited events to those which featured a co-temporal type-III radio burst, observed with the *WAVES* instrument aboard the Wind spacecraft (§1.7.1). Applying these criteria, the number of events was reduced to 14.

One event kept in the list (2010-10-20) featured no RHESSI observations, but short-duration electron flux with a well defined type-III burst was observed. This was included in the list due to the relatively easy determination of the injection time from radio observations, although no comparison of the electron spectrum at the Sun and

near Earth was possible.

2.2.1 Electron Analysis

The in-situ measurements were obtained from the *3 Dimensional Plasma Solid State Telescopes* aboard the Wind spacecraft (Wind/*3DP* §1.7.1). Each in-situ event consisted of 1.5 hours of minute-averaged data, covering an energy range of 25-400 keV in 6 energy channels. Due to high background/low flux, data from the highest energy channel was not used, leaving only the lowest 5 energy channels (25–230 keV) for analysis.

Working with the electron observations oriented away from the Sun, the unidirectional (anti-sunward) intensities, pitch angle distributions (PAD), peak flux spectra, and timings were found for each event.

The peak flux spectrum was found by taking the maximum flux in every energy channel, and comparison with the X-ray spectral index can give information about both the injection history of the electrons, and the conditions of the interplanetary magnetic field. Generally, the peak flux was well fitted by a broken powerlaw, with a low spectral index below the 40 keV, and a higher spectral index above 40 keV.

A complication in finding the peak-flux spectrum arose due to the spatially varying nature of both the Wind spacecraft, and the solar magnetic field. As Wind moves, it can leave and re-enter a flux tube which is magnetically connected to the solar flare (Mazur et al., 2000). Because of this, the flux in every energy channel passing the spacecraft can vary greatly over short periods of time (see Figure 2.1). This effect is known as a ‘dropout’, and it present in three of our selected events, changing the peak-flux spectrum considerably.

Next, the rise times of the observations were considered. In order to remove issues due to dropouts, the peak time was found by eye, and compared to the observed time of maximum. Unfortunately, due to the low time resolution of the observations, this gave ~ 1 minute uncertainties on the peak-time. In some cases, due to noisier profiles, the time of maximum flux looked to be slightly offset from the ideal peak time

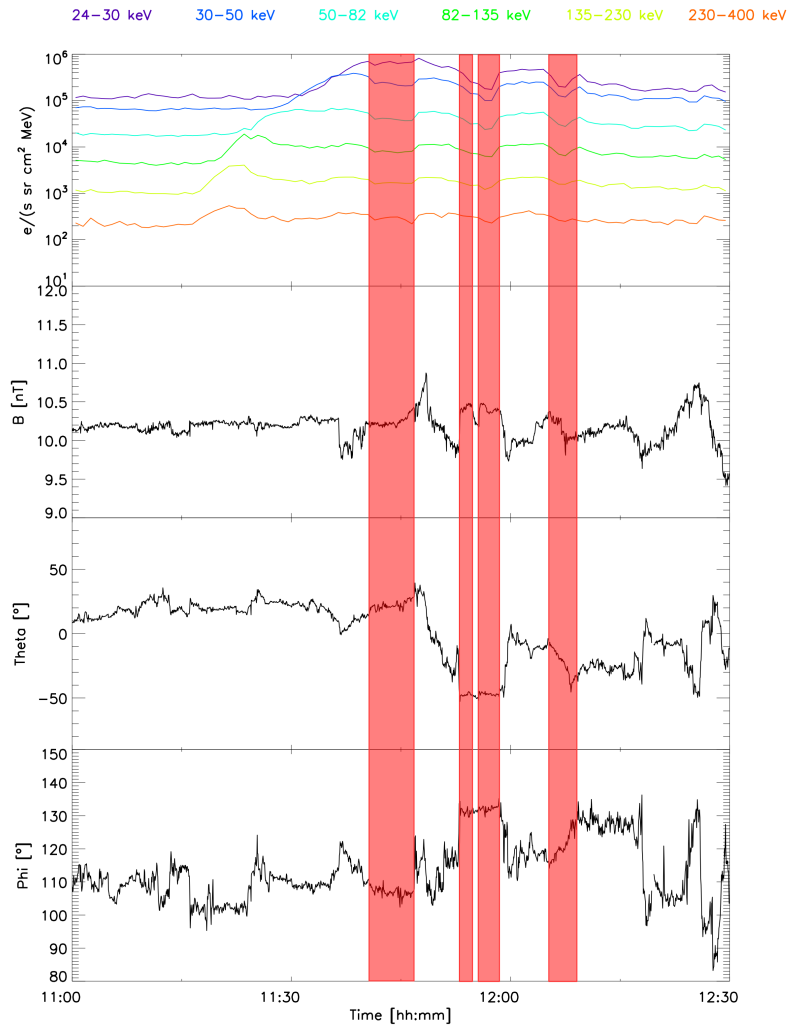


Figure 2.1: (**top - bottom**) Electron flux passing Wind on the 20th of February 2002, in-situ magnetic field strength, and magnetic field latitudinal and longitudinal directions, θ and ϕ . Simultaneous dropouts occur in all energy channels due to the relative movement of the spacecraft through areas of differing magnetic configuration. The shaded red areas highlight times of electron dropout.

(accounting for noise). However, to reduce complexity in finding the peak time, the time of maximum was used in almost all cases. The rise time for the electron flux was subsequently found as the time difference between the onset time (where the flux

reaches half of its maximum value) and the peak time.

Finally, the delay time was found. We used two distinct methods (see Figure 2.2), the first of which found the difference between the onset time of the flux and the expected onset time, assuming free-streaming electrons moving along a Parker Spiral. In calculating the expected onset time, we assumed the electrons travel a distance of 1.2 AU (the nominal distance along a Parker spiral line from the Sun to Earth), and assume the electrons travel at the mean detector channel energy. To reduce uncertainty in onset time, the onset time was here defined as the time of half-maximum, as opposed to $3\times$ the background level used in other work. However, while this should in theory give us the delay time for the first arriving electrons, the results can be greatly affected by data dropouts, high background levels, or low energy detector contamination, and so a second method of analysis was used in conjunction with this to find the delay time.

In sufficiently strong events, the peak flux is unaffected by either detector contamination or high levels of background electrons, and so we found the second delay time ('peak-delay') through the difference between the expected arrival time and the peak time. Both methods show the difference between the observed and predicted onset time of flux, based upon the assumption of free-streaming. However, due to relatively high background level/low peak-flux, in all events the peak-delay was preferentially taken over the onset delay, providing a less variable measure of the total delay and reducing the propagation of errors.

These observable quantities gave a set of parameters which could be easily compared with simulated values, in order to assess a model's effectiveness.

2.2.2 HXR Spectral Analysis

The HXR peak time was found from the 25-50 keV lightcurve, and the data was sorted into bins of width [0.33,1,5] keV within the boundaries of [3-15,15-100,100-300] keV, respectively. Generally, the spectrum was only fit between 10-100 keV, due to RHESSI's attenuation state in high countrate events affecting the low energy flux, and

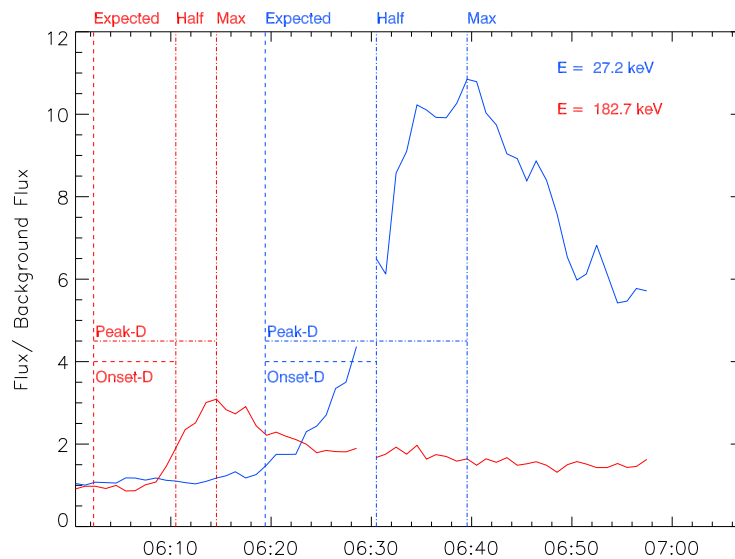


Figure 2.2: Electron flux passing Wind on the 25th of April 2002, normalised to the background flux. The lowest energy and highest energy flux channels are shown (~ 27 and ~ 182 keV), along with vertical lines showing the expected time of arrival, time of half maximum, and time of maximum flux. The horizontal lines show the Peak-Delay time, and the Onset-Delay time.

high background affecting the high energy flux.

The spectrum of the solar flare electrons was inferred from RHESSI observations by fitting the HXR spectrum with a thermal distribution (*vth* in *OSPEX*), and adding an additional powerlaw distribution via the *thick2* (thick-target) (e.g. [Holman et al., 2003](#)) and *thin2* (thin-target) distributions in the *OSPEX* package. To account for reflection of photons off the solar surface, an additional *albedo* component ([Kontar et al., 2006](#)) was included in fits. An example of this is shown in Figure 2.3 for the 2002-04-25 event, with a thin-target fit ([Brown et al., 2003](#)) to the peak flux spectrum.

For every event, the HXR model parameters were varied until the chi-squared goodness-of-fit parameter was minimised, giving the solar electron peak-flux spectrum. As there were many degrees of freedom in each model, the best-fit model was often relatively close to alternative models in terms of goodness-of-fit. While this could lead possible errors in the inferred electron spectrum, and hence problems with any

comparison with the in-situ electron spectrum, by ensuring that each fit was performed multiple times, starting from a range of guess parameters, the model which produced the minimum chi-squared value was robustly shown to be the best fit to observations.

For cases where the choice of best-fit parameters was more ambiguous, there was a risk of propagation of errors, as any variation in the model used to infer the electron spectrum would affect the degree to which the simulation output agreed with observations. This was reduced in part due to the fairly large uncertainties in near-Earth electron peak-flux spectrum (due to *Wind*/*3DP*'s wide energy bins), allowing for some variation of inferred solar electron spectrum and hence a wider range of acceptable parameters. However, any large differences in inferred electron spectrum (e.g. a change in δ_{high} of ~ 2 or more) would be noticeable in the simulated 1 AU spectrum; leading to disagreement between simulations and observations. Hence, by using a wide range of starting values for the HXR fitting procedure, and checking whether the predicted spectra fell within the uncertainty range of observed spectra, propagation errors due to false model selection were minimised.

Wind electron observations were well fit by a broken powerlaw with a break energy of around 40 keV. Similarly, HXR observations tended to feature a spectral break at around ~ 50 keV, with a steeper slope above the break. Using the inferred solar electron spectrum, the >40 keV electron spectral index was used as initialisation in simulations, while the lower energy electron channels were normalised to data (see §2.3). Both thick and thin target peak flux spectra at Earth were calculated and compared to observations, in order to find the higher spectral index.

2.3 Interplanetary Transport of Flare Electrons

As electrons traverse the interplanetary medium, multiple interactions occur with both the particles and the waves inhabiting the medium. Close to the solar surface, high energy (> 40 keV) electrons are subject to collisions with the background plasma, while further away from the Sun the medium is generally too diffuse for either Coulomb collisions or Langmuir wave generation (Kontar & Reid, 2009), meaning that electrons

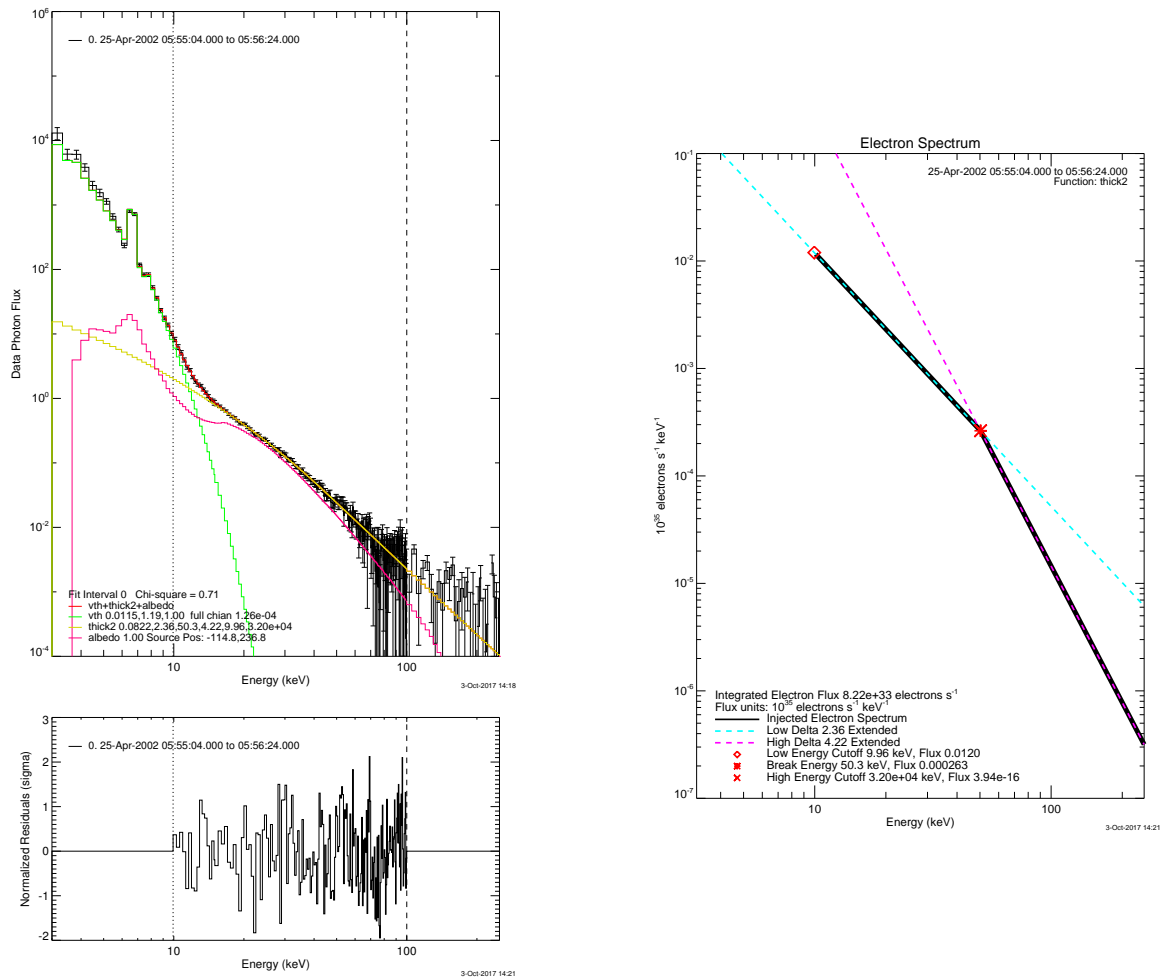


Figure 2.3: **(top, left)** Photon flux for the 2002-04-25 event, measured by RHESSI. Black shows data + uncertainties, green shows thermal fit, yellow shows thick-target fit, purple shows albedo correction, and red shows combined spectrum. The values at the bottom show the parameters used to best fit the observed spectrum (see §1.7.3 for a list of parameters used). **(bottom, left)** Normalised residuals for the fit. **(right)** Reconstructed thick-target electron flux.

are primarily scattered by small-scale magnetic fluctuations (Jokipii, 1966).

A well documented break in the in-situ electron spectrum is often observed around 40-50 keV (Lin, 1985; Krucker et al., 2007), which has been attributed to Langmuir wave generation modifying the low-energy (< 40 keV) electron distribution, leading to a flattening of the spectrum below the break energy (Kontar & Reid, 2009). Above

the break, however, the spectrum remains unchanged by any resonant Langmuir wave generation/absorption.

In modelling the passage of high energy electrons from a flare location to a near-Earth spacecraft, we ignore both particle-particle collisions and the generation/absorption of Langmuir waves, assuming that the electrons are most affected by scattering from a turbulent magnetic field (Roelof, 1969; Dröge et al., 2014).

2.3.1 Transport Model

The transport of electrons from a flare to Earth is assumed to be guided one dimensionally along the magnetic field. We make this assumption due to the low electron momenta sticking particles to a field line (e.g Dalla et al., 2017), allowing for only movement *along* the field, rather than across it. A one dimensional Fokker-Planck focussed transport equation was used to model the electron passage, given by (e.g. Roelof, 1969; Agueda et al., 2014)

$$\underbrace{\frac{\partial f}{\partial t} + \mu v \frac{\partial f}{\partial z}}_{\mathbf{a}} + \underbrace{\frac{v(1-\mu^2)}{2L_z} \frac{\partial f}{\partial \mu}}_{\mathbf{b}} - \underbrace{\frac{\partial}{\partial \mu} \left[D_{\mu\mu} \frac{\partial f}{\partial \mu} \right]}_{\mathbf{c}} = \underbrace{Q(t, z, v, \mu)}_{\mathbf{d}}, \quad (2.1)$$

where $f = f(v, \mu, z, t)$ is the electron phase space density (or ‘distribution function’), and t and v are time and electron velocity, respectively. The distance along the field line is given by z , and the cosine of the electron’s pitch angle is given by μ .

This equation describes the injection and subsequent evolution of an electron population along a one-dimensional magnetic field line, directed radially away from the Sun. This model accounts for adiabatic focussing and pitch angle scattering. Here, the identified terms are: **(a)** convection of the electron population along the field line, **(b)** focussing of the electrons along the field line, **(c)** pitch angle scattering of the electrons, and **(d)** the source term of the electrons at the Sun.

Adiabatic focussing **(b)** arises due to the combination of the weakening of the magnetic field with distance and the conservation of an electron’s magnetic moment as it travels along the field. Due to this conservation, an electron’s velocity parallel

to the B-field will increase, while its perpendicular velocity will decrease. Here, it is assumed that the magnetic field will decrease as $B(z) \propto z^{-2}$. The length scale over which this change occurs is defined by the focussing length $L_z(z) = B(z)/(-dB/dz)$ (Roelof, 1969), given here as $L_z = z/2$.

Here we have made the assumption that magnetic field (and hence path the electron population travels along) is directed radially away from the Sun, rather than a curved Parker Spiral field line. This simplification is possible because of the dominance of scattering (which depends upon length along the field line rather than radial distance from the Sun) over focussing in our simulations.

The Sun's magnetic field is extremely turbulent, featuring fluctuations on all length scales. If these fluctuations are on the same scale as an electron's gyroradius, then travelling electrons will resonantly interact with them, resulting in an energy transfer between the fluctuations and the electrons. As an initially beamed electron population travels along a magnetic field, repeated interactions between the fluctuations and travelling electrons will result in the diffusion of the electron population.

To describe this, we assume that magnetic fluctuations form a powerlaw distribution in spatial wavenumber and are frozen into the magnetic field (i.e. are static). Under these assumptions, the quasilinear diffusion coefficient was derived by Jokipii (1966), and subsequently modified by Beeck & Wibberenz (1986). This is given by

$$D_{\mu\mu} = \frac{3v}{2\lambda_{\parallel}(4-q)(2-q)}(1-\mu^2)(|\mu|^{q-1} + h), \quad (2.2)$$

where λ_{\parallel} is the parallel scattering mean-free path, and q is the spectral index of magnetic field fluctuations, taken as a Kolmogorov spectrum, $q = +5/3$. This is roughly the spectral index of measured fluctuations within the inertial range (Podesta et al., 2007), and this is the commonly used value for q used within the literature (e.g. Agueda et al., 2009; Dröge & Kartavykh, 2009). However, it must be noted that, although this value of q is measured within the inertial range, this is not the case further down the spectrum (at smaller wavelengths). Measurements of the magnetic fluctuation spectrum from the inertial range up to the solar wind proton gyroradius

scale have found a general steepening of the fluctuation spectrum up to around $q \approx 6/3 \rightarrow 7/3$ (Bruno & Telloni, 2015). As the electrons modelled in this work (up to 180 keV electrons) lie within the proton gyroradius scale (the scale extends to the 1 keV proton gyroradius scale, giving the electron-to-proton gyroradius ratio as $r_{ge}/r_{gp} \in [0.15, 0.31]$), it could be argued that a value of $q \in [2, 7/3]$ would be more appropriate for modelling. However, to keep consistency with previous literature, the value of $q = +5/3$ was kept.

The constant h was added to resolve the ‘resonance gap’ where scattering is greatly reduced at $\mu = 0$, and accounts for effects such non-static magnetic fluctuations (Fedorenko, 1983; Schlickeiser, 1989), resonance between particles and magnetic fluctuations (Palmer, 1982; Bieber et al., 1994; Dröge, 2000; Bian et al., 2012), and binary collisions between particles (Kontar et al., 2014). As these effects are expected to be negligible outside of the Sun, a small value of $h = 0.01$ is chosen (similar to the $h = 0.05$ used in Dröge & Kartavykh, 2009).

We further modify Equation (2.2) through an added dependence of the mean free path upon the electrons’ distance from the Sun and momentum. This is given by,

$$\lambda_{\parallel}(z, p) = \lambda_{\parallel, \oplus} \left(\frac{z}{z_{\oplus}} \right)^{\kappa} \left(\frac{p}{p_0} \right)^{2\alpha}, \quad (2.3)$$

where p is electron momentum, p_0 is the momentum of the lowest energy particles (27 keV) modelled, z_{\oplus} is the position of the near-Earth satellite, and $\lambda_{\parallel, \oplus}$ is the strength of scattering of the lowest energy particles at the scattering. The distance dependence of scattering is limited to $\kappa > 0$, in order to match analysis of Helios data by Ruiz et al. (2011), who found a general increase in parallel mean free path with distance. No assumptions on the range of α are made.

2.3.2 Injection Profile

Finally, part **d** describes the injection of the electron population near the Sun. As the Wind data used here is minute averaged, the mean solar wind speed of $\sim 400 \text{ km s}^{-1}$ reduces our effective ‘spatial resolution’ to $\sim 24 \text{ Mm}$; larger than the average solar

flare. Accordingly, in our simulations we assume that the flare is sufficiently small that the assumption of injected at a point in space holds. We also assume that the electron population is initially beamed away from the Sun.

Particles travelling towards the Sun will likely interact with the background plasma, losing their energy via collisions, resulting in the production of HXR bursts (Holman et al., 2011). As we are only concerned with the escaping particles (which are detected at 1 AU), particles scattered to below a distance of 0.04 AU are removed from our simulations.

The time profile of the injected electrons was modelled by a Gaussian, based upon 50 – 100 keV RHESSI X-ray observations. In order to match the general *flattening* and *steepening* of the flux spectrum observed in flares (Dennis, 1985; Holman et al., 2011), the velocity distribution of injected electrons was set to be dependent upon time (Figure 2.4).

Using these descriptions, the injection function was given by

$$Q(t, z, v, \mu) = \delta(z - z_0)\delta(\mu - \mu_0)e^{-\frac{(t-t_0)^2}{\tau^2}} \left(\frac{v}{v_0}\right)^{-\delta_{v,0}\frac{(t-t_0)^2}{\tau^2} - \delta_{v,0}}, \quad (2.4)$$

where all electrons are injected at a distance of $z_0 = 0.05$ AU from the Sun with pitch angle cosine $\mu_0 = 1$ (i.e. beamed in the anti-sunwards direction). The peak injection time t_0 , Gaussian width τ , and peak velocity spectral index $\delta_{v,0}$ are determined by the RHESSI observations. Finally, $v_0 = \sqrt{2E/m_e}$ was chosen as the velocity of the lowest energy channel in our simulations (~ 27 keV). This was normalised to the total number of injected pseudo-particles in each energy channel by $N_{tot} = \int_0^\infty Q(t, z, v, \mu)dt$.

2.3.3 Numerical Scheme

Using the methods derived by Gardiner (1985) and used by MacKinnon & Craig (1991); Dröge et al. (2014), for example, Equation (2.1) was transformed into equivalent stochastic differential equations determining the evolution of a pseudo particle's position and pitch angle:

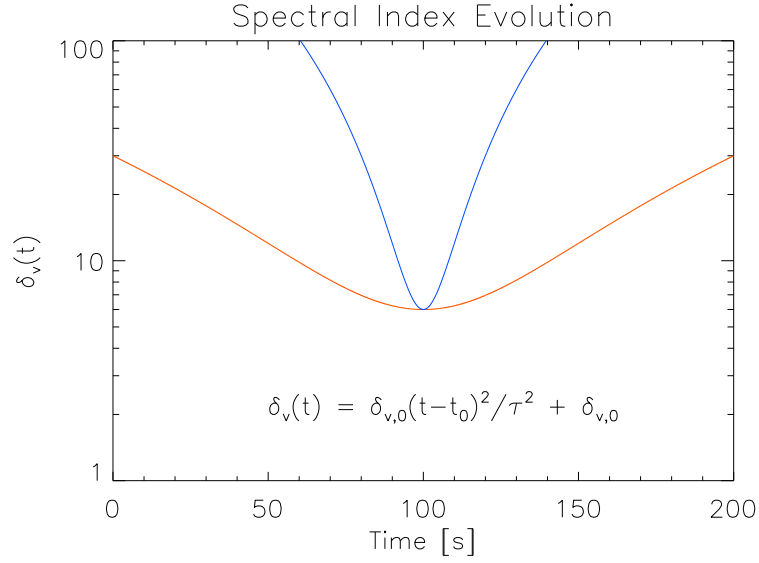


Figure 2.4: Velocity spectral index evolution of injected electrons near the sun. Here, $\delta_{v,0} = 6$ (red + blue), $t_0 = 100$ s (red + blue), $\tau = 50$ s (red) and $\tau = 10$ s (blue).

$$z_{i+1} = z_i + \mu_i v \Delta t, \quad (2.5)$$

$$\mu_{i+1} = \mu_i + \left(\frac{dD_{\mu\mu,i}}{d\mu} + \frac{v(1 - \mu_i^2)}{2L_{z,i}} \right) \Delta t + \sqrt{2D_{\mu\mu,i}\Delta t} \xi. \quad (2.6)$$

The subscript i denotes the simulation time-step, and $\xi \in \mathcal{N}(0, 1)$ represents a random variable drawn from a normally distributed pool of mean 0, and variance 1. Every pseudo-particle was tracked through the simulation using Equations (2.5) and (2.6), and the properties of the phase-space density were found through the ensemble properties. To ensure numerical stability, the simulation step size was taken as $\Delta t = (\lambda_{\parallel}/v)/100$, where λ_{\parallel}/v is the diffusive timescale. Finally, the pitch-angle cosine was constrained to $\mu \in [-1, 1]$ via the addition of reflective boundaries.

2.4 Numerical Simulation Verification

No non-trivial analytical solution of Equation (2.1) exists, leading to a problem in confirming any numerical results produced. However, by simplifying the equation, different parts can be checked analytically.

2.4.1 Diffusion Term

To confirm the diffusion term in Equation (2.1), the source and focussing terms were removed, and the distribution was integrated spatially. Applying these changes, and defining $F(t, \mu) = \int_{-\infty}^{\infty} f(t, z, \mu) dz$ gave the equation (e.g. [Shalchi, 2006](#))

$$\frac{\partial F}{\partial t} = \frac{\partial}{\partial \mu} \left[D_{\mu\mu} \frac{\partial F}{\partial \mu} \right], \quad (2.7)$$

where here we consider a simplified diffusion coefficient, given by $D_{\mu\mu} = (1 - \mu^2)/2\tau$. It has been shown by [MacKinnon & Craig \(1991\)](#); [Shalchi \(2006\)](#) that, when the ansatz $F(t, \mu) = \varsigma(t) \cdot P(\mu)$ is applied (where $\varsigma(t) = \exp(-\omega t)$), then Equation (2.7) can be solved with the series

$$F(t, \mu) = \sum_{n=0}^{\infty} \left(n + \frac{1}{2} \right) P_n(\mu_0) P_n(\mu) e^{-\frac{n(n+1)t}{2\tau}}. \quad (2.8)$$

Here, the function $P_n(\mu)$ is a Legendre polynomial, given by $P_n(\mu) = (2^n n!)^{-1} \frac{d^n}{d\mu^n} (\mu^2 - 1)^n$ ([Bird, 2014](#)), and the initial condition $F(0, \mu) = \delta(\mu - \mu_0)$ is applied. We compared this solution with our numerical simulation of Equation (2.7) to confirm that our results were reasonable, and found increasing agreement to the simplified model with time (Figure 2.5), due to the highly oscillatory solution at low t .

2.4.2 Source Term

The numerical solution of the source term in Equation (2.1) was confirmed by removing the diffusion and focussing terms, leaving a simple advection equation:

$$\frac{\partial f}{\partial t} + \mu v \frac{\partial f}{\partial z} = \delta(z) \delta(\mu - \mu_0) e^{-\frac{(t-t_0)^2}{\tau^2}} \tilde{v}^{-\delta_{v,0}} \frac{(t-t_0)^2}{\tau^2}^{-\delta_{v,0}}, \quad (2.9)$$

where $\tilde{v} = v/v_0$ is simply the normalised particle velocity. Through the method of characteristics, this can be solved to find

$$f = \frac{\delta(\mu - \mu_0)}{\mu v} \tilde{v}^{-\delta_{v,0}} \left(\frac{z/(\mu v) + t_0 - t}{\tau} \right)^2^{-\delta_{v,0}} e^{-\left(\frac{t_0 - t + z/(\mu v)}{\tau} \right)^2} \left(\Theta \left(\frac{z}{\mu v} \right) - \Theta \left(\frac{z}{\mu v} - t \right) \right), \quad (2.10)$$

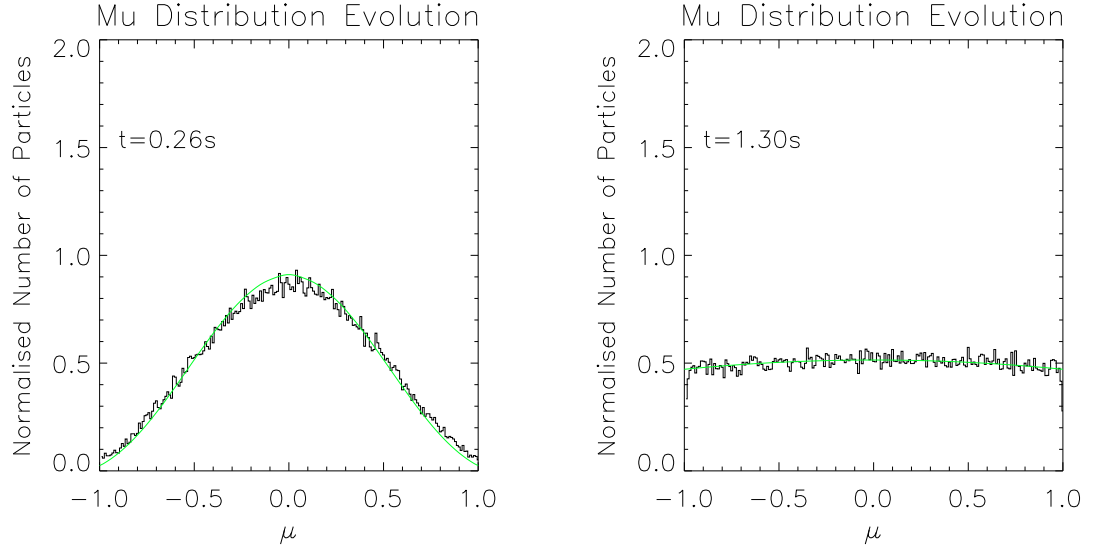


Figure 2.5: Results for a simplified pitch-angle scattering model (Eqn. 2.7), showing the analytical solution (green) and numerical solution (black solid) for two different times. The distribution was initialised with $\mu_0 = 0$, $\tau = 1$ s, and the numerical solution was solved using 5×10^5 pseudo-particles.

where $\Theta(\dots)$ is the Heaviside step function, defined as

$$\Theta(x) = \begin{cases} 1 & x > 0, \\ \frac{1}{2} & x = 0, \\ 0 & x < 0. \end{cases} \quad (2.11)$$

For the stochastic simulation, Equation (2.9) was integrated in time, giving the number of pseudo-particles injected in each timestep as

$$N = \frac{2N_{tot}\sqrt{1 + \delta_{v,0} \ln |\tilde{v}|}}{\tau\sqrt{\pi}(1 + \frac{t_0}{\tau}\Phi(\sqrt{1 + \delta_{v,0} \ln |\tilde{v}|}))} \tilde{v}^{-\delta_{v,0}(\frac{t-t_0}{\tau})} e^{-(\frac{t-t_0}{\tau})^2} \delta(\mu - \mu_0)\delta(z - z_0), \quad (2.12)$$

where $\Phi(\dots)$ is the error function, defined as

$$\Phi(t) = \frac{2}{\sqrt{\pi}} \int_0^t e^{-t'^2} dt'. \quad (2.13)$$

The simplified advection simulation was run, and both the spatial distribution and flux measured at a point were compared to analytical values. These were found to be

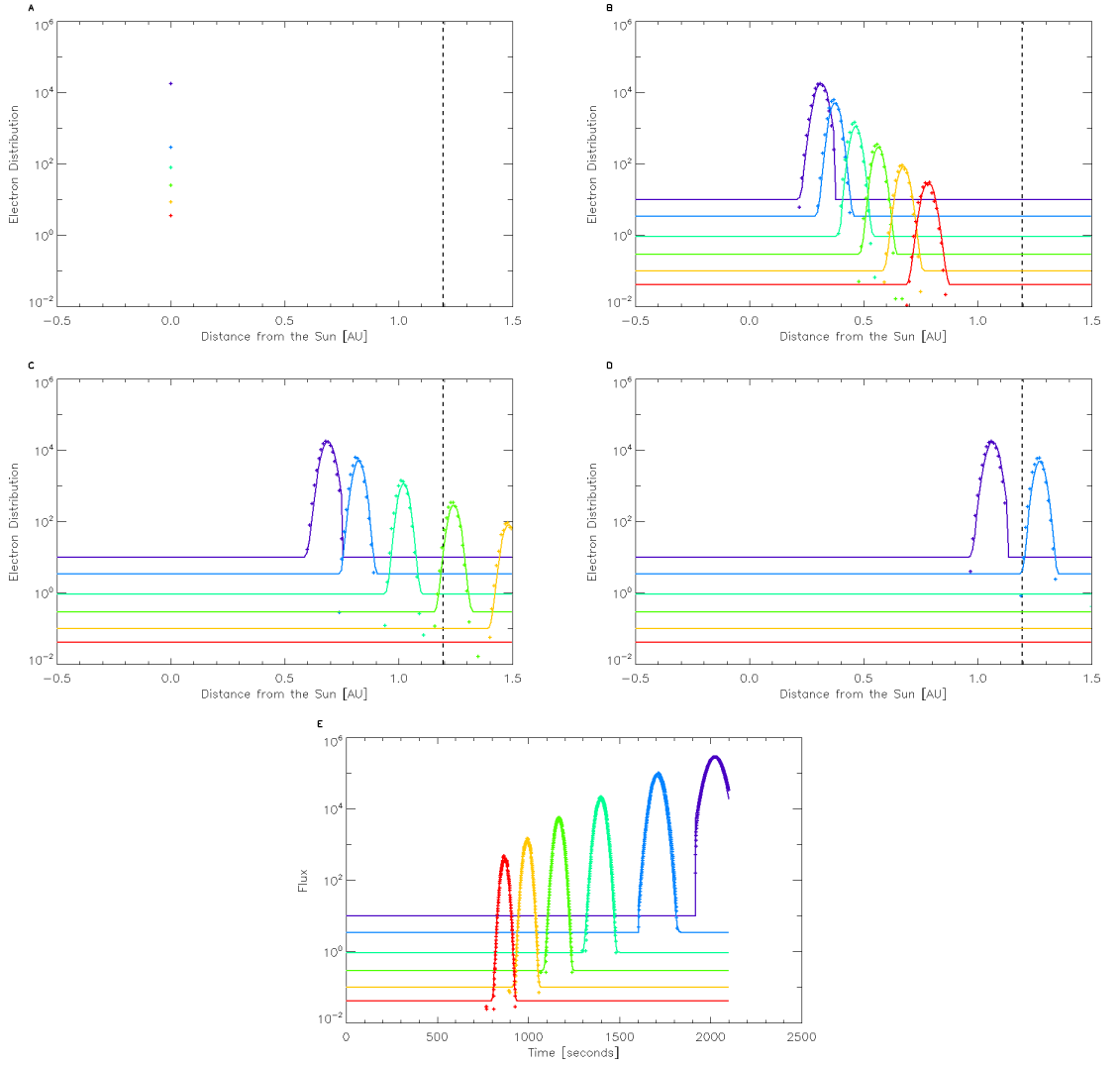


Figure 2.6: Results for a simplified pure advection model, with source term (Eqn. 2.10). (A – D) Analytical (solid) and numerical solutions (crosses) for the spatial distribution of pseudo-particles at four different times. The different colours represent different velocities (corresponding to the Wind/*3DP* energy channels used), and the vertical dashed line shows the position at which the passing flux was measured. (E) Analytically calculated flux (solid) and numerically obtained flux values (crosses). Simulations were run with parameters $t_0 = 100$ s, $\tau = 50$ s, and $\delta_{v,0} = 6$.

in agreement with each other, confirming the injection term used (Figure 2.6).

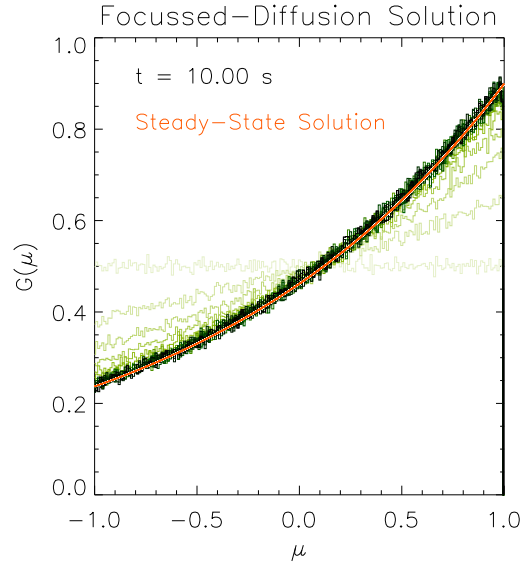


Figure 2.7: Steady-state results for a simplified focussed diffusion model (Eqn. 2.16), showing analytical solution (red), with numerical results (coloured). The histogram shade represents the simulation time, from $t = 0$ s (pale) to $t = 10$ s (black). To obtain the numerical solution, 5×10^5 pseudo-particles were used, with scattering and focussing parameters $\tau = 1$ s, $dt = 10^{-3}$ s and $L_z = 10^{-3}$ AU.

2.4.3 Focusing Term

Finally, the adiabatic focussing term in Equation (2.1) was checked for consistency. Following Kunstmann (1979); Wang & Qin (2016); Lasuik et al. (2017), we define a particle distribution $\tilde{f}(t, z, \mu) = f(t, z, \mu) \exp(z/L_z)$, where the factor $\exp(z/L_z)$ arises from the conservation of magnetic flux in an expanding flux tube. With this new phase-space density function, the source-free version of Equation (2.1) can be written as (Lasuik et al., 2017)

$$\frac{\partial \tilde{f}}{\partial t} + \mu v \frac{\partial \tilde{f}}{\partial z} + \frac{v}{2L_z} \frac{\partial}{\partial \mu} \left[(1 - \mu^2) \tilde{f} \right] = \frac{\partial}{\partial \mu} \left[D_{\mu\mu} \frac{\partial \tilde{f}}{\partial \mu} \right], \quad (2.14)$$

where the scattering is again assumed to be isotropic ($D_{\mu\mu} = (1 - \mu^2)/2\tau$). If both the diffusion and focussing terms are spatially independent, then Equation (2.14) can be simplified via spatial integration (Lasuik et al., 2017). Again, by defining $F(t, \mu) = \int_{-\infty}^{\infty} \tilde{f}(t, z, \mu) dz$, the transport equation becomes

$$\frac{\partial F}{\partial t} + \frac{v}{2L_z} \frac{\partial}{\partial \mu} [(1 - \mu^2)F] = \frac{\partial}{\partial \mu} \left[D_{\mu\mu} \frac{\partial F}{\partial \mu} \right]. \quad (2.15)$$

The steady-state solution of this is defined as $G(\mu) = \lim_{t \rightarrow \infty} F(t, \mu)$, yielding the differential equation

$$\frac{v}{2L_z} \frac{\partial}{\partial \mu} [(1 - \mu^2)G] = \frac{\partial}{\partial \mu} \left[D_{\mu\mu} \frac{\partial G}{\partial \mu} \right], \quad (2.16)$$

with the solution

$$G(\mu) = C_0 e^{\frac{\mu v \tau}{L_z}}, \quad (2.17)$$

where C_0 is a constant. This solution was compared to numerical results for combined diffusion-focussing models (Figure 2.7), and the two were found to be in good agreement.

2.5 Model Comparison and Results

Every observed electron event was placed into one of two categories: *Impulsive* and *Gradual* events, depending upon the FWHM duration of the electron intensity profiles at 1 AU. For most events, the simulated intensity at Earth was normalised to the peak observed intensity, and the time-intensity profiles were compared. The simulation parameters (κ , α , $\lambda_{||,\oplus}$) were cycled through all chosen values until a minimum in goodness-of-fit was achieved.

For all cases, the chi-squared value was computed, and the model which minimised chi-squared was chosen. However, due to dropouts or other instrumental effects, this often produced sub-optimal agreements between the models and observation. Hence, the best match to simulations was then determined by eye, to ensure the results of the chi-squared test were reasonable.

In three events, strong electron dropouts affected the peak-intensities in some energy channels, and so the simulated intensity was normalised to an arbitrary value in order to find the best fit with the observations. The simulated intensity was also sorted into

the eight pitch-angle bins used by Wind, in order to compare simulated and observed anisotropies.

The simulations were run multiple times, with simulation parameters κ , α , and $\lambda_{\parallel,\oplus}$ varying between $[0, 1]$, $[-1, 1]$, and $[0.3, 1.5]$ AU, respectively. Step sizes of $\Delta\kappa = 0.5$, $\Delta\alpha = 0.1$, and values of $\lambda_{\parallel,\oplus} = [0.3, 0.5, 0.75, 1.0, 1.5]$ AU were used to cover the range of κ , α , and $\lambda_{\parallel,\oplus}$.

2.5.1 Time-Intensities

Impulsive Events

For all impulsive events, both the uni-directional anti-sunward flux and the PADs were found to good agreement with observations. The overview plots for these events are shown in Figures 2.8 and 2.9, showing the comparison between uni-directional intensities and PAD, along with HXR and type-III timings and local magnetic field and solar wind properties.

As predicted, we find that the highest energy channel uni-directional intensities match best with observations, with a decrease in agreement with energy. In addition to this, the large scale features of the PAD can be seen to agree well in most cases for the highest energy channel simulated.

In the 2002-04-14 event, a reversal of polarity can be seen at roughly 22:50, where the peak intensity changes from 0° to 180° travelling electrons. This effect is attributed here to magnetic mirroring of particles from an interplanetary Coronal Mass Ejection (ICME) observed passing Earth between 2002-04-12/01:00 and 2002-04-13/13:00 (N. Agueda, personal communication).

Similarly, in the 2005-05-16 event, bidirectional electron fluxes are observed passing the spacecraft. An ICME was observed passing ACE from 2005-05-15/06:00, however it is unknown whether the sunwards travelling electrons are from the same population as the flare electron, or are from an unrelated event.

For all events, the simulated PAD is initially strongly peaked in the anti-sunward direction, but isotropises rapidly. Similarly we find that in all events, the PAD is

initially strongly peaked in the anti-sunward direction. However, the rate at which the electron distribution isotropises is extremely variable, ranging from ~ 30 minutes (e.g. 2002-04-25) to no observable change over the entire event (e.g. 2002-08-20). One possible explanation for this discrepancy is that subsequent injection of electrons into the spacecraft-linked flux tube from multiple events would cause the PAD to stay strongly anti-sunward. Further work is required to test this hypothesis.

Gradual Events

The more gradual events were also compared with simulations (Figures 2.10 and 2.11). As with impulsive events, the agreement between simulated and observed intensities tended to improve with increasing energy, with the lowest energy channels (~ 27 and ~ 40 keV) disagreeing in most events.

The rate of isotropisation remains roughly constant over these events, and is greatly reduced relative to impulsive events. Typically a weakly anti-sunward beamed distribution (between $\theta = 0 - 90^\circ$) was seen passing the spacecraft at all times after the initial detections, with only one event (2002-08-20/08:00) featuring a weak return current of sunwards travelling electrons (from around 09:10).

As with the 2002-04-14 event, an ICME was detected by the ACE spacecraft between 2002-08-19 and 2002-08-21, leading to the conclusion that the weak sunwards component observed is simply a reflected portion of the solar flare electrons.

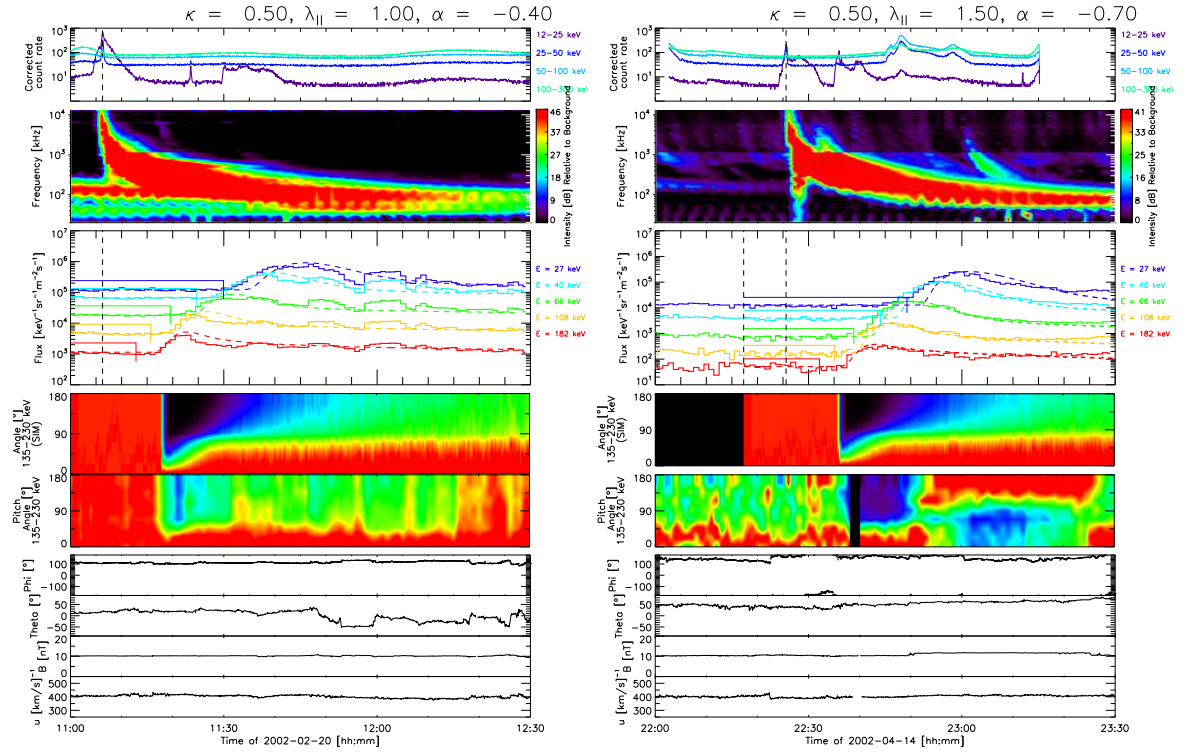


Figure 2.8: Time profiles for the 2002-02-20 (**left**) and 2002-04-14 (**right**) events. From top to bottom is shown the RHESSI corrected countrate; Wind/*WAVES* dynamic spectrum; Wind/*3DP* electron time intensity plot (solid lines), with simulated intensity overlaid (dashed lines); simulated PAD from the 182 keV channel (normalised to maximum; red = max, blue = min); observed PAD from the 182 keV channel; magnetic field latitude (θ); longitude (ϕ); strength; and solar wind velocity. The simulation parameters (κ , $\lambda_{\parallel\oplus}$, α) used to best fit observations are listed at the top of each overview plot.

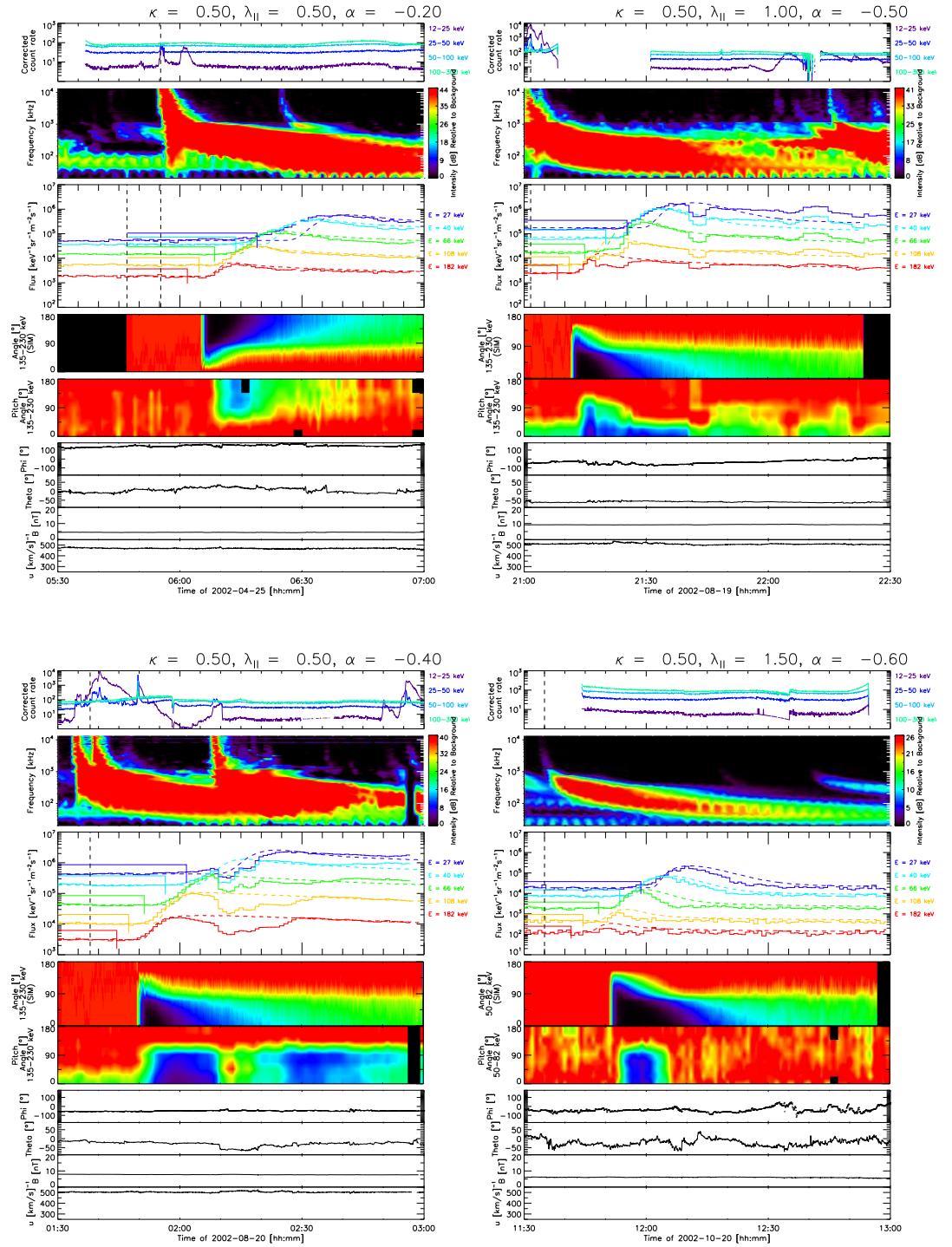


Figure 2.9: Time profiles for the 2002-04-25 (**top left**), 2002-08-19 (**top right**), 2002-08-20/01:30 (**bottom left**), and 2002-10-20 (**bottom right**) events. Figures are in the same order as Figure 2.8, except for the observed and simulated PADs for the 2002-10-20 event, where the ~ 66 keV PAD is shown due to low countrate in higher energy channels.

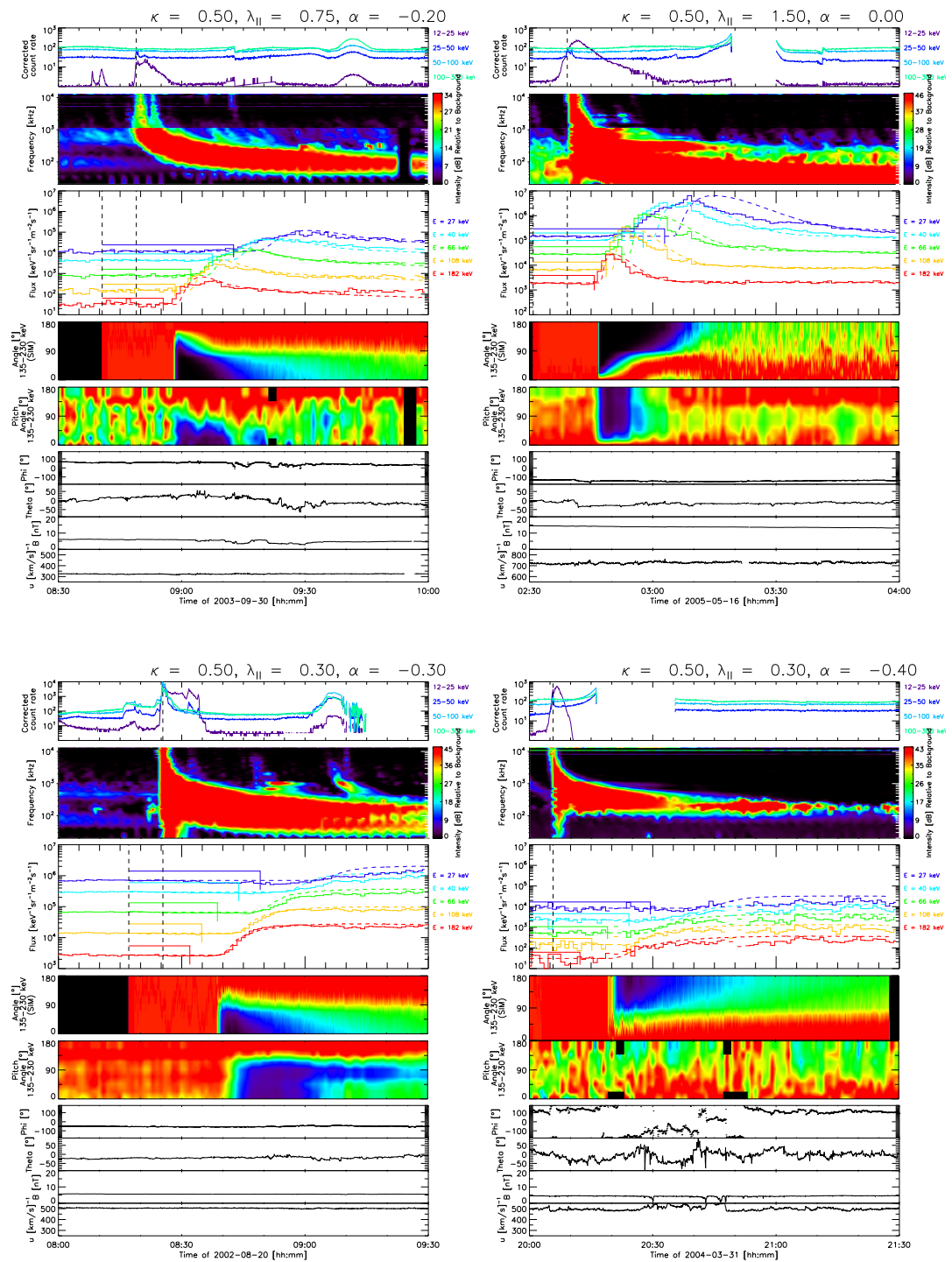


Figure 2.10: Time profiles for *impulsive* events on 2003-09-30 (**top left**) and 2005-05-16 (**top right**), and *gradual* events on 2002-08-20/08:00 (**bottom left**), and 2004-03-31 (**bottom right**). Figures are in the same order as Figure 2.8

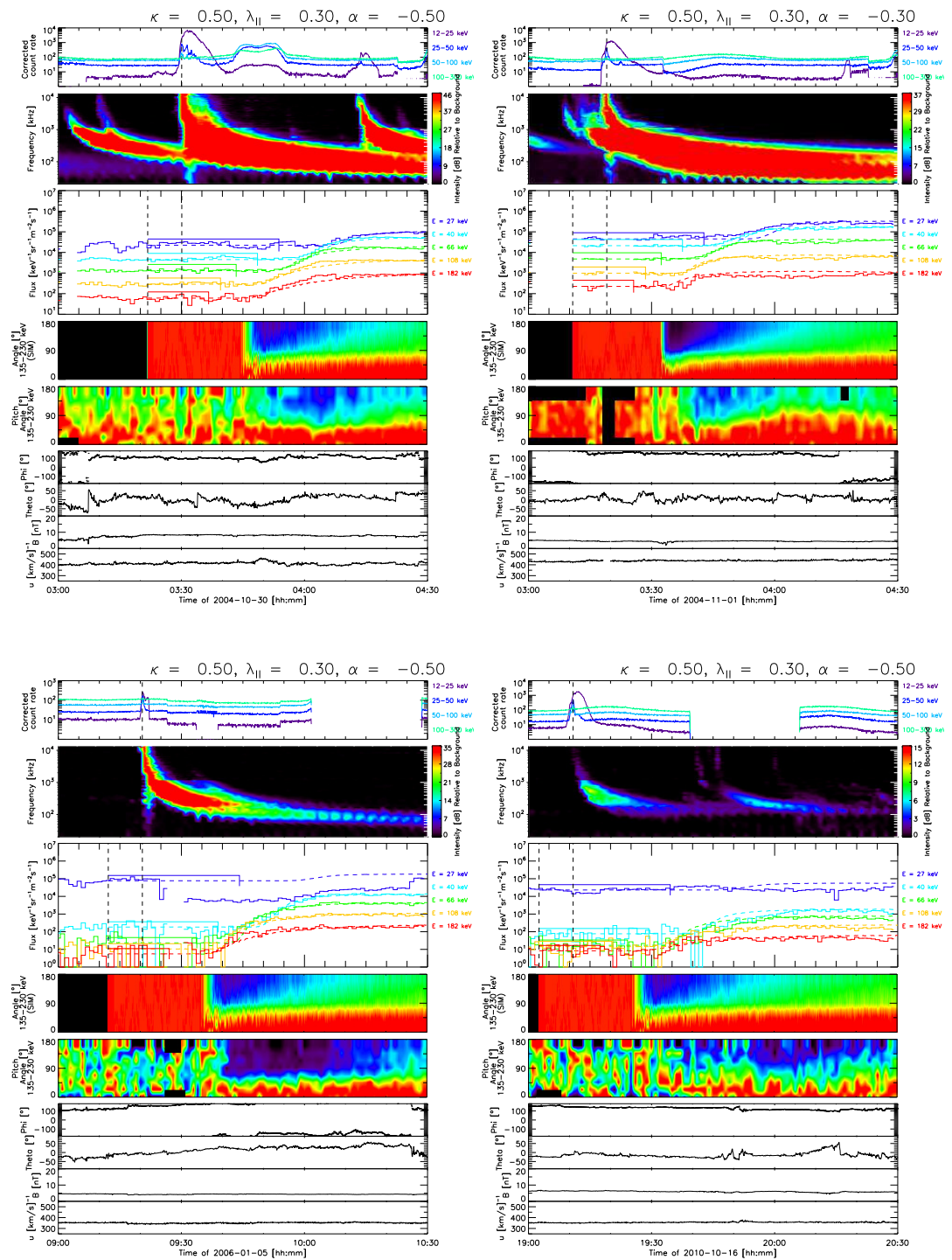


Figure 2.11: Time profiles for the 2004-10-30 (**top left**), 2004-11-01 (**top right**), 2006-01-05 (**bottom left**), and 2010-10-16 events (**bottom right**). Figures are in the same order as Figure 2.8

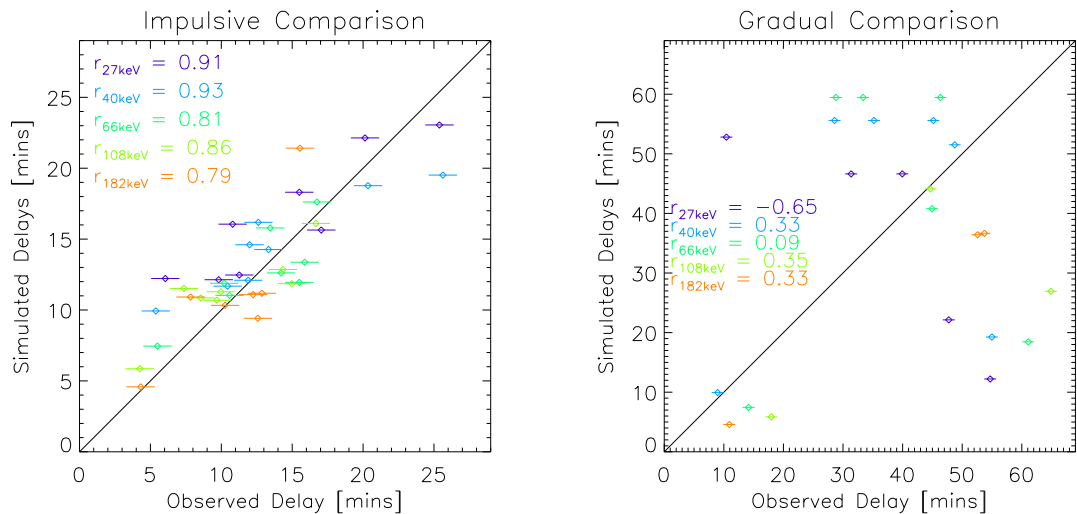


Figure 2.12: Comparison of simulated and observed delay times for impulsive (**left**) and gradual (**right**) events, colour-coded by electron energy. Uncertainties arise from the time resolution of the instruments (1 minutes). The linear-correlation coefficients for each energy ($r_{E[\text{keV}]}$) are listed for comparison. The solid black line denotes absolute agreement of simulations and observations.

Time Delays

The peak time delays were computed for both impulsive and gradual events, and the simulated and observed delays were compared. For impulsive events (Figure 2.12, left), a good correlation between simulated and observed delay was found, with higher energy delays tending to agree more than lower energy delays. However, as lower energy electrons are more strongly affected by Langmuir wave generation/absorption, it should be expected that the arrival time near Earth will not depend solely on pitch angle scattering.

For gradual events (Figure 2.12, right), despite the general agreement of simulated and observed intensities, the delay times varied up to a factor of ~ 5 . This could be due to the extremely large FWHM durations over which the events take place (nearly an hour vs ten minutes) and relatively smooth peaks leading to complications in the exact determination of the peak delay.

2.5.2 Spectral Shifts

To compare the simulated and observed spectra, the < 40 keV simulated channels were normalised to Wind measurements, while the > 40 keV channels were run using RHESSI inferred spectra as input. Both emission profiles were considered; thick-target emission, where the X-ray producing electrons lose all of their energy to the production of X-rays (Brown, 1971), and thin-target emission, where the electrons lose a minimal amount of energy to the X-rays (Section 2.2.2). As in Krucker et al. (2007), the electron peak-flux above 40 keV was represented by a single power-law, and the simulation parameters were varied until the difference between simulated and observed spectral indices was minimised.

For most impulsive events, the simulation spectra corresponding to the best-fit intensity profile agreed well with observed spectra (Figure 2.13, left), with generally more events fitting better with thin-target spectra. For the 2002-10-20 event, no RHESSI observations were available, disallowing for any spectral comparison. Similarly for the gradual events, the spectra given by the best-fit intensities generally agreed with observations (Figure 2.13, right) - although the simulated spectrum was typically harder than the observed spectrum.

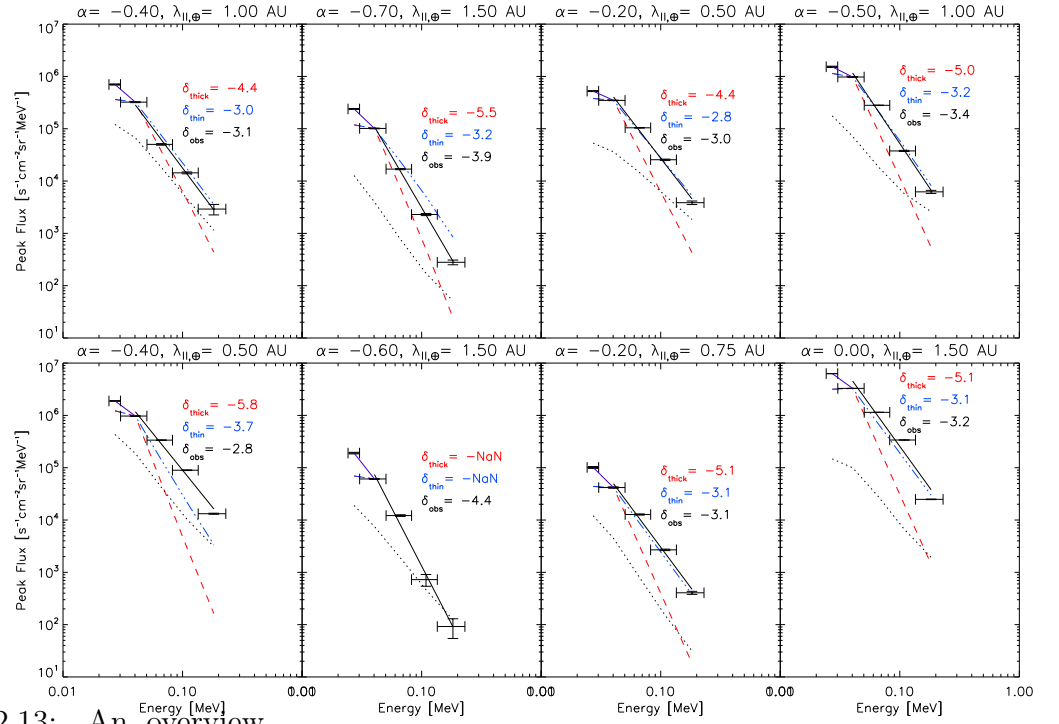
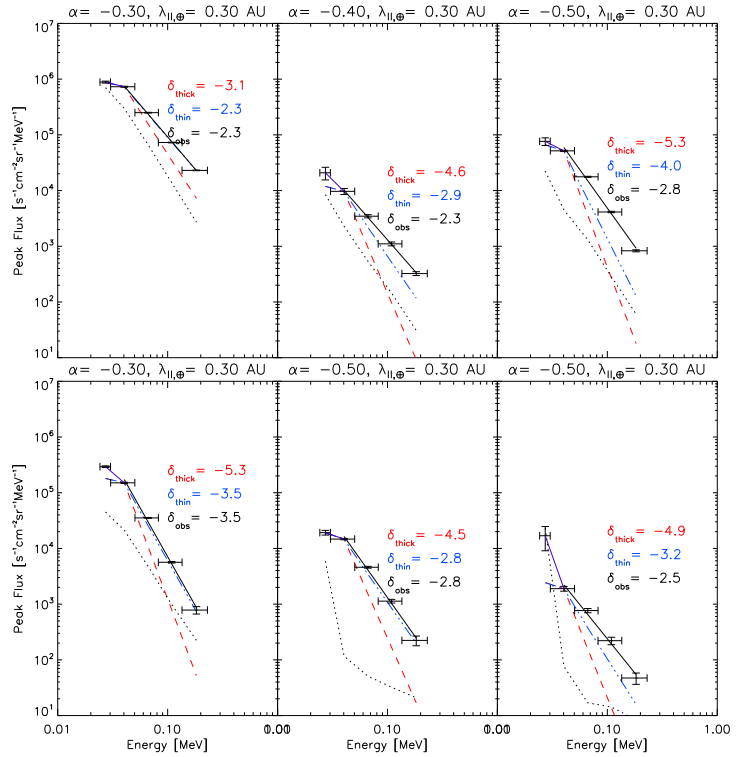


Figure 2.13: An overview

of background subtracted peak-flux electron spectra for impulsive (**top**) and gradual events (**right**), showing the Wind/ $3DP$ spectra (black points with black fit) vs simulation spectra (thick and thin target are red and blue), using RHESSI inferred values as input. The black dashed line shows the pre-event background measured by Wind.



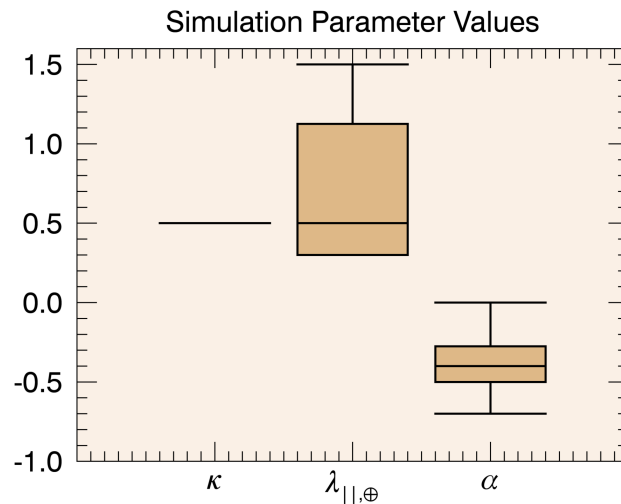


Figure 2.14: A box plot showing the parameter distribution which the analysed events fall into.

2.5.3 Average Scattering Properties

While the simulation parameters used to best match observations varied by event, an attempt to find a statistical dependence of scattering upon electron momentum and heliocentric distance was made (Figure 2.14). For all events, a clear dependence upon heliocentric distance was found, given by $\lambda_{\parallel} \propto z^{0.5 \pm 0.25}$, implying that the amplitude of parallel magnetic fluctuations drops with heliocentric distance, either via conversion to perpendicular fluctuations, or simply through a reduction in fluctuation level. Here the uncertainties arise from the parameter spacing used. While all events were found to fit better with $\kappa = 0.5$, the low resolution in parameter space tested and the small numbers of κ values used limit the precision of results.

It was also found that most events analysed fell within a relatively small range of α , giving an empirical relation of $\lambda_{\parallel} \propto p^{-0.8 \pm 0.4}$. This suggests that the highest energy electrons experience extremely strong resonant interactions with magnetic fluctuations, while lower energy electrons do not. Future measurements of the magnetic fluctuation spectrum at the electron scale are required to test this.

Finally, we consider the normalising constant $\lambda_{\parallel,\oplus}$. Here, however, the results are spread more evenly over the parameter space. This leads us to remark that, due to the

variability of magnetic field parameters (and hence strength of scattering) at Earth, no general relation between the strength of the scattering during transport and at Earth can be found.

2.6 Summary

In this work, we have simulated the propagation of 27 – 180 keV electrons travelling along a turbulent magnetic field away from the Sun. We have used both RHESSI X-ray and Wind/*WAVES* radio observations of the Sun to initialise our simulations, taking the relative timing of the X-ray and radio emission as the electron injection time at the Sun, and using the HXR spectral information to estimate the injected electron population’s energy spectrum. We have analysed 14 events using the *3DP Solid State Telescope* aboard the Wind spacecraft to determine the timing and spectral properties of electrons at 1 AU, and have compared our simulations to observations.

Using these comparisons, an average dependency for mean-free path upon heliocentric distance and electron momentum was found, given by

$$\lambda_{\parallel}(r, p) = \lambda_{\parallel, \oplus} \left(\frac{r}{r_{\oplus}} \right)^{0.5 \pm 0.25} \left(\frac{p}{p_0} \right)^{-0.8 \pm 0.2}, \quad (2.18)$$

where the indices represent the mean parameters found in each comparison, and the uncertainties are found through the parameter bin widths.

We find that these results agree with results drawn from previous studies. [Agueda et al. \(2014\)](#) studied 7 electron events of similar energy ranges observed by *Wind* and *ACE*, and ran similar models to fit the observed intensities at 1 AU. In this work, a mean rigidity-mean free path relationship of $\lambda_{\parallel} \propto R^{-0.7}$ was found¹, similar to our range. Similar to our findings, [Agueda et al. \(2014\)](#) see a fairly even spread in scattering strengths used in simulations.

Previous models of proton transport from a flare to 1 AU ([Beeck et al., 1987](#)), and between 1-6 AU ([Hamilton, 1977](#)) have given distance relations of $\lambda_{\parallel} \propto r^{0.6 \pm 0.1}$

¹Here $R = p/e$ is particle rigidity, and e is particle charge.

and $\lambda_{\parallel} \propto r^{0.4 \pm 0.2}$ respectively. While the populations analysed here are different, we find that our obtained result is comparable to these findings, under the assumption that scattering dominates over any adiabatic focussing. However, the limited range of values used here for κ ($\kappa = 0, 0.5, 1$) reduce reliability of any conclusions, and a more thorough search of the parameter space must be performed to more precisely determine the mean-free path dependence upon distance.

Comparisons between the spectra of electrons at the Sun and at 1 AU (e.g. by [Lin, 1985](#); [Krucker et al., 2007](#)) have showed that the spectrum of electrons at 1 AU is, in general, flatter than the inferred solar electron spectrum ($\delta_{\oplus} \approx \delta_{\odot} - 1$). Our simulations demonstrate that this difference can be explained by transport effects. The distance-dependant form of the mean-free path used has allowed us to place electrons observed near Earth in the same population as HXR producing electrons at the Sun. Our 1D simulations have succesfully reproduced the large-scale features of near-Earth observations, matching the large-scale time-profiles and anisotropies, apparent delay, and the peak spectra of energetic electrons.

It is important to note that this is the first time that direct X-ray emission models have been used to initialise simulations of this kind, allowing a comparison of the in-situ electron population with the inferred solar electron population. The agreement between simulated and observed electron distributions near Earth has backed up the hypothesis that upwards and downwards travelling electron beams are injected simultaneously in a solar flare, and the state of fluctuations along the interplanetary magnetic field have been probed.

As the generation of Langmuir waves affect the lowest energies simulated here, the addition of Langmuir wave generation/ absorption into simulations would greatly assist the analysis of lower energy electron transport from the flare site to Earth. This would allow for a full comparison between observations and simulations over all energy ranges covered by in-situ detectors, such as Wind/ ACE.

Chapter 3

Studying the Time Evolution of a Low-Frequency Type-IIIb Radio Source

The main focus of this chapter is a summary of the results of [Kontar et al. \(2017\)](#), which are key for the simulation work presented in [Chapter 4](#).

3.1 A Typical Type-III Burst

An overview of type-III burst features is given in [§1.4.3](#), however a “typical” type-III burst will be described again here, and the methods of analysing it shall be highlighted.

3.1.1 Typical Burst Features

As flare-accelerated electron beams pass through the coronal and interplanetary plasma, they generate Langmuir waves. These break down primarily by interactions with ion-sound waves or coalescence with oppositely propagating Langmuir waves, producing the fundamental and harmonic components of type-III bursts ([Melrose, 1980b](#); [Suzuki & Dulk, 1985](#)). As the beam travels into regions of progressively lower density, the frequency of induced Langmuir waves decreases and, hence, the frequency of emitted

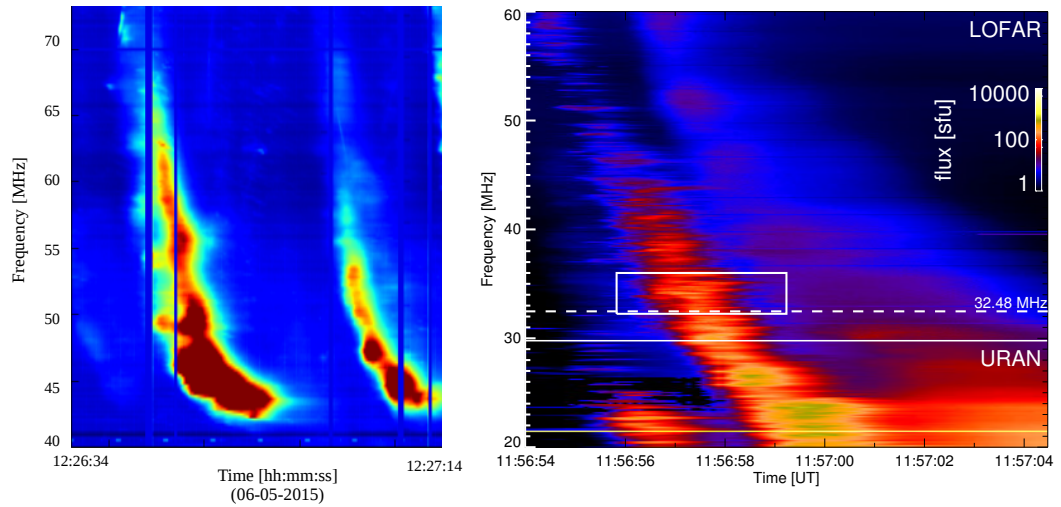


Figure 3.1: Example type-III and type-IIIb radio bursts. **(left)** Two “typical” type-III radio bursts observed during the 2015-05-06 event, adapted from Reid & Kontar (2017). The dynamic spectrum was taken by LOFAR. **(right)** A type-IIIb – type-III pair observed during the 2015-04-16 event (from Kontar et al., 2017), taken with combined LOFAR and URAN observations. The horizontal dashed line shows a single frequency for which the radio source was imaged, the solid line denotes the LOFAR (above) and URAN (below) observations, and the box shows the area for which multiple striae were imaged.

radiowaves drops. The frequency drift rate of observed type-III bursts can be inverted, in order to determine the propagation speed of the exciter electron beam.

Typical type-III bursts feature fast drifts from high to low frequencies, with a generally smooth dynamic spectrum (Reid & Ratcliffe, 2014). An example of this is seen in Figure 3.1 (left), where the characteristic l-shape is clear. Generally, type-III bursts feature increased peak flux with decreasing frequency (e.g. Saint-Hilaire et al., 2013). A maximum is usually found at around 1 MHz (Smith & Davis, 1975), below which the peak flux tends to decrease with frequency (Dulk et al., 1998). This relationship is strongly dependent upon the stopping distance of radio bursts, and bursts which are limited to the corona feature the most intense emission at the lowest frequencies reached.

The duration of a typical type-III burst tends to increase with decreasing frequency, with rise and decay times both roughly inversely proportional to burst frequency [Benz et al. \(1983\)](#). Finally, the typical type-III burst features very low levels of circular polarisation. Measured values of circular polarisation in type-III bursts have found an average of $\sim 15\text{--}30\%$ in fundamental bursts ([Dulk & Suzuki, 1980](#); [Suzuki & Dulk, 1985](#)), although polarisations up to 50% have been found ([Dulk et al., 1998](#)). The circular polarisation of the H-component in bursts is usually lower than that for the F-component, and has mean values around $5 - 10\%$ (e.g. [Dulk & Suzuki, 1980](#)).

3.1.2 Typical Electron Properties

Simultaneous in-situ detections of electron beams (featuring a *bump-on-tail* distribution) and Langmuir waves by near-Earth spacecraft (e.g. [Lin et al., 1981](#); [Dulk et al., 1998](#)) have helped confirm the plasma emission mechanism. However, this emission process is non-linear, and hence determination of electron properties from observed type-III properties is a complex process.

Comparison of measured electron beams and their associated radio emission was performed by [Dulk et al. \(1998\)](#), who found little correlation between electron and radio flux densities over 10 events, although a correlation between the ratio of the flux densities compared with electron energies was found. Analysis of these events showed that the positive slope in velocity space tended to occur at electron energies around $E \approx 5 - 15$ keV, in agreement with $1 - 15$ keV estimates by [Ergun et al. \(1998\)](#). This work demonstrates that the typical maximum energy of Langmuir generating electrons is around 15 keV, similar to numerical estimates from [Kontar & Reid \(2009\)](#).

Indirect determination of electron parameters requires either assumptions on electron/ wave transport, or complex simulation work. As mentioned in the §1.4.3, the frequency drift rate of observed bursts can be inverted to determine the source beam speed, assuming that the beam propagates radially, and both the beam and produced emission experience no scattering. This method gives a mean electron beam speed as $\sim 0.15 - 0.3 c$ ([Dulk et al., 1987](#); [Melnik et al., 2011](#)). Similarly, the burst width

(duration) can be assumed to be the time during which the source electron beam is at the correct distance to produce emission at the observed frequency. Using an inferred beam speed, the vertical size of the beam can be calculated. As the burst duration has been found to be $T = 60f^{-2/3}$ between 0.3 – 500 MHz (Elgaroy & Lyngstad, 1972), giving beam lengths of e.g. $\sim 0.9R_{\odot}$ at 30 MHz.

While the derivation of observationally inferred electron parameters require strong assumptions, comparisons of numerical work with observations allows for a much greater range of scenarios to be explored. State-of-the-art simulations modelling the entire plasma emission process have produced large variations in radio dynamic spectra by including changes in coronal electron and ion temperatures (Li et al., 2011b,a), or small fluctuations in the background plasma density (Loi et al., 2014), for example. By comparing simulated and observed dynamic spectra, constraints can be put on the properties of electron beams which are not directly measured.

3.2 Type-IIIb Background

Observations of <200 MHz type-III sources has been performed regularly since the late 1960s by ground-based imagers (see §1.4.3) and spectrometers. Under the assumption of an unchanging background density profile, it would be expected that an imaged radio source would correspond directly to the radio-producing source electron population, and a direct correlation with spectral properties (e.g. frequency drift rate and imaged source velocity) should arise.

Type-III bursts often feature small narrow-band intensity fluctuations, resulting in a “bumpy” dynamic spectrum (e.g. de La Noe & Boischot, 1972; Benz et al., 1982; Mel’Nik et al., 2005). These events are known as type-IIIb bursts (de La Noe & Boischot, 1972), and feature chains of near-zero drift rate bursts (called *striae*) which, when observed over a frequency range much larger than the burst width, have similar drift rates to “normal” type-III bursts. While these bursts feature smooth electron profiles, direct measurements of the Langmuir wave population have revealed much clumpier distributions than the corresponding electron profiles (Chaizy et al., 1995;

Thejappa et al., 2012).

Simulations by Kontar (2001b) have shown that extremely small density fluctuations ($\delta n_e/n_e \sim 0.2\%$) present in the heliosphere are able to generate large variations in Langmuir wave energy, producing the clumpy distribution observed in-situ. In turn, simulations of electron transport and Langmuir wave generation (e.g. Kontar, 2001b; Li et al., 2012; Loi et al., 2014) have led to the common conclusion that these clumpy Langmuir wave distributions results in the narrow-band radio emission features observed in type-IIIb bursts. Observations of type-IIIb bursts have been used to estimate the density fluctuation level close to the Sun, inferring fluctuation levels of $\delta n_e/n_e = 0.6 \pm 0.2\%$ between 1.6-2.2 R_\odot (Mugundhan et al., 2017).

While type-IIIb bursts can be used to study the background medium through which an electron beam passes, they are also a useful diagnostic of the beam itself. The frequency drift rate can give an estimate of the propagating beam velocity (see Chapter 5), and hence the FWHM burst duration gives an indication of the source size. Similarly, the stria frequency width is dependent upon the sizes of the propagating electron beam and density inhomogeneity (Kontar et al., 2017), giving a lower bound on the radio source size under various density models. By using this information, the inferred source size can be directly compared to imaged source sizes.

While density fluctuations on this order are too small to greatly affect the propagation of the source electron beam, simulations have shown that fluctuations on this scale can affect the propagation of radio waves (Steinberg et al., 1971; Arzner & Magun, 1999; Thejappa et al., 2007; Li et al., 2008). Scattering of radio waves off small density inhomogeneities does not affect the scattered wave frequency (and hence the striae band-width should remain unchanged after scattering), but the arrival time and incidence angle of incoming waves at 1 AU should change, affecting the burst duration and any produced images.

Using extremely high time resolution, spatial resolution, and frequency resolution images from the LOw Frequency ARray (LOFAR; van Haarlem et al., 2013), Kontar et al. (2017) compared inferred and imaged source properties to each other, in order to determine the effects of heliospheric turbulence on radio images.

3.3 LOFAR Overview

The LOFAR radio telescope is a series of low frequency antennas positioned across multiple countries (though centred in the Netherlands), designed primarily for astrophysical observations. However, LOFAR’s ability to take images across a range of frequencies (as opposed to radioheliographs) has made it particularly attractive for application to solar observations, in particular looking at Type-III solar radio bursts (e.g. [Morosan et al., 2014](#); [Reid & Kontar, 2017](#); [Kontar et al., 2017](#)).

LOFAR consists of two types of antenna: High-Band and Low-Band Antennas (HBAs & LBAs), which operate at frequencies of 110–240 MHz and 110–240 MHz respectively, although it is noted that typically the LBA range is kept within 30–80 MHz due to RFI and FM signal interference ([van Haarlem et al., 2013](#)). As opposed to traditional radio imaging, where interferometric visibilities are produced, LOFAR can take images via its *beam-formed mode* ([Stappers et al., 2011](#); [van Haarlem et al., 2013](#)). In this mode, LOFAR’s different collection stations are split into “array beams” which are each pointed at a different region of the sky. The coherent combination of multiple stations then produces an image over the desired range ([Morosan et al., 2014](#)). In this mode, LOFAR operates with centisecond time resolution, frequency resolution of ~ 12 kHz, and variable spatial resolution.

The beam FWHM depends upon the beam shape in the sky and the frequency of observations, with around ~ 9 arcminute resolution at 30 MHz ([Reid & Kontar, 2017](#)). While the spatial resolution is still fairly low for single beam observations, by using all of LOFAR’s beams (e.g. 169 beams used in [Reid & Kontar, 2017](#)), the uncertainty on source position and size can be reduced, particularly for strong bursts which occur from extended sources ([Condon, 1997](#); [Kontar et al., 2017](#)).

3.4 16th of April 2015 Event

On the 16th of April 2015, radio emission was observed by LOFAR’s LBA and the Ukrainian Radio interferometer of the National Academy of Sciences (URAN-2) si-

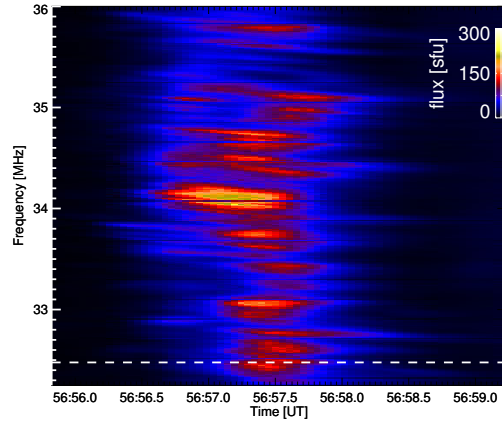


Figure 3.2: Dynamic spectrum from the 2015-04-16 event (from [Kontar et al., 2017](#)). A chain of near-zero frequency drift bursts can clearly be seen between 36 and 32 MHz, and the horizontal line shows a specific stria for which analysis is presented.

multaneously, giving an overlapping frequency range useful for calibrating LOFAR observations. This event was studied in [Kontar et al. \(2017\)](#), and featured a pair of type-III bursts: a type-IIIb burst (Figure 3.1, right) followed shortly by a “normal” type-III burst (called a type-IIIb – type-III pair). The timings and polarisation of the two bursts led to the conclusion that they were the fundamental and harmonic components of the type-IIIb.

Analysis of the dynamic spectrum revealed a beam speed of $\sim c/3$, a FWHM duration of ~ 1 second, and a fundamental source area of $A \sim 10^{-2}$ arcmin² (inferred from the striae frequency widths). However, while small sources were predicted from the dynamic spectrum, when imaged the burst appeared as an extremely extended source, of fundamental area $A \sim 400$ arcmin². For 48 stria between 32–38 MHz (Figure 3.2), the burst area and centroid position were tracked through time. This was achieved by fitting an elliptical Gaussian to observed sources, allowing for high precision on measured source centroid and area.

For a single frequency (32.48 MHz; Figure 3.3), a variation in source size and position was observed. During the burst decay phase (i.e. burst peak – half-max), linear fits were applied to source area and heliocentric distance. The burst decayed extremely rapidly (fundamental decay time ~ 0.6 seconds), during which time the

centroid moved with an average radial speed of $\sim c/4$, and grew with an average expansion rate of $\sim 180 \text{ arcmin}^2 \text{ s}^{-1}$. The final source area (of fundamental frequency) of $\sim 530 \text{ arcmin}^2$ was significantly larger than the predicted area from the dynamic spectrum, and interestingly, the fundamental source was observed to move radially *away* from the disk centre. Both features are in contradiction to expectations based purely from regular refraction.

The 32.48 MHz harmonic source was more extended in both space and time; with a decay time of $\sim 3\text{s}$, and a final area of $\sim 760 \text{ arcmin}^2$. However, both the harmonic expansion rate and centroid shift speed were much lower than those of the fundamental source; with around $50 \text{ arcmin}^2 \text{ s}^{-1}$ growth rate and negligible centroid movement speed. The fundamental and harmonic sources also differed in their apparent positions; with the fundamental source appearing further from the disk centre and moving radially North-West away from the centre, while the harmonic source appeared much closer to the disk centre and moved orthogonal (\sim east) to the centre.

By studying the group of all striae, [Kontar et al. \(2017\)](#) found that this trend was repeated; fundamental sources appeared further from the disk centre than their harmonic counterparts, and appeared to move radially away from the centre. The average position of each burst moved generally south-west in both fundamental and harmonic case, although the two emission modes followed different (but parallel) paths.

[Kontar et al. \(2017\)](#) concluded that the imaged source properties (position, area, growth rate, velocity) were strongly influenced by heliospheric density fluctuations. Strong evidence towards this hypothesis was provided by the observation of extended sources, in contradiction to the small inferred sources; the difference in fundamental and harmonic growth rates and positions; and the rapid growth of the sources. Models based purely off regular refraction or upon the assumption that these are intrinsic source properties are unable to explain these observations. The authors suggested that the large imaged source size compared to the small burst duration pointed towards an anisotropic scattering profile (preferential scattering perpendicular to the solar surface) or scattering off multiple fibre-like features in the heliosphere.

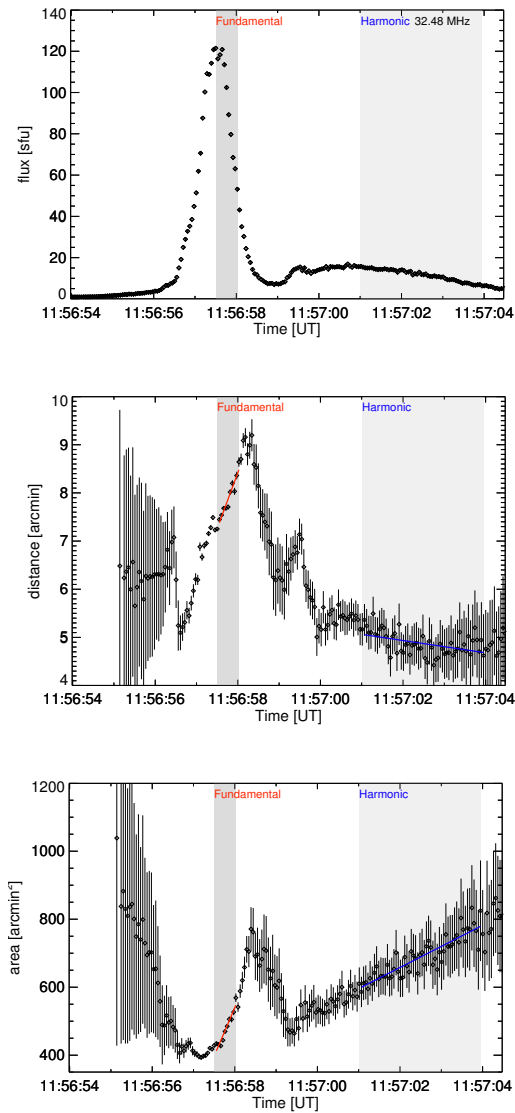


Figure 3.3: (**top–bottom**) Measured flux, source distance from the solar disk centre, and source area. Linear fits to fundamental (red) and harmonic (blue) distance and area are shown, and the grey areas demarcate the decay phase of the burst (peak to half-max). From [Kontar et al. \(2017\)](#)

3.5 Testing the Effects of Scattering

The results of [Kontar et al. \(2017\)](#) provide strong evidence towards the hypothesis that imaged low-frequency radio source properties are determined primarily by the interplanetary density structures. However, the extent to which density fluctuations

affect the imaged properties remains to be seen, and testing is required to see whether observed features from the 16-04-2015 event can be replicated in simulations.

Simulations of radiowave scattering via density turbulence have shown that scattering and refraction of radiowaves during propagation affects the properties of any images sources. [Steinberg et al. \(1971\)](#) showed that scattering serves to increase the apparent size of sources, with the greatest effects occurring for sources closer to the solar limb. In this case, the source centroid position appears to drift closer to the disk centre, due to the appearance of a weak tail in the brightness distribution. Conversely, simulations by [Riddle \(1972\)](#) showed a general shift *away* from the disk centre, although no time dependant motion of the source was investigated.

Using separate methods, [Arzner & Magun \(1999\)](#) found apparent increases in source size due to scattering. However, when tracking the position of the source through time, only *inwards* radial motion was observed. Hence, further study is required to see whether radio transport simulations can replicate observed *outwards* movement of an apparent radio source.

The subject of Chapter 4 revolves around testing this idea, asking the question of whether isotropic scattering and simple density models can produce features similar to those observed. The focus is put on simulating the fundamental source, as this is where the most drastic departures from simpler theories arise (e.g. rapid growth, outwards radial motion), and images comparable to those used by [Kontar et al. \(2017\)](#) are produced.

Chapter 4

Ray Tracing Simulations of Solar Radio Bursts in the Corona

4.1 Background

As discussed in the introductory chapter, type-III radio bursts are an excellent diagnostic tool with which the properties of both flare accelerated electrons, and the ambient solar background can be probed. Calculating the electron source properties (e.g. position, size, velocity) is of interest for enabling comparison with the post-flare population with the population inferred through e.g. X-ray and EUV observations. Type-III bursts also give an understanding of the conditions of propagation throughout space, giving information on both the source beam and the background plasma.

Type-III radio bursts are generated near the plasma frequency (for fundamental emission) or $\sim 2\times$ the plasma frequency (for second harmonic emission) (Suzuki & Dulk, 1985; Melrose, 2017), and so the burst is refracted into a small cone, directed radially away from the source-Sun line. While this form is well understood, low frequency events have been observed simultaneously across wide viewing angles through the use of the *STEREO*, *Wind*, and *ACE* spacecraft (Reiner et al., 2009; Martínez-Oliveros et al., 2015). Under the assumption of a symmetrically decreasing background plasma density profile, some process must be scattering the waves out of the refraction cone,

allowing for large angle observations.

Using the high resolution Low-Frequency Array (LOFAR) radio telescope, the sub-second variation of a type-III radio source, observed on the 16th of April 2015, has been studied by [Kontar et al. \(2017\)](#) (Chapter 3). In the 16-04-2015 event, well resolved striae were observed at multiple frequencies between 32–36 MHz (Figure 3.2), implying a compact radio source. However, by imaging the emission within narrow frequency ranges, a large source was observed, whose centroid position and area both varied in time. By comparing the narrow-band dynamic spectrum features with the large observed sources, it was concluded that scattering and refraction (*propagation effects*) of emitted radio waves were responsible for the observed variations in both position and size of the source.

The statistical method for modelling the transport of rays through a medium with fluctuating density profile was originally formulated by [Chandrasekhar \(1952\)](#), aimed at explaining stellar scintillation and atmospheric seeing. This was adapted by [Fokker \(1965\)](#); [Hollweg \(1968\)](#); [Steinberg et al. \(1971\)](#), who applied Chandrasekhar’s method to transport through the solar corona. More recently, [Arzner & Magun \(1999\)](#); [Thejappa et al. \(2007\)](#) have further modified this work, modelling higher frequency (100 MHz - 250 MHz) and lower frequency (120 kHz) bursts, respectively. While the mathematical framework for ray tracing simulations of this scale has been set out for a long time, there has only been limited work in utilising simulations to predict variations in the source size and source position during the burst.

In this work, we use methods derived by the above authors to build a 3D Monte-Carlo simulation of ray transport from a point source to an observer a distance away, accounting for both large-scale background density gradients and micro-scale density fluctuations, in order to observe any apparent variation in the source size and position. Section 4.2 introduces the model used to transport the rays and the method to account for scattering and absorption of the rays during transport. Section 4.3 discusses the imaging scheme used and presents the results obtained, while in Section 4.4 we draw conclusions from these results and discuss future methods of validation of results.

4.2 Ray Tracing Scheme

The transport of low frequency (≤ 120 MHz) radio waves through the corona and heliosphere is strongly dependent upon the characteristics of the background material, through which the waves pass. As radio waves pass through an increasingly sparse corona, variations in coronal density cause the wave path to be altered, refracting and scattering the radiation.

In this work, we consider the three dimensional propagation of waves outwards from a coronal source, and study the effects that large-scale density gradients and turbulent density fluctuations have upon the waves' direction of travel. For simplicity, the radio burst is modelled as a collection of rays of angular frequency ω , each occupying a position $\mathbf{r} = (r_x, r_y, r_z)$, and wavenumber $\mathbf{k} = (k_x, k_y, k_z)$. The propagation of each ray is determined by the canonical Hamiltonian equations (e.g. [Witham, 1974](#); [Arzner & Magun, 1999](#))

$$\frac{d\mathbf{r}}{dt} = \nabla_{\mathbf{k}}\omega, \quad (4.1)$$

$$\frac{d\mathbf{k}}{dt} = -\nabla\omega. \quad (4.2)$$

The dispersion relation for photons travelling in an un-magnetised plasma is

$$\omega(r, k) = \sqrt{\omega_{pe}(r)^2 + c^2k^2}, \quad (4.3)$$

where c is the speed of light, k is the absolute magnitude of \mathbf{k} , and $\omega_{pe}(r) = 2\pi f_{pe}$ is the angular plasma frequency. The fundamental electron plasma frequency, f_{pe} , is determined by the expression

$$f_{pe}(r)[\text{kHz}] = \sqrt{\frac{e^2 n_e(r)}{\pi m_e}}, \quad (4.4)$$

where $n_e(r)$ is the background electron plasma density [cm^{-3}], which is dependent upon distance from the Sun (see §4.2.3).

Type-III radio bursts are emitted very close to the plasma frequency ([Reid & Ratcliffe, 2014](#)). Assuming the three-wave model of fundamental emission, where the

radio-wave is produced via coalescence of a Langmuir wave and ion-sound wave, the photon frequency is given by $\omega = \omega_{pe} + \omega_s$. In this work, we assume that the frequency of ion-sound waves is $\sim 3\%$ that of Langmuir waves, and hence assumed that all photons are emitted with a frequency of $f = 1.03f_{pe}$.

The cyclotron frequency of waves travelling in a magnetic field is given by $\Omega_{ce}[\text{MHz}] \approx 2.8B(r)[\text{G}]$ (Aschwanden, 2005). Using a coronal magnetic field model to obtain typical magnetic field strength at $\sim 1.7 R_\odot$ (e.g. see §1.5.1), it can be seen that the plasma frequency is far higher than the cyclotron frequency. Because of this, we ignore any magnetic field in simulations; assuming that all rays travel through an un-magnetised plasma. The refractive index of rays travelling in an un-magnetised plasma (ρ) is simply given by (§1.6.2)

$$\rho^2 = 1 - \left(\frac{f_{pe}}{f}\right)^2. \quad (4.5)$$

4.2.1 Numerical Scheme

To solve the equations $d\mathbf{r}/dt = g(t, \mathbf{k})$ and $d\mathbf{k}/dt = m(t, \mathbf{r})$ with the initial conditions $\mathbf{r}(t_0) = \mathbf{r}_0$ and $\mathbf{k}(t_0) = \mathbf{k}_0$, a fourth order Runge-Kutta scheme is used (Press et al., 1986). Here, the functions $g(\dots)$ and $m(\dots)$ represent the right hand sides of Equations (4.1 & 4.2). The value of t , $y = \mathbf{r}, \mathbf{k}$, and $x = \mathbf{k}, \mathbf{r}$ are recursively updated via

$$t_{n+1} = t_n + \Delta t, \quad (4.6)$$

$$y_{n+1} = y_n + \frac{\Delta t}{6}(h_1 + 2h_2 + 2h_3 + h_4), \quad (4.7)$$

where

$$h_1 = f(t_n, x_n), \quad (4.8)$$

$$h_2 = f\left(t_n + \frac{\Delta t}{2}, x_n + \frac{h_1 \Delta t}{2}\right), \quad (4.9)$$

$$h_3 = f\left(t_n + \frac{\Delta t}{2}, x_n + \frac{h_2 \Delta t}{2}\right), \quad (4.10)$$

$$h_4 = f(t_n + \Delta t, x_n + h_3 \Delta t). \quad (4.11)$$

Using this scheme, the rays can be traced through any medium, provided the initial photon characteristics (i.e. position \mathbf{r}_0 and wavenumber \mathbf{k}_0) and background density profiles are known.

4.2.2 Initial Source Parameters

In all simulation runs, a single source placed at a radial distance of $\sim 1.76 R_\odot$ was considered, corresponding to a fundamental frequency of ~ 32 MHz. Three different source shapes were initially considered (a spherical source, a disk source viewed from the radial direction¹ and a point source), however due to relatively low resolution when reconstructing images it was found that the initial source shape had little outcome on the reconstructed source shape. Hence, the source shape was limited to a point for all further simulation runs.

Both isotropic and dipole emission profiles were modelled (Figure 4.1), in order to observe the differences in resultant images. The isotropic distribution was given by

$$\theta_0 = \arccos(2\xi - 1), \quad (4.12)$$

$$\phi_0 = 2\pi\xi, \quad (4.13)$$

where $\xi \in \mathcal{U}[0, 1]$ denotes a pseudo-random variable drawn from a uniformly distributed pool between 0 and 1, and θ & ϕ are polar and azimuthal direction angles, respectively. For polar emission, the fundamental emission was given by a dipole pattern,

$$f_F(\theta_0) = \sin^2(\theta_0), \quad (4.14)$$

$$\phi_0 = 2\pi\xi, \quad (4.15)$$

where the dipole axis is directed along the z-axis.

Using the initial ray angular distribution, the ray direction cosines ($T_{x,0}, T_{y,0}, T_{z,0}$) were obtained as (Thejappa et al., 2007; Jeffrey & Kontar, 2011)

¹Both spherical and disk sources had radii ~ 1.5 Mm.

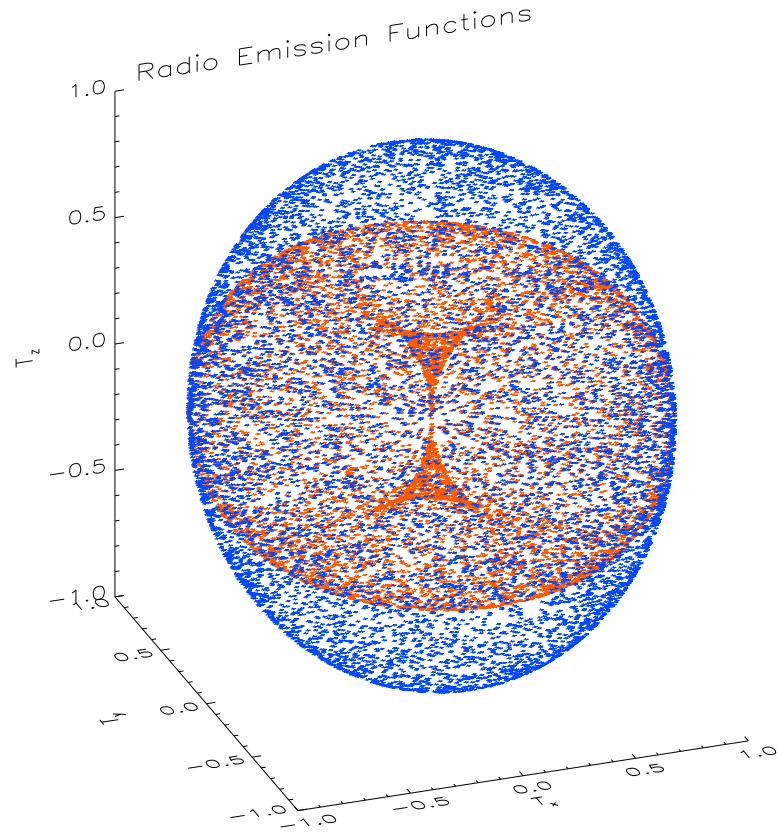


Figure 4.1: 3D scatter plot of radiation emission patterns used in simulations. Blue shows isotropic emission and red shows dipole (fundamental) emission with the dipole axis directed along the z-axis.

$$T_{x,0} = \sin(\theta_0) \cos(\phi_0), \quad (4.16)$$

$$T_{y,0} = \sin(\theta_0) \sin(\phi_0), \quad (4.17)$$

$$T_{z,0} = \cos(\theta_0). \quad (4.18)$$

The absolute value of the initial ray wavenumber \mathbf{k}_0 was determined from the initial position \mathbf{r}_0 and frequency through the rearrangement of Equation 4.3, and the initial wavenumber components were given by $(k_{x,0}, k_{y,0}, k_{z,0}) = \|\mathbf{k}_0\|(T_{x,0}, T_{y,0}, T_{z,0})$.

4.2.3 Background Density Model

The background plasma was modelled as in [Kontar \(2001a\)](#); [Reid & Kontar \(2013\)](#), using a heliospheric density model derived by [Parker \(1958\)](#). In this model, the corona is assumed to be isothermally expanding, leading to the equations

$$\left(\frac{v(r)}{v_c}\right)^2 - 2 \ln\left(\frac{v(r)}{v_c}\right) = 4 \ln\left(\frac{r}{r_c}\right) + 4 \ln\left(\frac{r_c}{r}\right) - 3, \quad (4.19)$$

$$n_{e,0}(r) = \frac{6.3 \times 10^{34} [\text{s}^{-1}]}{r^2 v(r)}. \quad (4.20)$$

By numerically integrating these equations, the electron density from the corona outwards can be calculated. Here, r is the radial distance from the Sun's centre, $v(r)$ is the plasma velocity at a distance r , and $n_{e,0}(r)$ is the background electron density at the distance r . The critical velocity is given by $v_c = \sqrt{k_b T_e / \tilde{\mu} m_p} = v(r_c)$, the critical distance by $r_c = GM_\odot / 2v_c^2$, M_\odot is the mass of the Sun, m_p the proton mass, $\tilde{\mu}$ the mean molecular weight (0.6 in the solar wind [Kontar, 2001a](#)), T_e is the electron plasma temperature, and the constant in Equation (4.20) is found by using the background density $n_e(1 \text{ AU}) = 6.59 \text{ cm}^{-3}$ ([Mann et al., 1999](#)).

As an analytical density profile is required to solve Equations (4.1) and (4.2), an analytical approximation of the electron density profile solution to Equations (4.19) and (4.20) was used to model the plasma density, given by

$$n_{e,0}(r) = \frac{m_1}{r^{2.3}} + \frac{m_2}{r^6} + \frac{m_3}{r^{14}}, \quad (4.21)$$

where m_1 , m_2 , and m_3 are given by $m_1 = 1.39 \times 10^6 [\text{R}_\odot^{2.3} \text{ cm}^{-3}]$, $m_2 = 3 \times 10^8 [\text{R}_\odot^6 \text{ cm}^{-3}]$, and $m_3 = 4.8 \times 10^9 [\text{R}_\odot^{14} \text{ cm}^{-3}]$. In this model, the coronal plasma temperature is taken to be $T = 1 \text{ MK}$, and is taken to be constant throughout the modelled area. As most of the scattering occurs within a small volume close to the source (Figure 4.4), this is found to be a reasonable assumption. Figure 4.2 shows the comparison of this approximation to the solution to Parker's model. Also shown for comparison is an empirical density model derived by [Leblanc et al. \(1998\)](#).

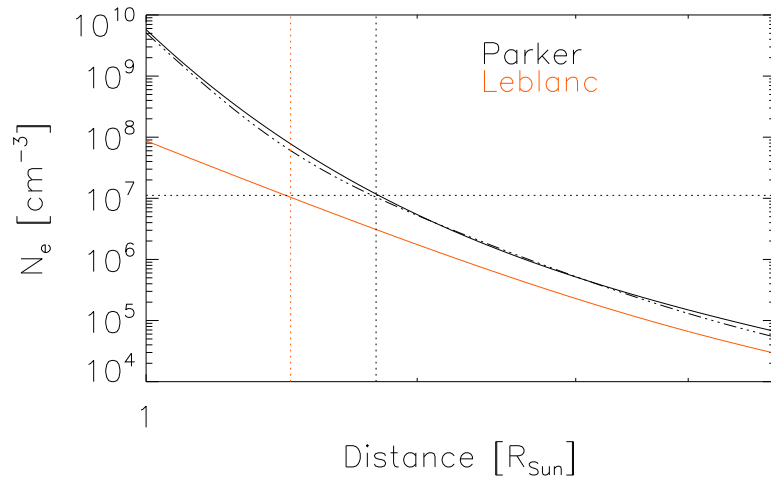


Figure 4.2: Comparison of Parker’s (black) and Leblanc’s (orange) background electron density profiles. Solid black shows Parker’s numerical model, while dot-dashed black shows the analytical approximation. The horizontal dotted line shows the density at which 32 MHz waves are emitted, and the vertical coloured dotted lines show the positions at which this density is reached, according to each model.

4.2.4 Asymmetric Density Models

While the assumption of an isotropic background density profile centred at the Sun allows for simple calculations of ray trajectories throughout space, observationally it is clear that the coronal density is much more complicated, featuring higher and lower density regions (see e.g. [Koutchmy & Livshits, 1992](#), for a review).

Methods to study the effects of over- and underdense regions in the corona (e.g. streamers and coronal holes) have been used by [Hoang & Steinberg \(1977\)](#); [Bougeret & Steinberg \(1977\)](#); [Thejappa & Kundu \(1994\)](#). However, while the effects on computed brightness temperatures from the large-scale density displacements has been studied, no time-dependent variation in apparent source position and size has been considered.

To model coronal streamers and holes, we consider two further background density cases; a high density (streamer) case, and a low density (coronal hole) case. In each model, we superimpose an additional asymmetric density profile onto the symmetric background profile, and model both the over-density and under-density via a

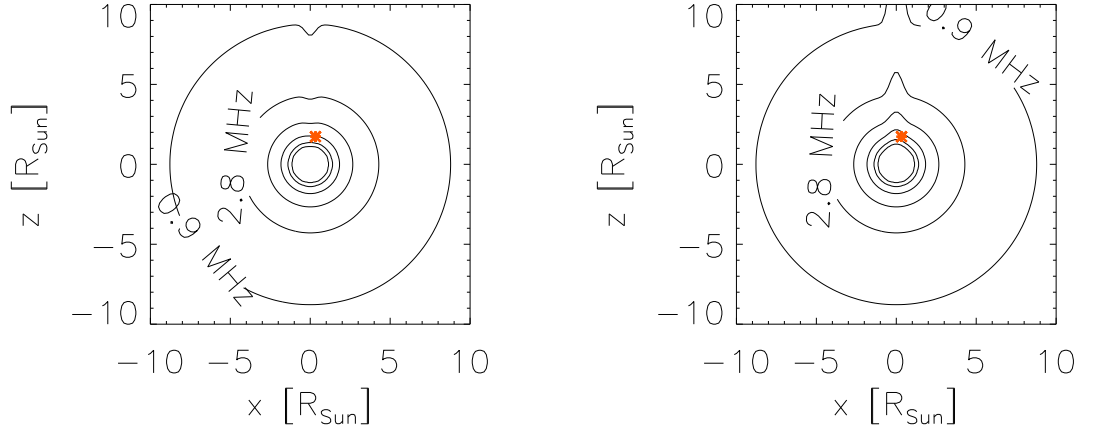


Figure 4.3: **(left)** Symmetric background + underdense asymmetric electron density profile, showing contours of constant plasma frequency. **(right)** Symmetric background + overdense asymmetric electron density profile. The red star shows the emission location of rays in simulations.

2D Gaussian,

$$n_{e,s}(x, y, z) = \pm N \times n_{e,0} e^{-\frac{r_x^2}{2\sigma_x^2} - \frac{r_y^2}{2\sigma_y^2}}. \quad (4.22)$$

In this case, (σ_x, σ_y) determines the width of the profile, and N determines the population of the profile. Here, the sign of the profile is switched to account for overdensities and underdensities. Using both the isotropic background profile and the asymmetric density profile, the final density profile was given as

$$n_e = n_{e,0} + n_{e,s}, \quad (4.23)$$

as shown in Figure 4.3. In simulations, the asymmetry width was set as $\sigma_x \in [0.33, 0.5] R_\odot$, $\sigma_y = \sigma_x$, and N was set as +2 and -0.2 for over- and under-dense models, respectively; consistent with observations (see §1.5.2 for quoted values). The ray source was placed at the edge of the over/under-density, at $(x, y) = (\sigma_x, \sigma_y)$. The source z -position was chosen to ensure that the frequency remained at $f = 32$ MHz.

4.2.5 Density Fluctuation Model

The background density fluctuations were added following [Thejappa et al. \(2007\)](#). The fluctuations are assumed to follow a power spectrum

$$P_n(q) = C_N^2 q^{-11/3}, \quad (4.24)$$

within the inertial range $q_o < q < q_i$, where q is the spatial wavenumber, $11/3$ is the Kolmogorov spectral index in 3D, and C_N^2 is a normalising constant. The inner- and outer-scale lengths of fluctuations are given by $l_i = 2\pi q_i$ and $l_o = 2\pi q_o$, respectively.

Values for the inner turbulence scale lengths have been given by $l_i \approx 1$ km when $r \leq 2R_\odot$ ([Coles & Harmon, 1989](#)), while the outer scale length was empirically derived by [Wohlmuth et al. \(2001\)](#) from Galileo data to be $l_o = 8.82 \times 10^{-2} r^{0.82}$ [AU] between the ranges of $7R_\odot \leq r \leq 80R_\odot$. As the scale length will not vary greatly within the small region which scattering and refraction occurs in (see [Figure 4.4](#)), we keep a constant outer scale length of $l_o = 300$ Mm, roughly consistent with [Wohlmuth et al. \(2001\)](#). Following [Thejappa et al. \(2007\)](#), the fluctuation scale length is given by $l = l_i^{1/3} l_o^{2/3}$.

The turbulence is included in our Monte-Carlo simulations via a perturbation vector $\langle \mathbf{q} \rangle$ which alters each ray's direction vector at the end of each time-step. The components of $\langle \mathbf{q} \rangle$ are chosen from a Gaussian distribution of pseudo-random numbers of mean 0 and standard deviation

$$\sigma = \sqrt{b\Delta S}. \quad (4.25)$$

Here, ΔS is the distance the photon has travelled in one time-step, and b is the mean-square deviation per unit length, given as

$$b(f) = \pi \left(\frac{f_{pe}}{f\rho} \right)^4 \frac{\epsilon^2}{l}, \quad (4.26)$$

where f_{pe} is the electron plasma frequency, f is the photon frequency, and $\epsilon = \langle \delta n_e^2 \rangle^{1/2} / n_e$ is the level of density fluctuations. It should be noted that, despite the different assumptions used by [Thejappa et al. \(2007\)](#) in the derivation of this

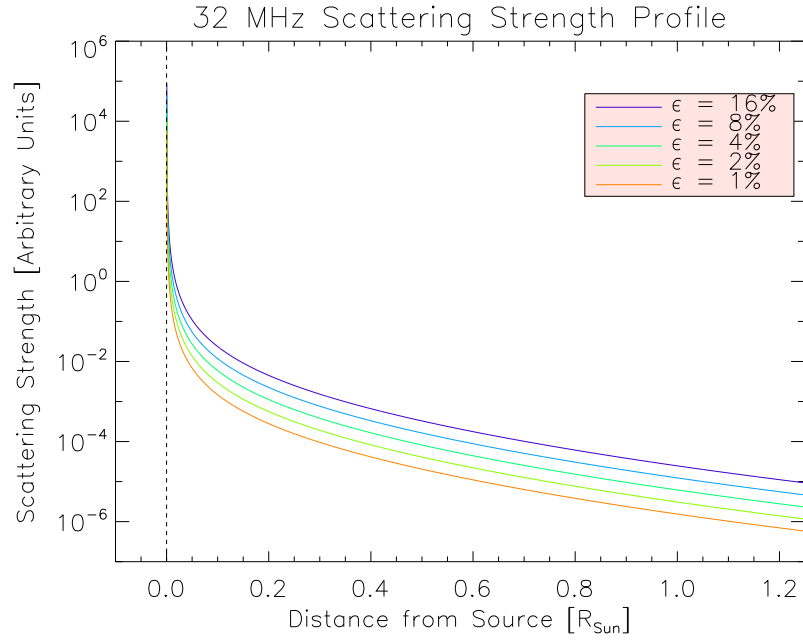


Figure 4.4: Scattering strength as a function of distance from the source and fluctuation level. The different coloured lines represent different fluctuation levels, and the dashed line shows the source.

equation (assuming the density fluctuations form a power-law), it only differs from Equation (1.48) by a small factor. This was varied over different simulation runs as $\epsilon = [0, 0.005, 0.01, 0.02, 0.04, 0.08]$ so that comparison with observations could allow us to constrain the range of fluctuation amplitudes possible.

As the scattering strength, $b(f)$, varies greatly with distance from the source (e.g. for 32 MHz rays - going to \sim zero at $0.5R_{\odot}$ from the source; Figure 4.4) the simulation time-step Δt was kept as a constant, producing a variation in distance-step as $\Delta S = \rho c \Delta t$. This ensured that rays close to the source could not be over-scattered, while far from the source the scattering is negligible enough to ignore scattering effects. The simulation time-step was set as $\Delta t = 5 \times 10^{-3}$ s, to ensure numerical stability.

4.2.6 Anisotropy

We account for the possibility of anisotropic scattering (assuming the ray is preferentially scattered across the face of the Sun) via the conversion of the wavenumber

components from Cartesian coordinates to parallel and perpendicular (to the normal to the solar surface) components. This is done as,

$$\mathbf{q}_{\parallel} = (\mathbf{q} \cdot \hat{n})\hat{n}, \quad (4.27)$$

$$\mathbf{q}_{\perp} = -\hat{n} \times (\hat{n} \times \mathbf{q}), \quad (4.28)$$

where \hat{n} is the normal defining the radial direction (Figure 4.5). The perturbation vector $\langle \mathbf{q} \rangle$ is split into parallel and perpendicular components ($\langle \mathbf{q}_{\parallel} \rangle$ and $\langle \mathbf{q}_{\perp} \rangle$), and the perturbation strength is set as $\sigma_{\perp} = \alpha_{\perp:\parallel} \sigma_{\parallel}$, where $\alpha_{\perp:\parallel}$ is an anisotropy scaling factor. The perturbation is then added to the direction cosine, and the Cartesian coordinate system components are found via

$$q_x = \mathbf{q}_{\parallel} \cdot \hat{x} + \mathbf{q}_{\perp} \cdot \hat{x}, \quad (4.29)$$

$$q_y = \mathbf{q}_{\parallel} \cdot \hat{y} + \mathbf{q}_{\perp} \cdot \hat{y}, \quad (4.30)$$

$$q_z = \mathbf{q}_{\parallel} \cdot \hat{z} + \mathbf{q}_{\perp} \cdot \hat{z}. \quad (4.31)$$

We vary the perturbation level between $\alpha_{\perp:\parallel} = [1, 3]$, and also model extreme cases of $\sigma_{\perp} = 0$ and $\sigma_{\parallel} = 0$.

4.2.7 Absorption

With every interaction between radio-waves and matter, the incident photons have a chance of being absorbed by the background plasma via inverse bremsstrahlung (Melrose, 1980a). This is included in simulations via the monitoring of each ray's optical depth coefficient τ , given by Ratcliffe & Kontar (2014) as the path integral

$$\tau = \int_{r_{source}}^{r_{observer}} \frac{\gamma_d}{v_g} ds, \quad (4.32)$$

where v_g is the group velocity (given by $v_g = \rho c$) and γ_d is the collisional damping rate. For inverse bremsstrahlung, this rate is given by

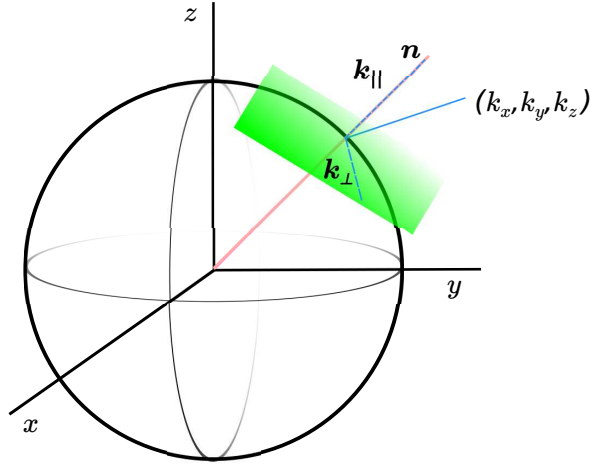


Figure 4.5: Converting from Cartesian coordinates to Sun-centred coordinates. The \mathbf{k} -vector is converted from (k_x, k_y, k_z) to \mathbf{k}_{\parallel} and \mathbf{k}_{\perp} , the parallel and perpendicular \mathbf{k} -vectors respectively. Here the red line shows the normal to the sphere at the point (x, y, z) , and the green plane shows the plane orthogonal to the normal.

$$\gamma_d = \frac{4\pi e^2 \ln \Lambda}{3m_e v_{Te}^3} \sqrt{\frac{2}{\pi}} \left(\frac{\omega_{pe}}{\omega} \right)^2, \quad (4.33)$$

where e is the absolute value of the electron charge, $\ln \Lambda$ is the Coulomb logarithm, assumed to be 20 in the solar corona ($\sim 1.7 R_{\odot}$), m_e is the electron mass, and v_{Te} is the electron thermal velocity.

If the simulation distance-step is small enough, then Equation (4.32) can be approximated by

$$\tau = \sum_{i=0}^N \frac{\gamma_d(r_i)}{v_g(r_i)} \Delta S, \quad (4.34)$$

where i denotes the timestep, N the maximum number of timesteps, and ΔS is the distance the ray travels in the timestep.

The emissivity of each ray is given by $e^{-\tau}$, and hence the intensity in each time bin (Δt_i) and in each pixel $(\Delta x_j, \Delta y_k)$ is given by

$$I(\Delta t_i, \Delta x_j, \Delta y_k) = \sum_{t \in \Delta t_i, x \in \Delta x_j, y \in \Delta y_k} e^{-\tau}, \quad (4.35)$$

where the spatial and temporal pixel spacing is given by $\Delta a_b = [a_b : a_{b+1}]$.

4.3 Results

4.3.1 Simulation Verification

Once the simulation had been run, some initial checks on the output parameters were compared with analytical solutions to Equations (4.1) and (4.2).

Arrival Time

As the rays are injected at a frequency close to the plasma frequency, it should be expected that the burst observed a distance away will be delayed with respect to rays injected at a much higher frequency. The delay time of the first arriving rays can be found via

$$\Delta t = \int_{r_{source}}^{r_{observer}} \left(\frac{1}{v_g} - \frac{1}{c} \right) ds = \frac{1}{c} \int_{r_{source}}^{r_{observer}} \frac{1 - \rho(r)}{\rho(r)} ds, \quad (4.36)$$

and so a consistency check on any simulation runs can be performed by comparing the arrival time of the first arriving rays with the predicted arrival time, assuming strictly radial transport.

For 32 MHz rays injected at a level of $f = 1.03f_{pe}$, the source distance is $r_{source} = 1.76R_{\odot}$. The observer is placed at a distance of $3R_{\odot}$, and performing the above integral gives an estimated delay time of $\Delta t \approx 0.653s$, found to be consistent with the simulations.

Wavenumber Shift

In addition to comparing the arrival times of rays which propagate directly to an observer, the variation in ray wavenumber can be analytically calculated and compared to simulations. By rearranging Equations (4.3) and (4.1), the ray's wavenumber and time are given as

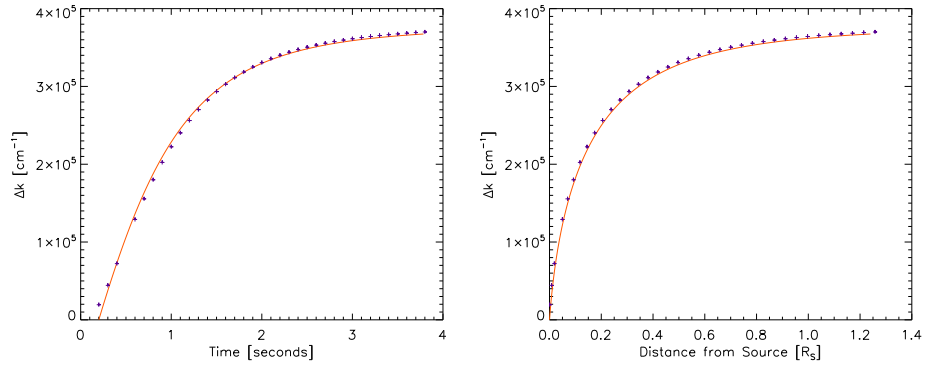


Figure 4.6: Comparison of analytical (red) and numerical (blue crosses) wavenumber values for a single ray, emitted directly towards an observer. Wavenumber shift is shown as a function of time (**left**) and distance (**right**).

$$k = \frac{\sqrt{\omega^2 - \omega_{pe}(r)^2}}{c}, \quad (4.37)$$

$$t = \int_{r(k_0)}^{r(k)} \left(\frac{\partial \omega}{\partial k} \right)^{-1} dr, \quad (4.38)$$

respectively, where $r(k)$ is the ray position at a given wavenumber, and k_0 is the initial wavenumber. Using this form, the wavenumber shift ($\Delta k = k(t, r) - k_0$) was found, and compared with the shift found by tracking a single pseudo-photon in simulations (Figure 4.6), showing good agreement between simulated and predicted values.

Optical Depth

A final confirmation of simulation results is obtained through a comparison of expected and observed optical depth values. Provided a ray's path is known, its optical depth is given exactly by Equation (4.32). To calculate the range of optical depths that should be measured, two ray paths are needed; one direct and one reflected ray.

The path of the direct ray will be given by the integral from $1.76 R_\odot$ to $3 R_\odot$, while the path of the reflected ray will be given by integrals along the paths $1.76 R_\odot \rightarrow 1.75 R_\odot \rightarrow 1.76 R_\odot \rightarrow 3 R_\odot$. Here, $1.75 R_\odot$ is roughly the point at which $f_{pe} > f$, leading to reflection.

Using these two paths, the range of optical depths is analytically found to be

$\tau = [0.032, 0.098]$, which gives the emissivity as $e^{-\tau} = [0.91, 0.97]$. By comparison, this was found to be consistent with the values obtained from simulation runs.

4.3.2 Imaging Scheme

As rays travel away from the source region, the background electron density rapidly drops off, causing the rays' refractive index to approach unity. Effectively, rays which have moved further than one solar radius away from the source experience negligible refraction and scattering. Hence, we model the transport of pseudo-photons from the source to a shell one solar radius away from the source, and assume that the photons travel in a constant direction past this shell. This is shown in Figure 4.7, for density fluctuation levels of $\epsilon = 0\%$ and 8% .

To image the source, the final position (\mathbf{r}) and wavenumber (\mathbf{k}) components are recorded, and the rays are sorted into bins according to their angle cosine from the z -axis ($\Xi_z = z/|\mathbf{r}|$). The rays within a certain range $\Xi_z \in [0.95, 1]$ are then projected onto a plane which passes through the emission source, where the plasma frequency approaches the ray frequency as shown in Figure 4.8. Projection effects at the edges of the images are reduced via limiting the $\Delta\Xi_z$ range over which images are made, although an effort to keep the count-rate as high as possible is also attempted.

The advantage of this method of imaging is that it easily allows for multiple view-points to be simulated, without the need to re-run time consuming simulations. To image from different viewing angles, the coordinate system is rotated by some angles θ and η in the azimuthal and polar directions, respectively, before repeating the imaging process described above. To compare simulated images with observations, the imaging pixel size was chosen as 50 arcseconds for 32 MHz bursts, within the uncertainty range seen in Kontar et al. (2017).

4.3.3 Centroid and Area Variation

As stated above, an important method of probing the density structure in the corona is through the observation of radio source motion. Under the assumption of radiowave

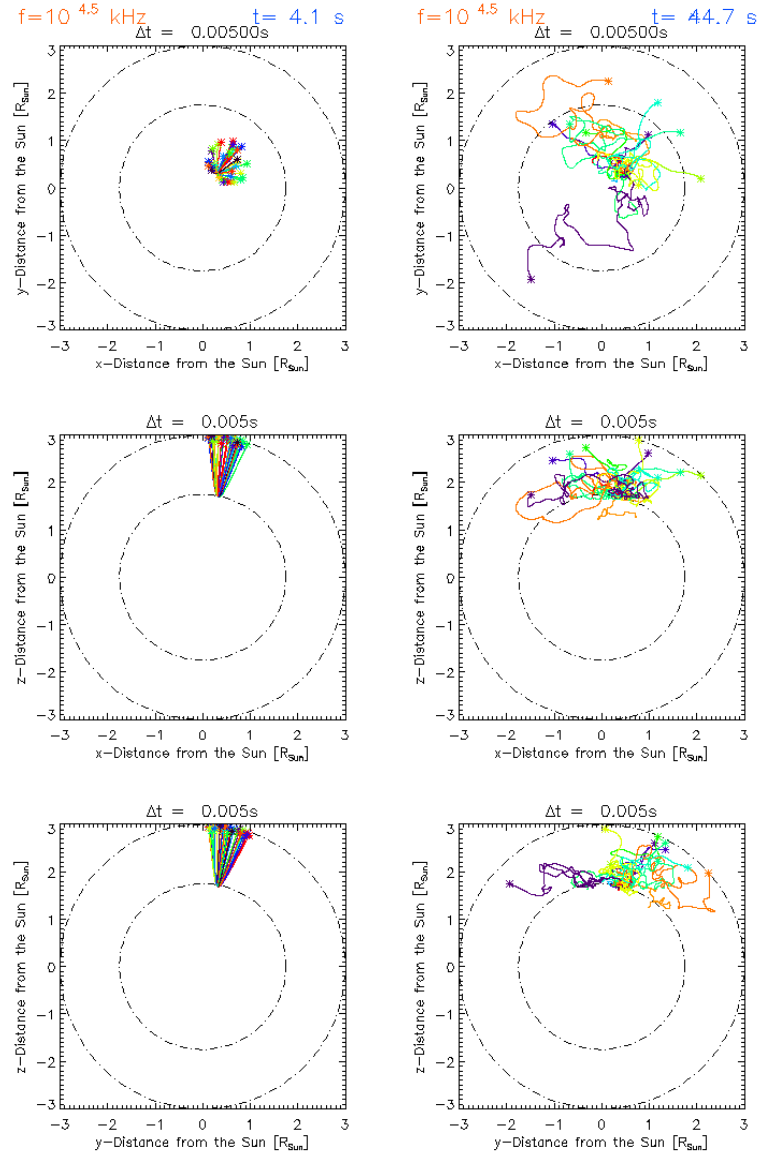


Figure 4.7: Rays showing the passage of 50 photons. The level of density fluctuations is varied from $\epsilon = 0\%$ (**left**) to $\epsilon = 8\%$ (**right**). Asterisks show the positions of photons which exit the simulation. From top to bottom shows (x, y) , (x, z) , and (y, z) views, and the inner and outer circles show the ray reflection point and maximum distances allowed. Above each plot shows the simulation step time Δt , and the ray frequency f and simulation stop time t are shown in orange and blue.

free-streaming, the source properties (i.e. position, size) should directly match the electron beam properties. However, recent observations by [Kontar et al. \(2017\)](#) have allowed for a decoupling of the intrinsic source properties from propagation effects,

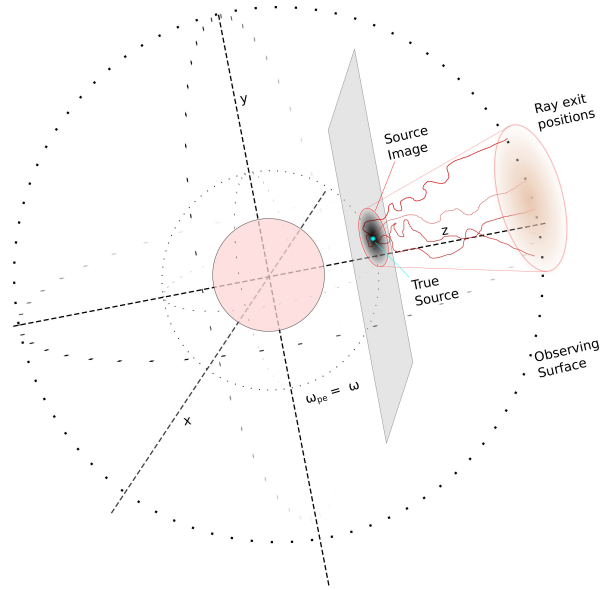


Figure 4.8: Geometry used to make images of the radio sources. The position and direction of travel of each ray is recorded once it passes a certain distance (the Observing Surface), and the population is back-traced to a plane which passes through the emission location. Here, the original point source is represented by a blue dot, and the path of four rays are shown.

showing that scattering and refraction dominate the apparent properties of the source.

Studying the motion and growth of a radio source at a single frequency, an apparent *outwards* radial motion of the fundamental source was observed, along with a rapid growth in both fundamental and harmonic sources. By applying the same imaging techniques used in [Kontar et al. \(2017\)](#) to simulated sources, a direct method to test the effects of radiowave propagation on apparent source area and position is possible.

To calculate the time dependent properties of the apparent source, the simulated lightcurve was divided into 24 equal time segments, and an image was constructed from the rays which reached the observer within the specified time range. To reduce noise in the reconstructed sources, the images were only created from time slices whose integrated flux was above 10% of the maximum.

A 2D elliptical Gaussian was fitted to every imaged source (e.g. [Figure 4.9](#), left), and from this Gaussian the source centroid ($\langle R_s \rangle$) and width were obtained. The source area was given as $A = \pi w_1 w_2 / 4$, where w_1 and w_2 are the semi-major and semi-minor

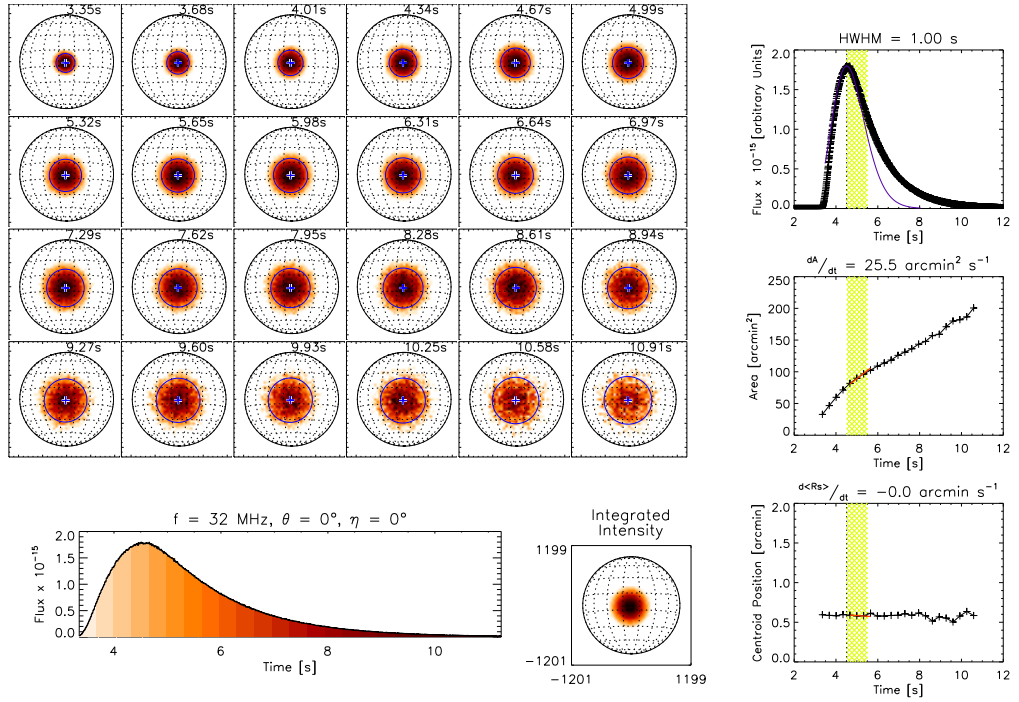


Figure 4.9: **(left)** Reconstructed images of the radio source as a function of time for *isotropic scattering*, with a fluctuation level of $\epsilon = 8\%$. Bottom shows the flux, where the coloured segments show the integration time for each time-slice image. Each image shows the source (red) with 50% contour of Gaussian fit (blue) and centroid (blue cross). **(right, top-bottom)** Specific intensity; source area; and centroid movement as a function of time for *isotropic scattering*. Black crosses show data and coloured lines show fits to the data. Derived gradients dA/dt and $d\langle R_s \rangle/dt$ are noted above each figure.

axes of the Gaussian at a 50% level. Through this method, the FWHM area and centroid position were easily calculated for every time slice.

The source area and heliocentric distance were then studied as a function of time (e.g. Figure 4.9, right). A log-normal distribution was fitted to the flux, and the Half-Width at Half Max (HWHM) after the peak was obtained. Following [Kontar et al. \(2017\)](#), linear fits to the area and distance after the maximum flux were applied, with forms $A = A(t_0) + (dA/dt)(t - t_0)$ and $\langle R_s \rangle = \langle R_s(t_0) \rangle + (d\langle R_s \rangle/dt)(t - t_0)$.

Scattering Effects

In the simplest scattering case (isotropic scattering with a spherically symmetric background), there are only two free parameters which could change the produced images and lightcurves - fluctuation level and viewing angle. To test the effects of fluctuation level upon apparent source properties, the ray paths through background with fluctuation levels of $\epsilon = [0, 0.5, 1, 2, 4, 8]\%$ were computed. The sources were imaged as described above, from an observer at an angle of $(\theta, \eta) = (20^\circ, 0^\circ)$ (e.g. Figure 4.9).

As expected, a clear relationship between apparent source area and scattering strength was found (Figure 4.10, left), with doubling fluctuation level increasing the apparent source area by $\sim 2 - 3\times$. This apparent increase is visible at all times, with both the *initial* and *final* sources appearing much larger in runs with higher fluctuation level.

A relationship between apparent source heliocentric distance and fluctuation level was harder to find (Figure 4.10, right). For fluctuation levels 2–8%, it was seen that increased fluctuations produced a greater outwards radial shift of the apparent source, while for lower fluctuation levels the source followed more complicated trajectories. However, low countrates at small ϵ (due to refraction keeping most rays within a small solid angle away from the observer) reduce the reliability of any fits produced.

Interestingly, it was seen that higher fluctuation level did not always produce more rapid movement of the apparent source, with the highest fluctuation level modelled resulting in a slower drifting source than lower fluctuation levels modelled. Similarly, the fluctuation level was not always seen to produce the largest absolute shift in source centroid, with the highest fluctuation level source remaining closer to its original position than lower fluctuation level sources; although the highest fluctuation level resulted in the furthest centroid shift from the disk centre. Currently there is no explanation for this feature, as it opposes the expectation that increased fluctuation level would produce larger variation in apparent source position. In all cases, it was observed that the apparent source moved radially towards the disk centre with time.

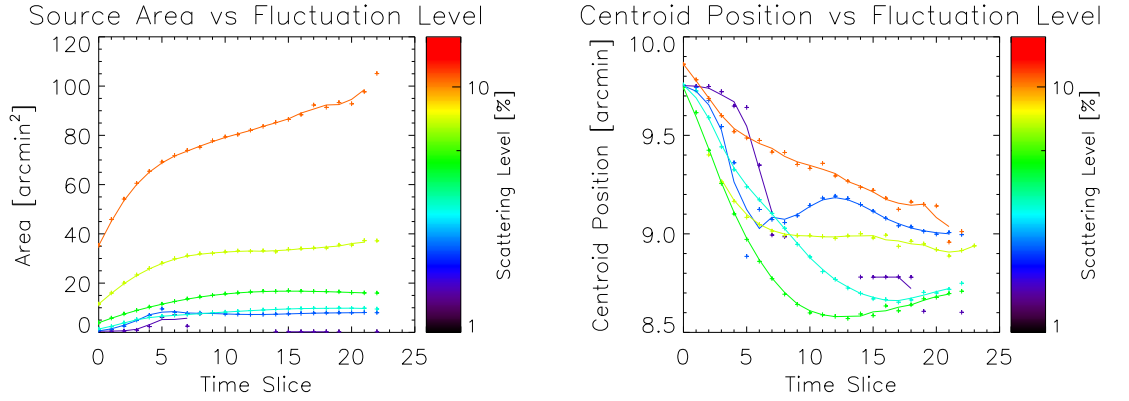


Figure 4.10: **(left)** Source area and **(right)** source centroid distance from disk centre as functions of time and fluctuation level. In both plots the points represent the measured parameters, and the lines show a 3-point moving average. Here the viewing angle was kept constant at $(20^\circ, 0^\circ)$.

Viewing Angle Effects

To assess the effects of off-axis observers, bursts from multiple azimuthal angles were analysed, keeping the fluctuation level constant at $\epsilon = 8\%$. To reduce uncertainties in low countrate fits, the observer’s angular range was kept within $\theta \in [0^\circ, 45^\circ]$.

As before, the FWHM areal extent of each apparent source was calculated through the elliptical Gaussian fit, and the effect of changing viewing angle was seen (Figure 4.11, left). For all angles, the initial apparent source is seen to decrease with increasing viewing angle, similar to Kontar & Jeffrey (2010); Jeffrey & Kontar (2011) who found increasing compression of simulated X-ray sources with larger viewing angle. The source expansion rate is roughly constant for smaller viewing angles, while at larger angles ($> 30^\circ$) the expansion rate increases greatly, resulting in extremely large sources at late times.

For every angle, the relative centroid shift ($\Delta\langle R_s \rangle = \langle R_S(t) \rangle - \langle R_S(t_0) \rangle$) was calculated (Figure 4.11, right). In every case, the source was seen to “drift” towards the disk centre with time, with a clear dependence of radial drift speed viewing angle. For low angle ($\lesssim 3^\circ$) observations, the source remained centred at the disk centre, while at large angle observations the source appeared to drift up to $\sim 0.5R_\odot$.

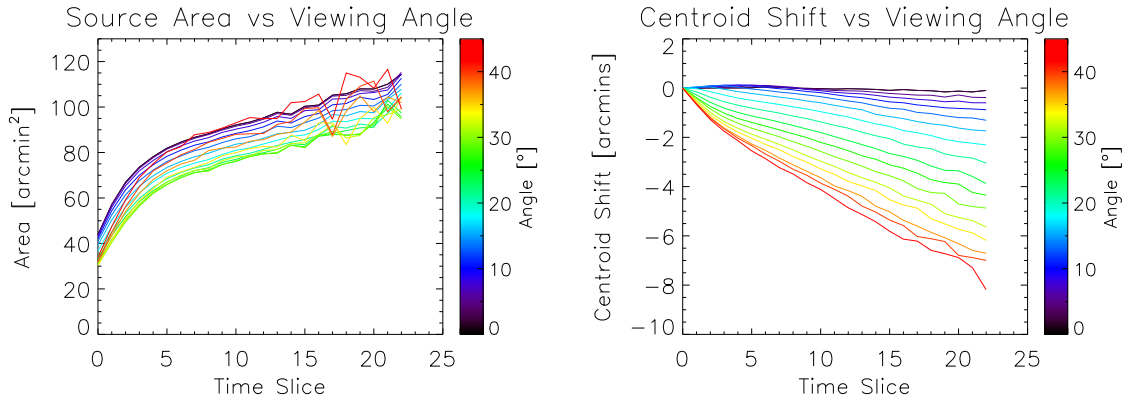


Figure 4.11: Source centroid shift as a function of time and viewing angle. Here the fluctuation level was set as $\epsilon = 8\%$.

Isotropic vs Anisotropic Scattering

To assess the effects of anisotropic scattering on images, the observer was rotated by $(15^\circ, 15^\circ)$ in the polar and azimuthal directions, such that the apparent source was initially placed in the north-west quadrant of the Sun (imitating the observed source position in [Kontar et al., 2017](#)). Both isotropic ($\alpha_{\perp:\parallel} = 1$) and anisotropic ($\alpha_{\perp:\parallel} = 3$) scattering models were simulated, with the scattering strength set at $\epsilon = 4\%$ and a spherically symmetric background density profile present.

Several similarities between the resultant images and lightcurves are present. In both cases, the HWHM burst duration and HWHM centroid drift rate are comparable (Figure 4.12, top & bottom). However, two significant deviations are also present. Firstly the centroid drift rate tends towards zero at times far past the peak in the isotropic case, while in the anisotropic case it remains roughly constant at all times. Secondly, anisotropic scattering greatly affects the apparent areal extent, with both the initial source area and general expansion rate increasing in simulations with anisotropic scattering.

Symmetric vs Asymmetric Density Profiles

Finally, the effects of asymmetric background density profiles on apparent source geometry was considered. The background density profile was varied as in Section 4.2.4,

where a single Gaussian over- or underdensity was added to the spherically symmetric background profile, with ratios of $N = 0.2\times$ and $N = 2\times$ the background (see Equation 4.22).

In both the under- and overdensity simulations, the radio source was placed at the edge of the streamer, which would be directed radially \sim North-West away from the Sun, at the top-right edge of the apparent sources in Figure 4.13.

Both over- and underdensity additions produced large effects on the properties of apparent radio sources. In the underdensity case, the asymmetry resulted in the trapping of passing rays, with the walls of the underdensity serving to reflect most escaping rays back into the cavity. By trapping the rays within a small volume, the duration of the burst at the observer was greatly reduced, with a HWHM of around ~ 0.6 s (Figure 4.13).

This repeated reflection also resulted in large incidence angles at the observer, causing a larger apparent source with more rapid growth. The increase in incidence angle also resulted in a change in apparent source direction, featuring both *inwards* and *outwards* radial motion of the centroid. In this instance, the greatest centroid shift was observed to occur close to the burst peak, similar to observations.

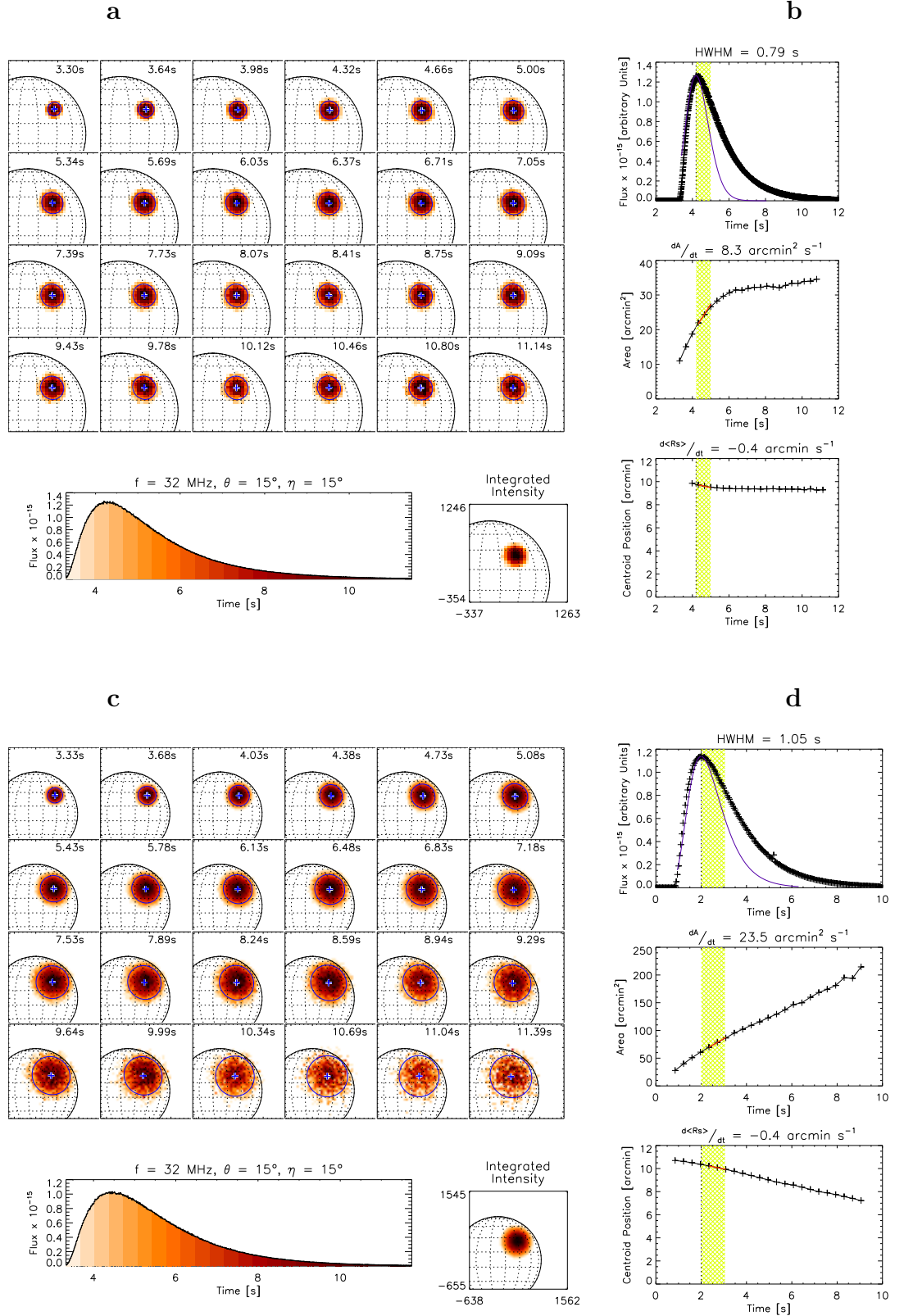


Figure 4.12: Reconstructed images and source parameters as a function of time for isotropic scattering (a & b) and anisotropic scattering (c & d). All simulations feature $\epsilon = 4\%$, and anisotropic results models used $\alpha_{\perp,||} = 3$. Figures are in the same order as Figure 4.9.

In the overdensity case, a similar effect occurs; reflection of rays off the overdensity causes an apparent outwards shift of the source centroid. As larger reflection angles are achieved at later times, an increasingly outwards shift is observed. However, while in the underdensity case rays were trapped and experienced multiple reflections before detection, here on average only a single reflection off the overdensity occurs. This has the effect of both producing a simpler centroid motion (in one direction vs the multi-directional motion seen previously), and producing smaller apparent sources, with greatly reduced expansion rates.

Importantly, both asymmetric density models feature *viewing angle dependancies*, with the apparent source properties varying with viewing angle. While symmetric density models produced roughly constant apparent centroid shifts, with a change in viewing angle only affecting the speed of the shift, in these models it is possible to replicate multiple directions of centroid motion purely by altering the viewing angle.

4.4 Summary and Conclusions

In this chapter, the effects of regular and irregular refraction of low frequency (<120 MHz) solar type-III radio burst images has been studied through numerical simulations of radio propagation effects. A Monte-Carlo simulation of radio-wave propagation through a turbulent medium featuring both large and small-scale density inhomogeneities was used, and the viewpoint of an observer at 1 AU was replicated.

By tracking the apparent motion and growth of an imaged radio source, any propagation effects on simulated radio images were directly determined. By comparing radio source images with the true sources, it was found that isotropic scattering and refraction produce growth of the apparent source, with increasing fluctuation level producing more rapid growth of the source. It was also found that the apparent radio source tends to travel towards the disk centre, with increased viewing angle producing a large increase in apparent source speed. The effects of isotropic and anisotropic density fluctuations were compared, with anisotropic scattering increasing the source growth rate.

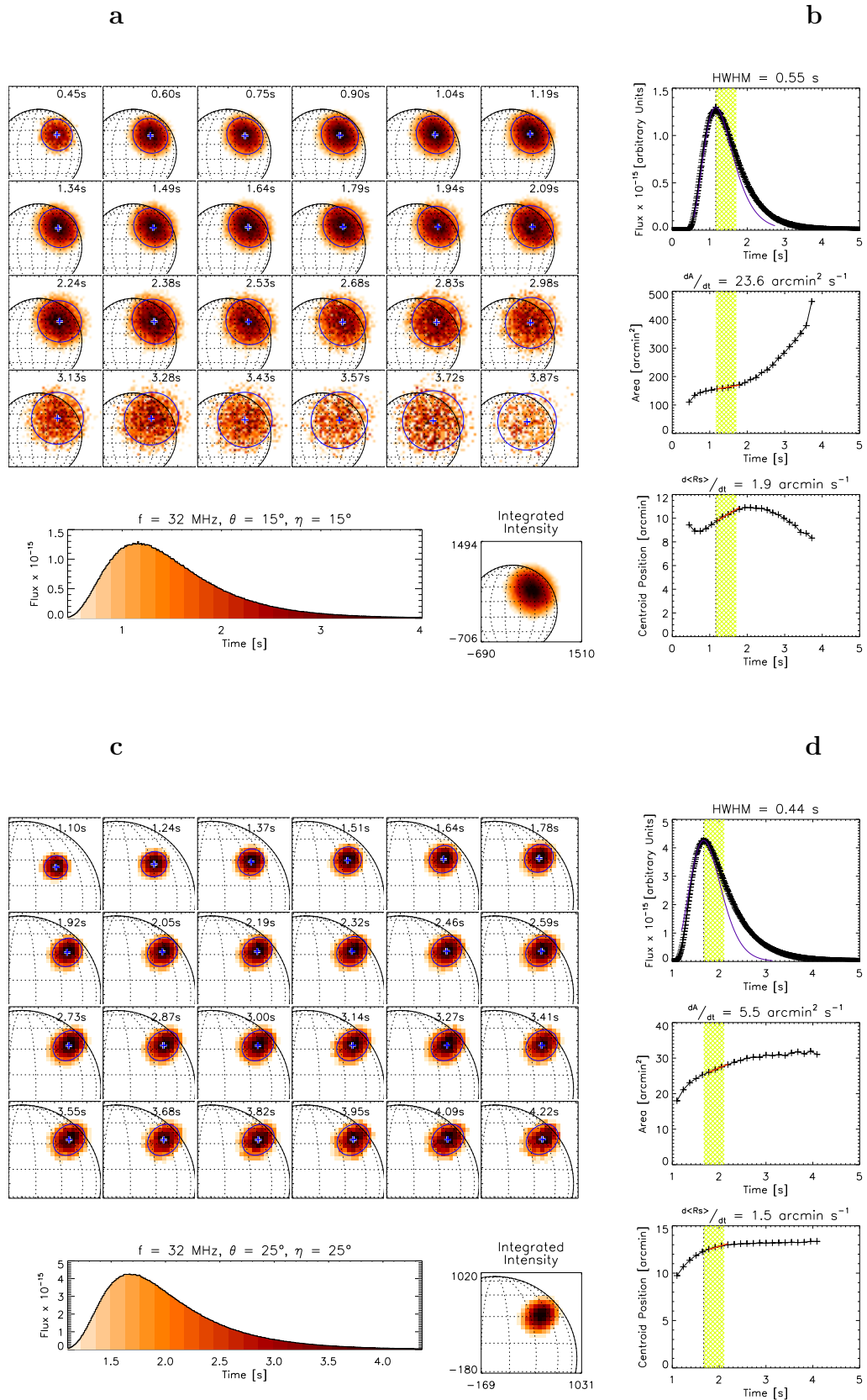


Figure 4.13: Reconstructed images and source parameters as a function of time for an *underdense* (a & b) and an *overdense* (c & d) background. All simulations feature isotropic scattering with $\epsilon = 4\%$. Figures are in the same order as Figure 4.9.

Finally, additional asymmetric density profiles were included in simulations, in order to roughly observe the effects of coronal streamers and coronal holes on radio images and lightcurves. By adding a structure which either serves to trap or reflect incoming photons, large changes to the apparent radio source were produced. Due to the increasing incidence angle of rays at an observer, the apparent source centroid no longer followed a simple trajectory towards the disk centre, and instead exhibited more complicated motion depending upon the angle of observation. The additional density structure also served to expand the apparent source, increasing the areal growth rate significantly compared with the simpler symmetric profile models.

By comparison with observations by [Kontar et al. \(2017\)](#), it appears as though a simple symmetric density model is insufficient to produce outwards radial motion of an apparent radio source. Based upon the more rapid growth and increased area of the source, it seems that the coronal hole model agrees better with observations. However, no coronal holes were reported within the rough area predicted by this simulation at the 16-04-2015 event² - although a small hole was seen a few days earlier³ and potentially could have rotated into roughly the position required, although this is fairly ambiguous association. Similarly, due to the positioning of the source on the solar disk, an association with coronal streamers is hard to deduce. However, a more thorough search of the model parameter space, quantitatively directly matching observations, could assist in confirming or denying either the streamer or hole hypotheses.

More generally, a conclusion has been drawn that complex structures within the corona can produce large changes to the observed radio population. Because of this, the simpler models used by [Steinberg et al. \(1971\)](#); [Thejappa et al. \(2007\)](#), for example, are not always applicable when modelling radio-waves at these frequencies; where coronal structures differ greatly to the quiet Sun symmetric backgrounds.

²https://solarmonitor.org/chimera.php?date=20150416&type=saia_chimr®ion=&indexnum=1

³https://solarmonitor.org/chimera.php?date=20150414&type=saia_chimr®ion=&indexnum=1

Chapter 5

Multilateration of Observed and Simulated Low-Frequency Type-III Radio Burst Sources

5.1 Background

Tracking type-III bursts allows for a direct comparison between observed and expected position (from an interplanetary density and magnetic field models), constraining the density and magnetic structures in the heliosphere. For example, comparisons between white light and radio images allow for the structures in which type-III bursts propagate to be estimated (e.g. [Leblanc et al., 1974](#)).

At higher frequencies (>10 MHz), large interferometric assemblies on Earth can be used to study the Sun (e.g. LOFAR; [van Haarlem et al., 2013](#), the Karl Jansky Very Large Array, the Atacama Large Millimeter Array), producing high resolution spectra and images, and tracking type-III bursts out to a rough distance of $\sim 2.6R_{\odot}$. However, at frequencies lower than ~ 10 MHz, Earth's ionosphere reflects incoming radio waves, requiring the use of spaceborne missions to track bursts out to 1 AU. A consequence of using spaceborne instruments is the lack of imaging at these frequencies. As such, different techniques must be employed in tracking source electrons from the corona out

through the heliosphere.

Direction finding (DF) techniques (also known as *Goniopolarimetry*) for positioning radio bursts have been achieved in a variety of manners. By calculating the null points in the dipole receiver pattern of the Interplanetary Monitoring Platform 6 mission, [Fainberg et al. \(1972\)](#) used the spin-modulation of a type-III burst and an interplanetary density model to locate the position and size of the source electrons. Locating the type-III burst at multiple frequencies revealed an underlying spiral trajectory of the source motion, in good agreement with the Parker Spiral model of the interplanetary magnetic field.

The need for a density model can be removed via the inclusion of additional spacecraft, giving the source location as the intersection of the derived possible source positions. DF via multi-spacecraft observations has been used by [Weber et al. \(1977\)](#), who used both spin-modulation patterns and time-difference-of-arrival (TDOA) methods to locate several type-III radio sources. More recently, [Reiner et al. \(1998\)](#) used similar spin-modulation analysis of the Wind and Ulysses spacecraft to determine the direction of an incoming burst relative to each spacecraft, and hence triangulate the source location via line-of-sight intersections.

From late 2007 - mid 2014, continuous observations of low-frequency (0.125 – 16.025 MHz) radio emission from multiple viewpoints has been made with the *WAVES* instrument aboard the Solar TERrestrial RELations Observatory (STEREO; [Bougeret et al., 2008](#), see §1.7.2 for a more full description of the instruments). The STEREO spacecraft are two 3-axis stabilised solar orbiters with orbital radii of ~ 0.95 AU and ~ 1.01 AU. This difference in orbit puts one spacecraft ahead of Earth's orbit (STEREO-A), and one behind (STEREO-B). As the spacecraft are three-axis stabilised (Sun facing), no demodulation is required to find the direction of arrival of radio sources, and hence triangulation of sources is much easier to achieve ([Cecconi et al., 2008](#)). By measuring the auto- and cross-correlations between the received signal at three (x, y, z) antennas, the direction and polarisation of incoming emission can be determined and the source location can be triangulated.

Observations from the STEREO spacecraft have been combined with spin-modulation

DF from the Wind spacecraft by [Reiner et al. \(2009\)](#), who determined the emission locations of two type-III bursts in December 2007/ January 2008, when the STEREO separation angle was large enough to allow accurate triangulation. The same events were analysed by [Martínez-Oliveros et al. \(2012\)](#), who used an eigenvalue determination scheme to find the source direction and polarisation independently, and found roughly consistent results for source locations.

However, one problem with methods used in the references listed above is the assumption of free-streaming. As has been shown in Chapter 4, photon propagation effects can affect the apparent size and position of imaged type-III sources, and can delay the arrival of rays to observers at different viewing angles. Some attempt to include the effects of refraction in DF has been used by [Thejappa & MacDowall \(2010\)](#), who used a combination of TDOA techniques and an intensity ratio comparison to locate a type-III burst observed by both STEREO spacecraft.

In this chapter, we use a simple TDOA multilateration method to locate multiple low frequency (≤ 2 MHz) type-III bursts observed over the period 2007–2014 by the Wind and STEREO spacecraft. We then use the same method to locate simulated low frequency sources, including the effects of refraction and scattering, and observing the effects on derived source location. Section 5.2 introduces the multilateration scheme, and Section 5.3 applies it to a single event. Section 5.4 describes the numerical simulation, and Section 5.5 compares results from observations with simulations. Finally, conclusions as to the state of density fluctuations present within interplanetary space are drawn in Section 5.6.

5.2 Multilateration Technique

TDOA techniques have extensively used in many fields, such as artillery fire positioning used from WWI (*sound ranging*; [Bateman, 1918](#)), radio navigation systems used by the Royal Air Force during WWII, and more recently, positioning of underwater bodies ([Gamroth et al., 2011](#)). Although the applications vary, the method remains the same; by observing the difference in arrival time of a signal at receivers placed a distance

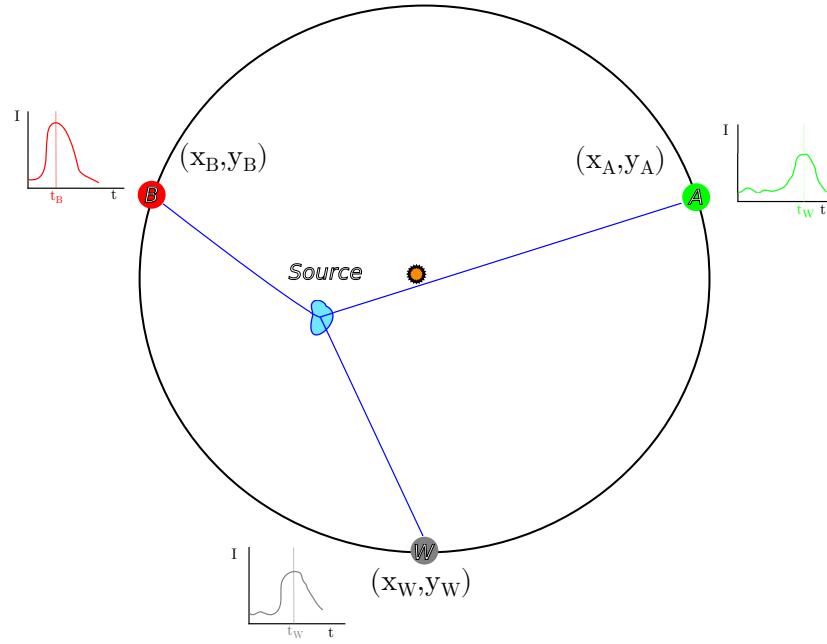


Figure 5.1: Diagram of the spacecraft setup for the TDOA positioning scheme. Three spacecraft (B , W , A) orbit the Sun in the ecliptic plane at roughly the same distance. They each detect a radio burst at times t_B , t_W , and t_A , and their positions are denoted by $(x, y)_{B,W,A}$.

apart, a hyperbola containing possible source locations can be constructed (Weber et al., 1977). Through the use of three or more receivers, the true source location can be determined via the intersection of multiple hyperbolae.

To use this method to track low frequency (< 2 MHz) type-III radio bursts, the Wind and STEREO spacecraft were used. Figure 5.1 shows a diagram of the positions of the Wind and STEREO spacecraft during a hypothetical event, where emission from a source is observed by all three spacecraft at different times.

If the radio burst is assumed to travel freely at a constant speed from emission time t , then the distance travelled from the source (x, y) to a spacecraft (e.g. B at x_B, y_B) is equal to the time of arrival multiplied by the wave speed (c),

$$c(t_B - t) = \sqrt{(x_B - x)^2 + (y_B - y)^2}. \quad (5.1)$$

In the case of a single spacecraft observation, none of x , y , or t can be uniquely

determined. However, by taking the time of arrival difference between two spacecraft at different positions (say A and B), the emission time can be removed from Equation (5.1), giving

$$c(t_B - t_A) = \sqrt{(x_B - x)^2 + (y_B - y)^2} - \sqrt{(x_A - x)^2 + (y_A - y)^2}. \quad (5.2)$$

By transforming the spacecraft coordinate system such that A and B sit on a line with $x_B = x_A = 0$, and $y_B = -y_A = Y$, then Equation (5.2) can be rearranged to

$$\frac{x^2}{\left(\frac{c\Delta t_{BA}}{2}\right)^2 - Y^2} + \frac{y^2}{\left(\frac{c\Delta t_{BA}}{2}\right)^2} = 1, \quad (5.3)$$

giving a hyperbola (in transformed coordinates) containing all possible source locations which would produce the observed signal time delay. Here Δt_{BA} is the peak time delay between the spacecrafts B and A. By adding an additional spacecraft (within the same plane), the 2D location of the source can be determined (e.g. Figure 5.2), and by adding a fourth (off-plane) spacecraft the full 3D source location can be constrained.

5.3 Data Analysis

5.3.1 Event Selection and Radio Analysis

We worked from an initial list of 160 type-III radio bursts observed by STEREO-A, -B, and Wind (largely provided by J.C. Martínez-Oliveros & V. Krupar, personal communication). Of these, we set the criteria that an analysable event must be visible by all three spacecraft, and must feature high signal/noise ratios in at least 80% of the frequency bands used. Applying these narrowed the list down to 24 events.

To analyse each event, the *WAVES* instruments aboard Wind and STEREO-A and B were used (§1.7.1). For the Wind/*WAVES* instrument, we used minute-averaged data from the *RAD1* and *RAD2* bands, scanning a range of 20 kHz – 13.825 MHz with a resolution of 3 kHz (up to 1.04 MHz), and 20 kHz above (Bougeret et al., 1995). For the STEREO/*WAVES* instruments, 38 second-averaged data were used from the *HFR*

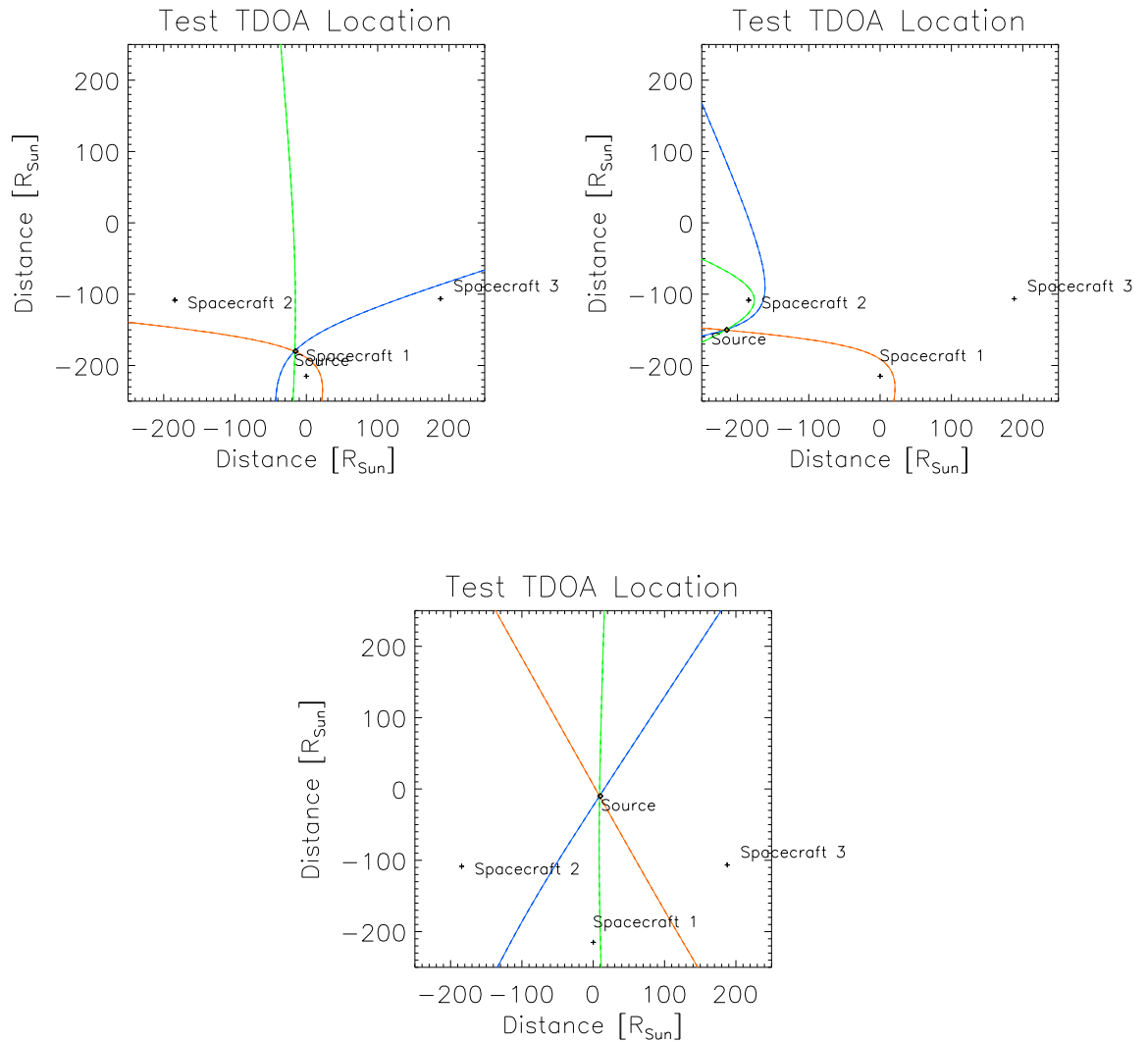


Figure 5.2: Example sources located by three spacecraft using the TDOA method. The spacecraft are shown by black dots and the true source is shown with a black diamond. The location of intersect of the hyperbolae shows the derived source location.

bands, scanning a range of 125 kHz – 16.025 MHz with resolution 50 kHz (Bougeret et al., 2008).

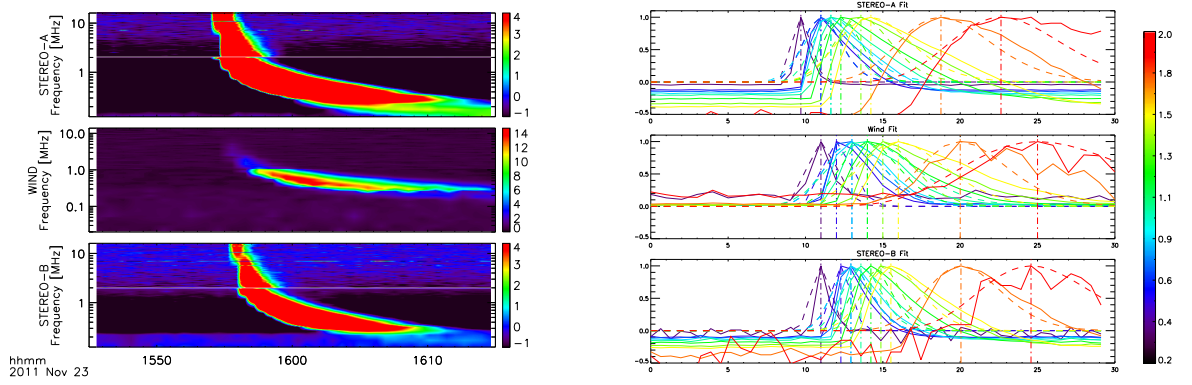


Figure 5.3: **(left)** Dynamic spectra of the 2011-11-23 event, measured by STEREO-A, Wind, and STEREO-B. The colour scale denotes intensity relative to the pre-event background level. **(right)** Single frequency intensities from STEREO-A, Wind, and STEREO-B, normalised to the spacecraft peak intensity. The colour represents frequency (from 2 MHz – 200 kHz). The solid lines show the observed intensities, while the dashed lines show Gaussian fits. The peak time for each frequency (extracted from the Gaussian fit) is shown as a dot-dashed vertical line. All intensities are normalised to their maximum.

5.3.2 Positioning the Sources

As only three spacecraft were used in this study - which all orbit the Sun in the ecliptic plane - we made the assumption that the radio sources were located within the ecliptic plane. This is broadly consistent with studies by [Reiner et al. \(2009\)](#); [Martínez-Oliveros et al. \(2012\)](#); [Krupar et al. \(2014\)](#).

To position the sources, we first obtained dynamic spectra for all the three spacecraft (e.g. Fig 5.3, left). A number of frequency bands in which STEREO/*WAVES* and Wind/*WAVES* frequency values overlapped were selected, and a Gaussian was fitted to the intensity each frequency band (normalised to the maximum). Using this method, the time of peak detection was extracted (e.g. Fig 5.3, right). Although low frequency radio sources are likely to be extended, we assumed that the peak signal detected by each spacecraft corresponded to emission from the source centroid.

For each frequency, the peak time and (transformed) spacecraft positions were

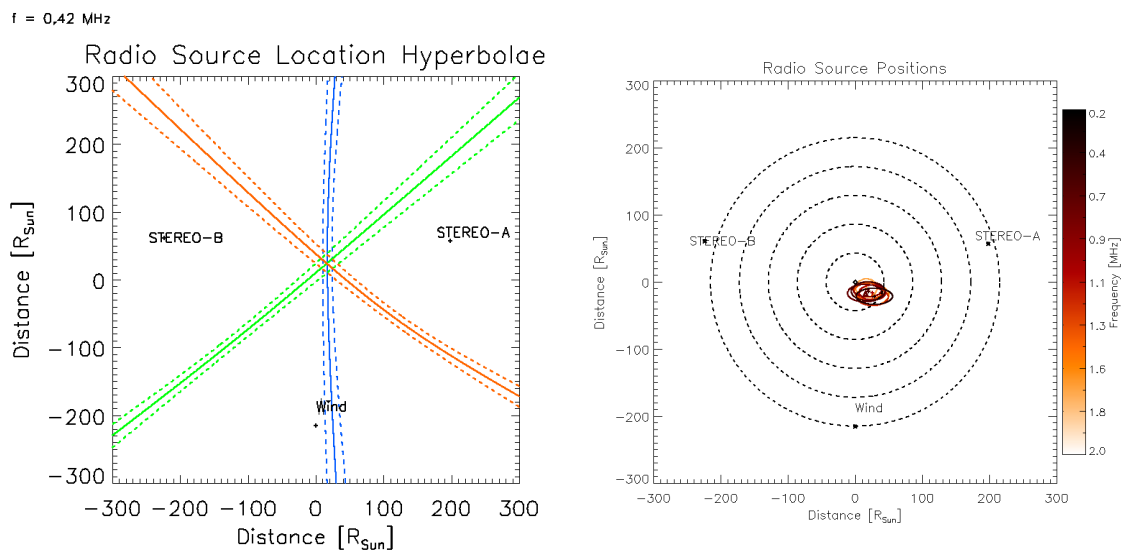


Figure 5.4: **(left)** Hyperbolae of possible source locations for the 425 kHz observations from the 2011-11-23 event. Hyperbolae were created using peak time delays between the STEREO and Wind spacecraft. The solid lines show the mean value, while dashed lines denote uncertainties derived from the instrument time-resolution. The source is located at the point of triple intersection. **(right)** 2D Radio source positions as a function of frequency for the 2011-11-23 event. Points show mean source positions, and ellipses show 2D uncertainties.

then put into Equation 5.3, and the hyperbola of possible source locations was generated. This was done for all three spacecraft, creating three difference hyperbolae - corresponding to the STEREO-B/Wind delay, the Wind/STEREO-A delay, and the STEREO-B/STEREO-A delay. Uncertainties for the hyperbolae are taken from the spacecraft time resolution, of 60s (Wind) and 38.05s (STEREO-A/B). Example source location hyperbolae are shown for one frequency in Figure 5.4 (left), and the derived source locations for all frequencies for this event are shown in Figure 5.4 (right).

5.3.3 Beam Speed

As beam electrons propagate upwards through the corona and out into the heliosphere, they encounter progressively less dense plasma, causing a drop in the plasma frequency

and hence a drop in the type-III emission frequency. Correspondingly, by observing the rate at which the type-III burst frequency changes (the drift velocity; df/dt), the beam speed can be inferred.

In the simplest case, both the source electrons and the radio waves are assumed to travel freely, with the electron beam propagating radially away from the Sun. Under these assumptions, the electron beam speed (v_b) can easily be derived to be

$$v_b = \frac{df}{dt} \frac{2n_e}{f} \left(\frac{dn_e}{dr} \right)^{-1}, \quad (5.4)$$

(e.g. [Li et al., 2008](#)). Using a density model (e.g. Equation 4.21), this equation (hereafter *Method 1*) can be solved for any measured frequency drift rate. The downside of this method is that it requires a density model to calculate the beam speed, and hence is inherently variable. Typical beam speeds calculated using this method lie in the range of $\sim 0.1 - 0.5c$ (e.g. [Melnik et al., 2011](#)).

As the positioning of low frequency sources does not require a density model, multilateration of type-III bursts offers an excellent tool by which the beam speed can independently be estimated. If the assumption of electron and radio free-streaming is kept, then the beam speed can be calculated by simply tracking the motion of the source in time (hereafter *Method 2*).

For every event, both methods were used to calculate the electron beam speed. For Method 1, the time of peak intensity for each frequency was found, and a powerlaw $t_{\text{peak}} \propto f^{-\alpha}$ was fit to the data, giving the frequency drift (and hence beam speed) as a function of frequency (Figure 5.5, left). For Method 2, the heliocentric source distance from the Sun was assumed to vary linearly in time, as $s = v_b t + s_0$ (Figure 5.5, right).

5.4 Monte Carlo Simulations

To test the extent to which the free-streaming assumption is valid, we next model the transport of radio waves through a turbulent medium, featuring large and small scale density inhomogeneities. To model the passage of the radio waves, we use the same

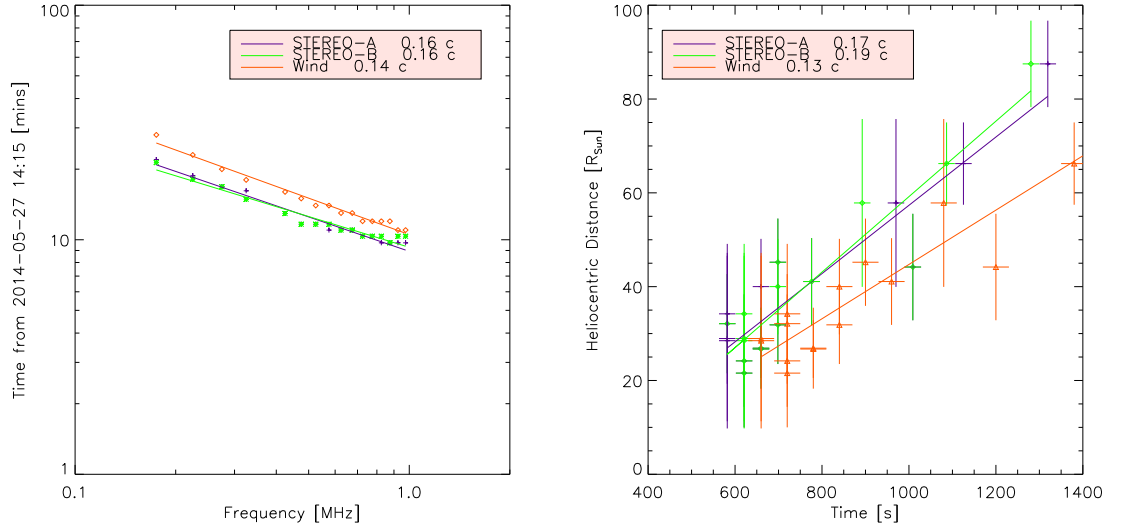


Figure 5.5: **(left)** Electron beam speed derived using the observed dynamic spectrum and the Parker density model. **(right)** Electron beam speed derived using multilaterated source positions.

numerical scheme employed in Chapter 4. We assume that at low frequencies (large distances from the Sun), the density enhancements and reductions provided by active regions, streamers, and coronal holes are greatly reduced; allowing us to assume a spherically symmetric background density profile. We describe the background density profile using the Parker (1958) model with Mann et al. (1999) normalisation at 1 AU, assuming a 1 MK corona.

We inject 10^7 rays along a line $(0, 0, r_z)$, and measure the observed countrate over the full 4π sky from an observer placed $19 R_{\odot}$ away from the Sun's centre. By assuming that no further scattering or refraction of rays occurs past $19 R_{\odot}$, observations from an observer at 1 AU can be deduced from observations at $19 R_{\odot}$. The spatial emission range was chosen as $r_z \in [5, 16] R_{\odot}$, corresponding to a frequency range of $f \in [0.45, 2]$ MHz. The scattering level was varied between $\epsilon \in [0, 0.10]$, the inner scale of fluctuations was taken as 30 km (Coles & Harmon, 1989), and the outer scale as 300 Mm (Spangler, 2002). Only isotropic scattering was considered in these simulation runs.

As before, the rays were assumed to scatter strongly close to the source, isotropising

the directional distribution of emitted rays. Hence, we assumed isotropic emission from the source. As the rays are emitted from different locations, the arrival time was corrected for velocity dispersion, assuming emission from a beam travelling radially with velocity $v_b = 0.2c$.

5.5 Results and Discussion

5.5.1 Density Model Comparison

As the source positions derived using the TDOA method do not depend upon density models, this method offers an excellent comparison tool with theoretical/empirical density models.

Observations

For every event, the source heliocentric distance was plotted as a function of frequency (e.g. Figure 5.6), and a comparison between the observed heliocentric distances and predicted emission distances (from Parker, 1958; Leblanc et al., 1998) was made. Unfortunately, due to the low time resolution of the three *WAVES* instruments used, the uncertainties on individual source locations were large ($\sim 10 - 20R_\odot$). To account for this, we compare the average source position as a function of frequency (between 0.2 – 1 MHz) to the commonly used density models.

We find that, on average, the observed type-III sources appear to lie at much larger distances than predicted by either density model (Figure 5.8). The ratio of the observed to predicted source distances was found by fitting a powerlaw to observations, and comparing with the models. Generally we find the emission to come from distances $\sim 4 - 6\times$ those assuming fundamental emission, or $\sim 2 - 3\times$ those assuming harmonic emission. This is consistent with a statistical study (using DF triangulation) by Krupar et al. (2014), who found $\sim 3 - 5\times$ larger heliocentric source distances than predicted.

As it is unlikely that every event occurs within a large overdensity, the most likely explanation for the disparity between observations and models is scattering and refrac-

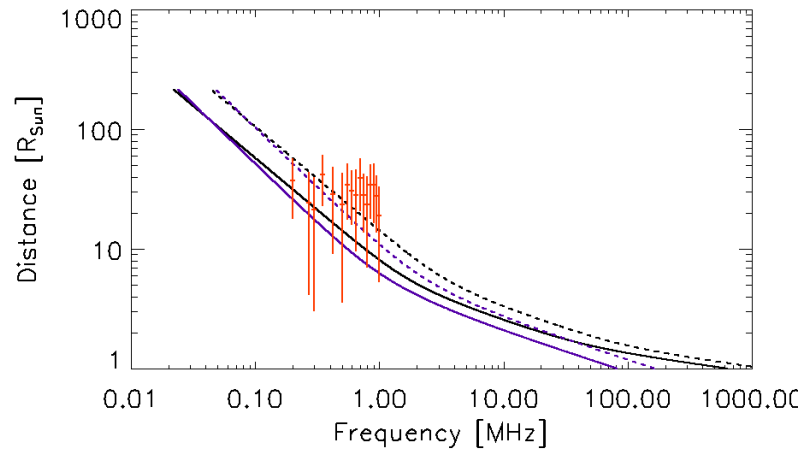


Figure 5.6: Comparison of heliocentric source distances as a function of frequency for the 2011-11-23 event (red with uncertainties) with predicted emission locations from Parker (1958) (black) and Leblanc et al. (1998) (blue) density models. Solid lines show emission distances assuming fundamental emission, and dashed lines show distances assuming harmonic emission.

tion of the radio bursts during propagation causing the apparent source to be shifted radially outwards from the real source.

Simulations

While observations only allow a comparison between the observed source distance and the *predicted* source distance, the positions of simulated low frequency bursts can be directly compared with the true source location. As with observations we located the centroid position of a small frequency range by finding the peak burst time, building the source position hyperbolae, and hence finding the point of triple intersection.

To allow for large angle multilateration, only the highest fluctuation levels ($\delta n_e/n_e = [2\%, 4\%, 10\%]$) were used. For each fluctuation level, five different burst geometries were used: two bursts directed at STEREO-B, and three bursts directed at Wind, with viewing angle ranges from $\pm 45^\circ$ to $\pm 120^\circ$. Figure 5.7 (left) shows the multilaterated 2D source positions for a burst directed at STEREO-B, with Wind and STEREO-A placed

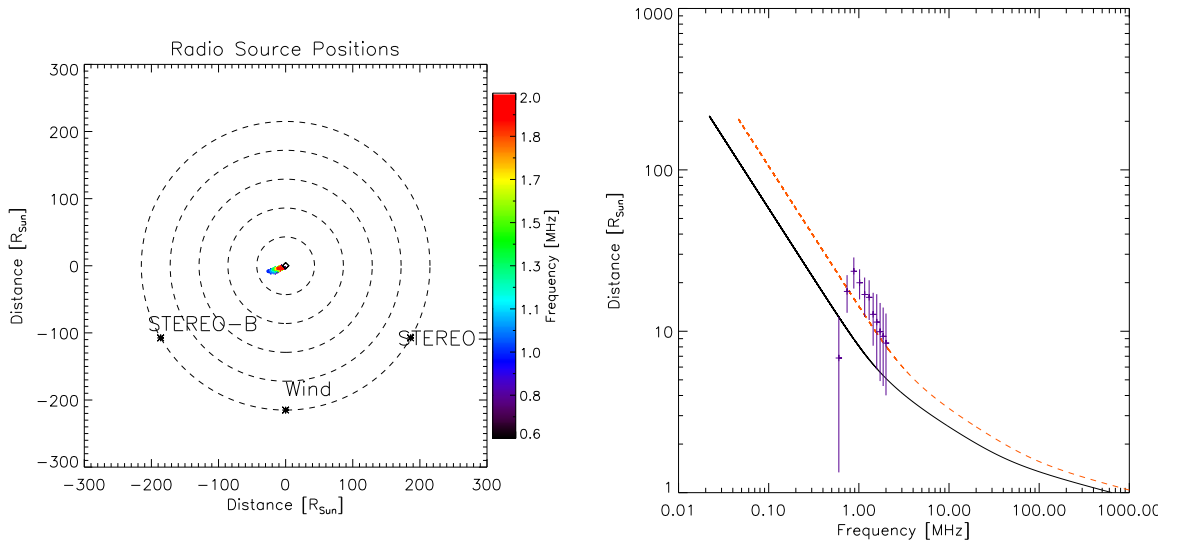


Figure 5.7: **(left)** Simulated 2D radio source positions as a function of frequency for $\delta n_e/n_e = 4\%$. The burst was directed at STEREO-B in simulations. **(right)** Heliocentric source distance as a function of frequency (blue crosses), with a Parker density model overlaid for fundamental (black) and harmonic (red dashed) emission.

60° and 120° away, respectively.

Similar to observations, we find an upwards radial shift in apparent source distance from the Sun (e.g. Figure 5.7, right). Averaging over all five burst geometries, we find that the bursts are shifted roughly $1.5 - 4\times$ further from the Sun than injected, with doubled fluctuation level producing an increased shift of around $\sim 25 - 75\%$.

5.5.2 Excitor Speed

For each event, the source beam speed was calculated via the frequency drift rate and directly through multilaterated source positions (e.g. see Figure 5.5). This method was then repeated with the simulated bursts, allowing for comparison both between the two derived beam speeds, and between the derived and injected beam speeds.

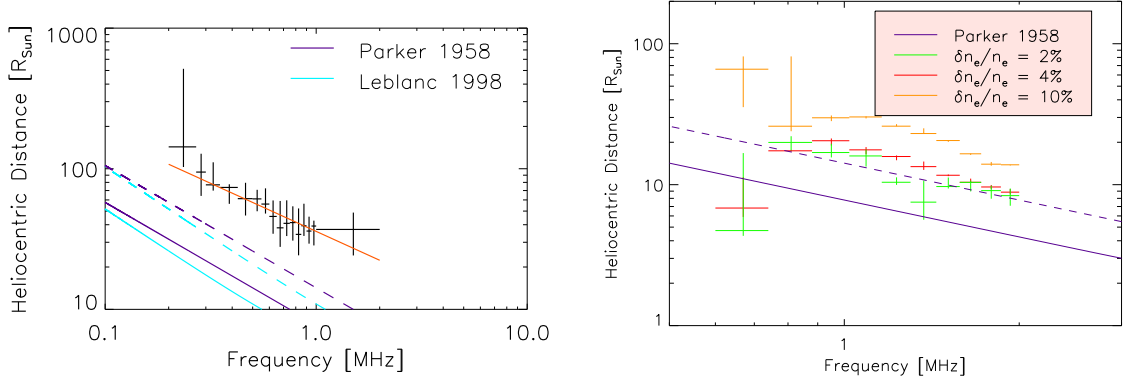


Figure 5.8: Median heliocentric source distances for observed (**left**) and simulated (**right**) events. Crosses show source distances as a function of frequency, with uncertainties arising from the first and third quartile values, while lines show theoretical source distances for fundamental (solid) and harmonic (dashed) emission. (**left**) Crosses show median distances for 24 events. Dark blue lines show the Parker density model and pale blue show the Leblanc density model, and a powerlaw (red) is fit to observations. (**right**) Green, red, and orange crosses show results from simulation runs with $\delta n_e/n_e = 2\%$, 4% , and 10% respectively. Dark blue lines show the Parker density model.

	Method 1 (Parker)	Method 1 (Leblanc)	Method 2
STEREO-A	$0.14 \pm 0.01c$	$0.09 \pm 0.01c$	$0.11 \pm 0.02c$
STEREO-B	$0.12 \pm 0.01c$	$0.08 \pm 0.01c$	$0.10 \pm 0.01c$
Wind	$0.14 \pm 0.02c$	$0.09 \pm 0.01c$	$0.12 \pm 0.02c$

Table 5.1: Average beam speeds calculated for all events. Uncertainties are given by the standard error.

Observations

The source beam speed was calculated for every event, and the average speed as determined by each method was considered (Table 5.1). To calculate the beam speed from Method 1, both the Leblanc and Parker density profiles (Equations 1.24 and 4.21 respectively) were considered.

On average we find that the beam speeds calculated using Method 2 agree with derived speeds using both Leblanc and Parker density models. However, this is possibly due to large uncertainties, as the beam speeds derived via the two models disagree with each other, with the Parker model requiring $\sim 50\%$ faster bursts to produce the observed frequency drift rates. Beam speeds derived via multilaterations are $\sim 25 - 30\%$ slower and faster than those inferred using Parker and Leblanc models, respectively. Without direct measurements of the background density profile at the time of emission, any further differentiation between the two density models is impossible. Hence, to deconvolve propagation effects from intrinsic source properties, simulations with a prescribed density profile are required.

Simulations

For each run of the simulation, the data were sorted into time bins of width 5s and frequency bins of width ~ 80 kHz, and a dynamic spectrum was built. Each frequency bin was normalised to the peak intensity, and a log-normal distribution was fit to the data to find the peak time reliably. A powerlaw was then fit to the frequency vs peak time, and from this the frequency drift rate was calculated (e.g. see Figure 5.9). From the frequency drift rate, the apparent beam speed was given by Equation (5.4), and the effects of both scattering strength and viewing angle on apparent beam speed were considered.

By varying the density fluctuation level from 0% to 10%, we find a relative delaying of low frequency rays with respect to high frequency rays (Figure 5.9). This causes the apparent beam speed to decrease from $0.15c$ (75% of the injected beam speed; $v_b = 0.2c$) to $0.02c$ (10% of the injected beam speed). Interestingly, we find that even with no scattering, refraction of the rays is strong enough to produce an apparent beam speed drop.

At large viewing angles ($> 45^\circ$), no emission is visible in simulations with low levels of density fluctuations. This is due to refraction dominating the directivity of the burst, forcing the emitted rays into a narrow cone. For higher density fluctuation

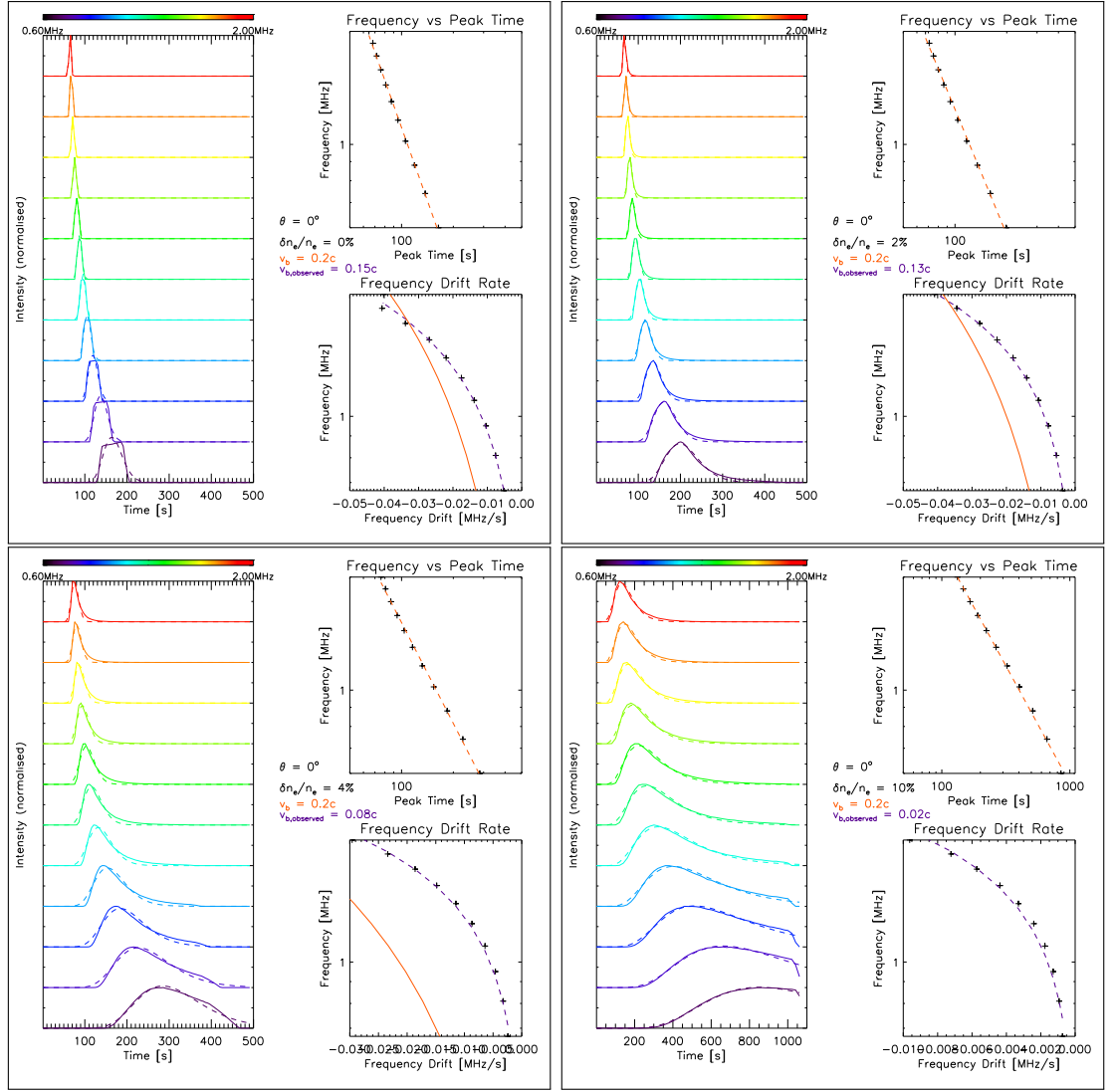


Figure 5.9: Simulated multi-frequency intensity plots, for scattering levels $\delta n_e/n_e = [0\%, 2\%, 4\%, 10\%]$ (shown in the **top left**, **top right**, **bottom left**, **bottom right** quadrants respectively), observed from a viewing angle of 0° . Each quadrant shows: (**left**) Multi-frequency intensities, normalised to peak intensity (solid lines) with log-normal fit (dashed lines). Colour denotes frequency, from 0.6 MHz – 2 MHz. (**right, top**) Frequency vs peak time (black crosses) with powerlaw fit (red dashed). (**right, bottom**) Frequency vs drift rate (black crosses) with powerlaw fit (blue dashed). The solid red line shows the expected frequency drift rate given $v_b = 0.2c$.

levels, however, the bursts can still be observed, albeit with higher noise levels due to

the limited number of pseudo-particles used in the Monte-Carlo simulations.

Similar to the effect of increasing the density fluctuation level, we see a decrease in the apparent beam speed with increasing viewing angle - from $0.08c$ at 0° to $0.06c$ at 90° (Figure 5.10). Due to limitations of the Monte-Carlo simulation used, viewing angles larger than 90° are hard to attain, requiring a significant increase in ray numbers, greatly increasing the simulation run time.

The source distance from the Sun was tracked through time, and the speed of the burst was estimated via a linear fit (Figure 5.11). We find that, similar to beam speed derivations from dynamic spectra, an increase in both viewing angle and background density fluctuation level causes a drop in the apparent source speed.

Bursts directed along an observer's line of sight appear to travel with the prescribed beam speed to that observer. However, bursts directed at some angle to an observer's line of sight experience a delay of the lowest frequencies, causing apparent reduction of around 25% of the mean source speed. Increased fluctuation level also decreases the apparent source speed by around $\sim 40\%$.

5.6 Summary and Conclusions

The properties of interplanetary type-III radio sources have been studied using multiple techniques. We have used a TDOA multilateration technique to locate the source of radio emission for multiple events covering a seven year period, and have used the derived source locations to compare both observed emission distance with commonly used density models, and observed source radial velocities with beam speeds derived from dynamic spectra.

By locating multiple type-III sources, a statistical relationship between source frequency and emission distance from the Sun was derived. By assuming either F- or H-emission, it was found that the type-III sources lie $\sim 4 - 6\times$ or $\sim 2 - 3\times$ further from the Sun than predicted by commonly used density models, consistent with a study by Krupar et al. (2014). This apparent statistical enhancement of electron density in the heliosphere is attributed to scattering and refraction of the radio waves during

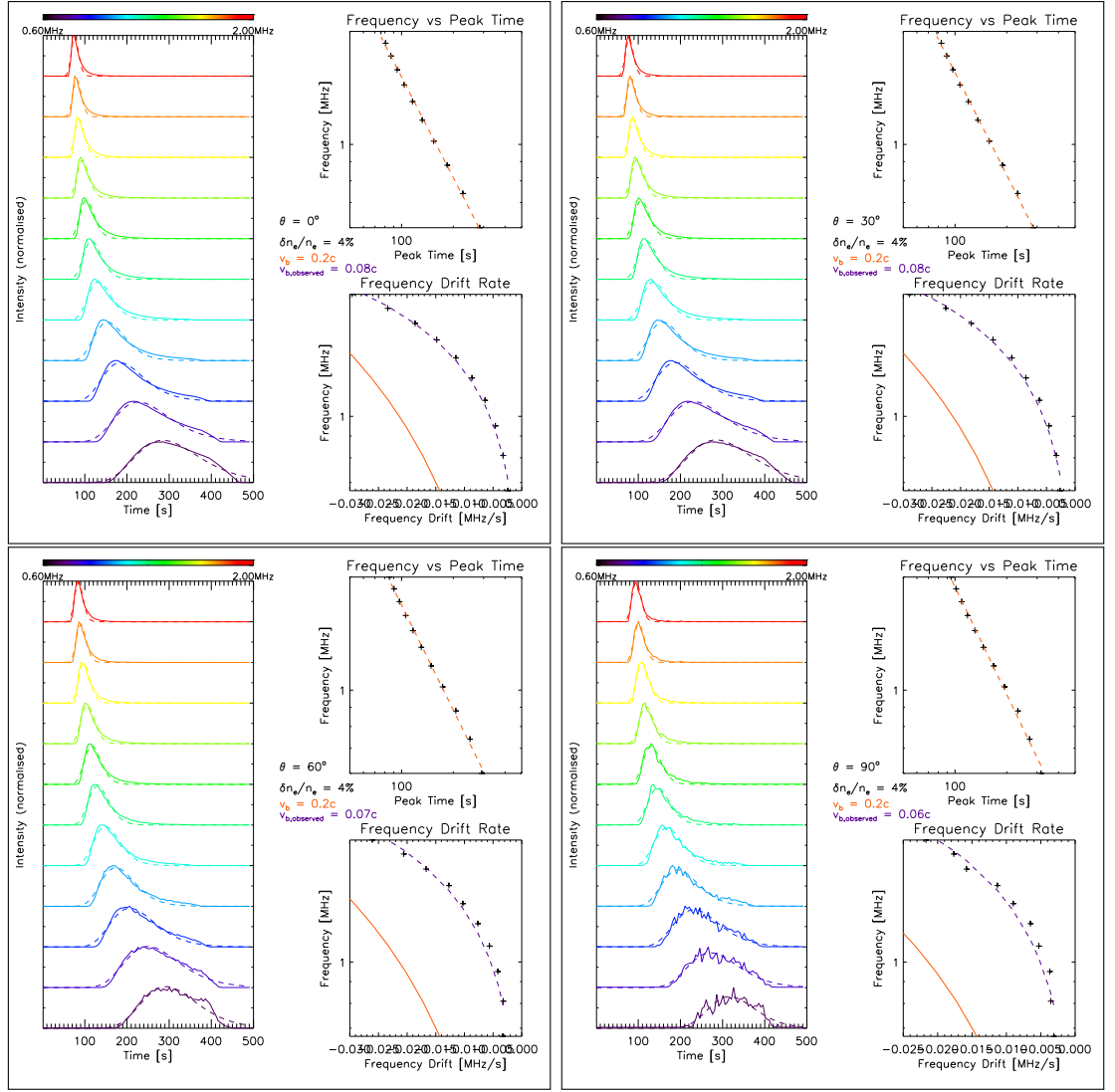


Figure 5.10: Simulated multi-frequency intensity plots, for scattering levels $\delta n_e/n_e = 4\%$, as viewed from angles $\theta = [0^\circ, 30^\circ, 60^\circ, 90^\circ]$ (shown in the **top left**, **top right**, **bottom left**, **bottom right** quadrants respectively). Each quadrant is laid out as in Figure 5.9.

propagation.

The similarity of results between this study and that of Krupar et al. (2014), however, leads to a complication in the drawing of conclusions about this work. In simulations used here, an assumption was made that the photon population scatters/refracts strongly close to the source, and travels scatter-free past $\sim 1 R_\odot$ from the source.

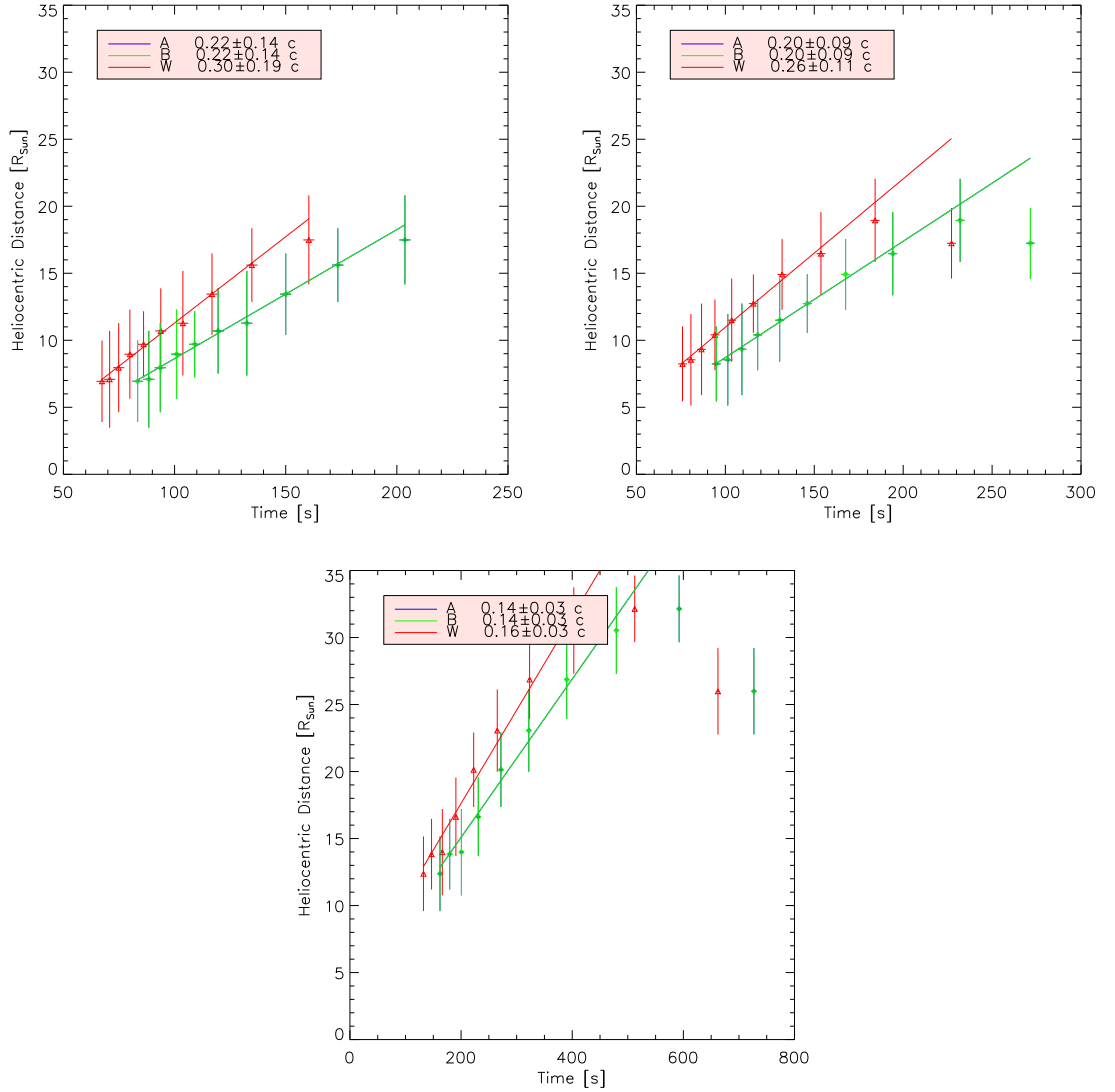


Figure 5.11: Simulated source positions as a function of time, for a burst directed at Wind with STEREO-A and STEREO-B separated by an angle of 180° . The fluctuation levels used here were $\delta n_e/n_e = 2\%$ (**top left**), 4% (**top right**), and 10% (**bottom**). Derived source speeds from each spacecraft are shown in red (Wind), blue (STEREO-A), and green (STEREO-B).

This assumption is based upon the scattering profile (Figure 4.4), which shows a rapid drop-off in scattering strength a short distance from the source. Under this assumption, direction-finding techniques should locate the source at most $1 R_\odot$ away from the true location (i.e. to the point at which scattering/refraction becomes negligible).

However, [Krupar et al. \(2014\)](#) has shown that direction-finding techniques are able to place the apparent sources 10s of solar radii away from their predicted location.

One possible conclusion based upon [Krupar et al. \(2014\)](#) is that the radiowaves experience scattering/refraction to a much greater distance than predicted by scattering models used here. Alternatively, it is possible that the difference in apparent shift as a function of angle causes the directions of rays at the observer to be shifted to such an extent that, when using incidence angles for methods such as triangulation, the intersection of the source-lines (assuming free-streaming) occurs much further out from the source than the position of last scattering. Further study is required to test either hypothesis, and an additional triangulation scheme implemented in current simulations would be able to resolve this dilemma.

Following common methods, the radial velocity of the type-III sources was inferred from dynamic spectra using an assumed density model, and the inferred velocities were found to differ by a factor of $\sim 50\%$ between density models. The radial source velocity was independently derived from the time-distance profile of observed sources, and it was seen that the average derived source velocity agreed with both inferred beam velocities, complicating the analysis of either density model.

We have also tested the effects of refraction and scattering via large and small scale density inhomogeneities on the derived source positions and observed dynamic spectra. A Monte-Carlo simulation of $\sim 0.6 - 2$ MHz fundamental radio transport from a source location to 1 AU was used, and the effects of varying fluctuation level and different viewing angles were considered. By applying the same methods as used on observations to output from simulations, a direct comparison between the true- and observed sources was achieved.

An outwards radial shift in apparent source location was observed, statistically pushing apparent sources around $1.5 - 4\times$ further from the Sun than injected. It was found that enhanced fluctuation level contributes to the shift, with a 10% fluctuation level producing a greater shift of around 125% than results with a 2% fluctuation level. Assuming fundamental emission, real sources are observed to be shifted by around $4 - 6\times$ compared to predictions, consistent with $\sim 10\%$ relative density fluctuation

levels used here.

The apparent radial velocity of observed sources was also calculated, and was compared to inferred beam speeds from multi-angle dynamic spectra. For both methods, an inverse dependence of beam speed upon fluctuation level was found, with enhanced fluctuation level (2% - 10%) causing an apparent $\sim 85\%$ reduction in beam speed derived using both methods, independent of viewing angle. Comparing a larger range of fluctuation levels, a $\sim 90\%$ drop in inferred beam speed from $\delta n_e/n_e = 10\%$ dynamic spectra was seen compared with $\delta n_e/n_e = 0\%$ dynamic spectra. As a whole, it was also seen that inferred beam speeds *always* feature reductions of 25 – 90% with respect to injected beam speeds.

A weaker dependence of apparent beam speed upon viewing angle was also seen via both methods. Speeds derived from multilaterated source positions showed that bursts directed at an observer appear to travel at the injected beam speed, while bursts travelling along the plane of the sky appear to travel slower. Similarly, it was seen that arrival delays of the lowest frequency rays at large angles produces a decrease in the frequency drift rate, causing a reduction in the apparent source beam speed. Interestingly, speeds derived directly from source locations appear to be larger than speeds inferred from dynamic spectra, in disagreement with results from observations which feature general agreement between speeds derived using both methods. However, it is possible that the relatively large uncertainties in observations are causing the derived beam speeds to appear to agree.

By comparing both observations to predictions, and simulations to predictions, the effects of interplanetary scattering and refraction on the apparent positions of low-frequency radio sources has been probed. By using both observational and numerical methods, it has been estimated that density fluctuations of around $\delta n_e/n_e \sim 10\%$ down to the scale of ~ 10 km are required to produce the statistical enhancement of apparent source heliocentric distance, and the general agreement of observed and simulated source speeds provide some backup to this work. The effects of scattering on the observed shapes of the intensity profiles at 1 AU have shown that scattering can have a large effect, leading to false conclusions on the source velocity based purely on

dynamic spectra.

Following the launches of Solar Orbiter ([Maksimovic et al., 2017](#)) and the Parker Solar Probe ([Bale et al., 2016](#)), high time resolution radio observations from multiple viewpoints will be available, allowing for the multilateration of low frequency type-III sources from potentially four spacecraft. High time resolution tracking of sources could be used to further compare the derived beam speeds from both methods, while larger scale simulations could be run to achieve high count-rates at wide viewing angles, and hence allow for full 180° comparisons with observations.

Chapter 6

Conclusions

A significant fraction of the energy released in a solar flare goes into accelerating ambient electrons, which are responsible for both X-ray and radio emission as they travel either down into the solar atmosphere, or up into interplanetary space. The subject of this thesis has been the understanding of the propagation of both the upwards travelling electrons and the subsequently produced radio waves, which are detected at Earth. By studying the time evolution of detected radiation and by comparing observations of multiple particle and wave species, the underlying properties of the background magnetic field and density profiles can be determined. This allows for transport and injection effects to be separated, and the properties of solar electrons to be estimated.

Conclusions have already been drawn at the end of each research chapter, and so only the key details are addressed again here. A larger scale analysis of the work is presented, with importance upon the field as a whole emphasised, and possible future directions and applications of the above work proposed.

6.1 Electron Transport and Scattering

In Chapter 2, the transport of flare accelerated electrons along a turbulent magnetic field from a flare to a near-Earth spacecraft was simulated. The effects of both vary-

ing injection profiles and scattering profiles upon measured time-intensity profiles and peak-flux spectra were found. Fourteen in-situ electron events which featured delayed electron arrival and steeper peak-flux spectra than predicted from HXR observations were studied.

By comparing the normalised time-intensities of simulations and observations, the parameters which best fit observations were found. The simulation data was then re-normalised to RHESSI electron inferences and the simulated and in-situ peak-flux spectra were compared, showing a good match between observations and simulations. Generally it was found that thin-target injections tended to match observations slightly better, although large uncertainties due to the lack of high energy data complicate the drawing of conclusions from the data.

Finally, the simulated and observed anisotropy was compared through the pitch-angle distributions at 1 AU, where generally good agreement was found in most cases. It is noted that the PAD for gradual events tended to match observations better, with more impulsive events featuring less agreement. It was hypothesised that a possible cause of this is subsequent injection of high energy electrons from the flare site, causing long-duration anisotropic distributions to be observed at 1 AU, although further testing is required. In some events, drastic differences are present in the observed PADs, which are attributed to reflection of electrons off nearby ICMEs.

It is noted that the low energy results mostly disagree with observations, probably due to Langmuir wave generation affecting the lowest energy channels. In future, it would be of interest to combine a pitch-angle scattering model of this form with a Langmuir wave simulation (e.g. models used by [Kontar & Reid, 2009](#); [Reid & Kontar, 2015](#)) to determine whether a combined simulation can explain both *late* arrival of high energy particles, and *early* arrival of lower energy particles, relative to the expected arrival time.

In addition to the generation of Langmuir waves, the possibility of 3D motion has been unexplored in this work. While the assumption that a flare-accelerated electron is tied closely to the magnetic field seems likely, due to the relatively low electron momentum, 3D spatial diffusion is still possible. [Laitinen et al. \(2013, 2016\)](#) studied

the effects of meandering magnetic field lines on the diffusion of solar energetic particles, and concluded that wandering field lines could produce large scale diffusion of solar protons in relatively short time-scales, allowing for large-angle observations of a single event. By expanding our event list and re-evaluating work through the inclusion of wide-angle observatories (e.g. the STEREO spacecraft, or the Parker Solar Probe from 2019), it can be determined whether similar large-angle observations of electron events can be made. Following this, an additional turbulent field meandering can be included in simulations, and the effects on the 3D spatial distribution, timing at multiple spacecraft, and spectra at different spacecraft can be assessed.

6.2 Coronal Radio Imaging

In Chapter 4, the effects of large and small scale density inhomogeneities on the propagation of low frequency radio rays was evaluated, and the subsequent effects on produced images was assessed. To assess this, a Monte-Carlo ray tracing simulation of radio transport from a flare site to an observer at 1 AU was built, with images and lightcurves being reproduced from the point of view of the observer. Two different density fluctuation forms were considered: isotropic and anisotropic fluctuations, where the probability of scattering along the radial spatial direction was either equal to, or less than the probability of scattering orthogonal to the radial direction. Further to this, three different background electron density models were considered; mimicking a featureless (symmetric) corona, a streamer, and a coronal hole.

By tracking the apparent radio source properties seen by an observer at 1 AU, it was found that a general increase in source area and inwards radial motion is observed at all times for the symmetric and isotropic transport model. The symmetric and anisotropic model was seen to produce similar burst durations and apparent source motion, but featured a greatly expanded apparent source, with more rapid growth. Similar to the symmetric models, the two asymmetric density models featured apparent source expansion at all times, with the coronal hole model producing more larger sources with rapid growth due to the trapping of radio rays. However, unlike the symmetric

models, a variety of apparent source motion directions was observed in both asymmetric models, with both inwards and outwards radial motion observed. By comparing results to observations of outwards radial motion by [Kontar et al. \(2017\)](#) (Chapter 3), it was concluded that asymmetric density models are required to explain this motion, meaning that simpler density models typically used in simulations (e.g. by [Steinberg et al., 1971](#); [Thejappa et al., 2007](#); [Li et al., 2008](#)) are not applicable for modelling radio bursts at these heights.

While the work presented here focusses on a single frequency burst, propagation effects on bursts of all frequencies (up to ~ 120 MHz, where the thick solar atmosphere absorbs much of the outgoing emission) can be simulated. Preliminary work looking into the frequency dependant apparent source size has been performed (Figure 6.1). The scattering level was kept constant and the frequency range was changed to $f \in [15, 100]$ MHz. For each frequency bin, the a time-integrated image was produced, and the source parameters were extracted via a 2D Gaussian fit to data. It was seen that the apparent source size roughly scales as $1/f$, constant across all viewing angles simulated. In future, this relationship could be tested via comparison with multiple further high resolution type-III radio images. It could also be tested what effects anisotropic scattering and asymmetric density profiles have on this relationship.

The downside of the simulations used here is the large parameter space available, with no definite density profile or fluctuation level profile available for constraint. Future work could look into using these simulations in conjunction with further high resolution observations, in order to constrain both the density fluctuation level and the background density profile. By simulating the apparent expansion of a transient point source outside the corona (e.g. the Crab Nebula; [Sasikumar Raja et al., 2016](#)), the resultant simulated radio images can be directly compared with observations, and restrictions on the density fluctuation level can be made. Alternatively, with density fluctuation estimates (e.g. by direct sampling of the background density from future missions travelling close to the Sun), a combination of simulated and real images can potentially be used to deconvolve the effects of scattering from an image, revealing the true source properties.

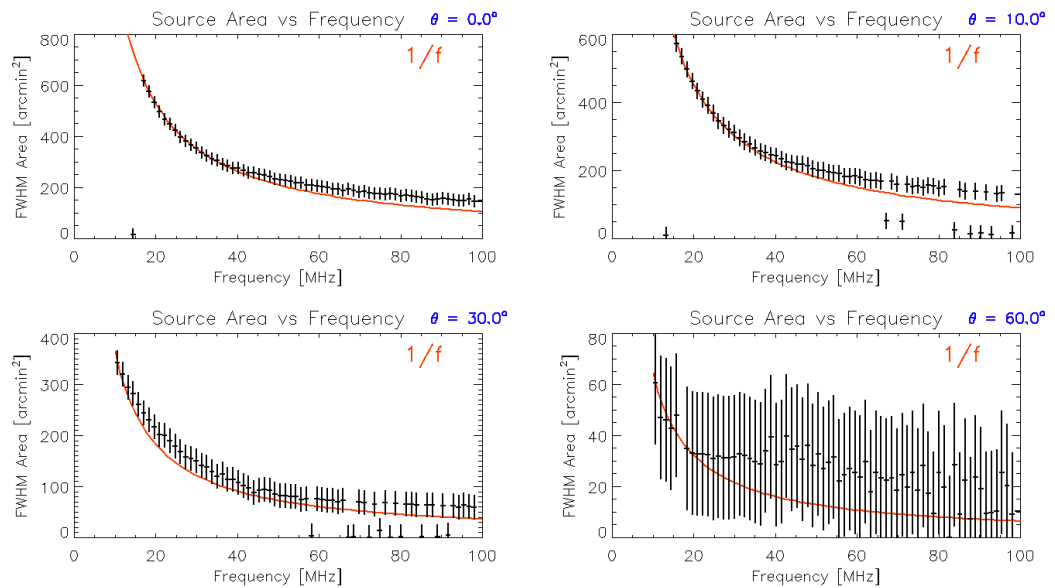


Figure 6.1: Apparent source area as a function of frequency, as viewed from angles of $\theta = [0^\circ, 10^\circ, 30^\circ, 60^\circ]$ (top left, top right, bottom left, bottom right, respectively). The black points show FWHM source area, and the red line shows an inverse frequency fit. The simulation was run with fluctuation level $\epsilon = 8\%$.

6.3 Heliospheric Radio Multilateration

Finally, in Chapter 5, the passage of interplanetary type-III radio bursts was simulated, with the aim of comparing multilaterated source positions to both the true source location and observations of low-frequency type-III bursts. A multilateration technique was used to locate 24 low frequency bursts, and it was found that observed radio sources appear to lie $\sim 4 - 6\times$ further from the Sun than predicted (e.g. by density models derived by Parker, 1958; Leblanc et al., 1998), similar to a study by Krupar et al. (2014).

Using identical methods, the positions of simulated low-frequency sources were determined, and the apparent positions were compared to the true source positions. Similar to observations, a consistent outwards shift of the apparent source relative to the true source was found, with increased density fluctuation level producing larger differences. Within the propagation models used, a $\delta n_e/n_e = 10\%$ fluctuation level is required to match observations, within observational constraints (Celnikier et al.,

1983).

The source velocity was calculated directly through tracking the multilaterated source, and derived velocities were compared with source speeds inferred from the frequency drift rate. Both methods were found to agree, although the inferred source speed was found to be strongly dependent upon the density model used. The same methods were applied to multilaterated simulated sources and simulated dynamic spectra, but the derived source speeds were only found to agree for low fluctuation level. For the highest fluctuation level, it was found that the source speed inferred from the dynamic spectrum was significantly lower than that obtained directly from source positions. However, the time resolution of the simulated lightcurves was generally higher than that for observed bursts, leading to a large increase in uncertainties for directly obtained observed source positions. Future missions featuring higher time resolution receivers could solve this problem, allowing for better comparison of simulations and observations.

In future, it will be of interest to use simulations such as this with spacecraft travelling out of the ecliptic plane, allowing for a fully 3D positioning of radio sources with a reduction in position uncertainty. Further to this, the multilateration technique used here could be applied to the tracking of type-II radio bursts (as in [Martínez-Oliveros et al., 2015](#)). By comparing the peak emission position of a type-II burst with CME positions found through white light imaging, an understanding of the type-II emission location within a CME can be made.

6.4 Closing Statement

The work presented within this thesis can be summarised thusly: given the current understanding of turbulence within the inner heliosphere, it is likely that all particle and radio populations detected at Earth have been strongly modified during transport, complicating the evaluation of the populations present within a solar flare. Through the combination of numerical simulations and observations, the level of these effects has been assessed, and a deconvolution of transport and source effects has begun. The

attempt to precisely probe the electron population in a solar flare is a complicated process, and much more work is required to allow for exact modelling of the solar population.

Bibliography

- Agueda, N., & Lario, D. 2016, *ApJ*, 829, 131
- Agueda, N., Lario, D., Vainio, R., et al. 2009, *A&A*, 507, 981
- Agueda, N., Vainio, R., Lario, D., & Sanahuja, B. 2008, *ApJ*, 675, 1601
- Agueda, N., Klein, K.-L., Vilmer, N., et al. 2014, *A&A*, 570, A5
- Alissandrakis, C. E., Kundu, M. R., & Shevgaonkar, K. R. 1991, *A&A*, 251, 276
- Alissandrakis, C. E., Patsourakos, S., Nindos, A., & Bastian, T. S. 2017, *A&A*, 605, A78
- Alvarez, H., & Haddock, F. T. 1973, *Sol. Phys.*, 29, 197
- Ambastha, A. 2010, *Solar Interior*, ed. N. Gopalswamy, S. Hasan, & A. Ambastha (Berlin, Heidelberg: Springer Berlin Heidelberg), 15
- Arzner, K., & Magun, A. 1999, *A&A*, 351, 1165
- Aschwanden, M. J. 2005, *Physics of the Solar Corona. An Introduction with Problems and Solutions* (2nd edition)
- Aschwanden, M. J., Caspi, A., Cohen, C. M. S., et al. 2017, *ApJ*, 836, 17
- Bale, S. D., Goetz, K., Harvey, P. R., et al. 2016, *Space Sci. Rev.*, 204, 49
- Bateman, H. 1918, *Monthly Weather Review*, 46, 4
- Battaglia, M., & Benz, A. O. 2006, *A&A*, 456, 751

- . 2008, *A&A*, **487**, 337
- Battaglia, M., & Kontar, E. P. 2013, *ApJ*, **779**, 107
- Beeck, J., Mason, G. M., Hamilton, D. C., et al. 1987, *ApJ*, **322**, 1052
- Beeck, J., & Wibberenz, G. 1986, *ApJ*, **311**, 437
- Benz, A. O. 2008, *Living Reviews in Solar Physics*, **5**, 1
- Benz, A. O., Bernold, T. E. X., & Dennis, B. R. 1983, *ApJ*, **271**, 355
- Benz, A. O., Jaeggi, M., & Zlobec, P. 1982, *A&A*, **109**, 305
- Benz, A. O., Magun, A., Stehling, W., & Su, H. 1992, *Sol. Phys.*, **141**, 335
- Bethe, H., & Heitler, W. 1934, *Proceedings of the Royal Society of London Series A*, **146**, 83
- Bian, N., Emslie, A. G., & Kontar, E. P. 2012, *ApJ*, **754**, 103
- Bieber, J. W., Matthaeus, W. H., Smith, C. W., et al. 1994, *ApJ*, **420**, 294
- Bird, J. 2014, *Higher Engineering Mathematics, Seventh Edition* (Routledge)
- Blandford, R. D., & Ostriker, J. P. 1978, *ApJ*, **221**, L29
- Bougeret, J. L., & Steinberg, J. L. 1977, *A&A*, **61**, 777
- Bougeret, J.-L., Kaiser, M. L., Kellogg, P. J., et al. 1995, *Space Sci. Rev.*, **71**, 231
- Bougeret, J. L., Goetz, K., Kaiser, M. L., et al. 2008, *Space Sci. Rev.*, **136**, 487
- Brown, J. C. 1971, *Sol. Phys.*, **18**, 489
- Brown, J. C., Emslie, A. G., & Kontar, E. P. 2003, *ApJ*, **595**, L115
- Bruno, R., & Telloni, D. 2015, *The Astrophysical Journal Letters*, **811**, L17
- Budden, K. G. 1988, *The propagation of radio waves: the theory of radio waves of low power in the ionosphere and magnetosphere* (Cambridge University Press)

- Cane, H. V. 2003, [ApJ](#), **598**, 1403
- Cargill, P. J. 1991, [ApJ](#), **376**, 771
- Carley, E. P., Reid, H., Vilmer, N., & Gallagher, P. T. 2015, [A&A](#), **581**, A100
- Cecconi, B., Bonnin, X., Hoang, S., et al. 2008, [Space Sci. Rev.](#), **136**, 549
- Celnikier, L. M., Harvey, C. C., Jegou, R., Moricet, P., & Kemp, M. 1983, [A&A](#), **126**, 293
- Chaizy, P., Pick, M., Reiner, M., et al. 1995, [A&A](#), **303**, 583
- Chandrasekhar, S. 1952, [MNRAS](#), **112**, 475
- Chen, B., Bastian, T. S., Shen, C., et al. 2015, [Science](#), **350**, 1238
- Claßen, H. T., Mann, G., Klassen, A., & Aurass, H. 2003, [A&A](#), **409**, 309
- Coles, W. A., & Harmon, J. K. 1989, [ApJ](#), **337**, 1023
- Condon, J. J. 1997, [PASP](#), **109**, 166
- Daglis, I. A., ed. 2005, *Effects of Space Weather on Technology Infrastructure*, Nato Science Series II (Springer Netherlands)
- Daibog, E. I., Devicheva, E. A., Kurt, V. G., et al. 1981, [Advances in Space Research](#), **1**, 73
- Dalla, S., Marsh, M. S., & Battarbee, M. 2017, [ApJ](#), **834**, 167
- Dasso, S., Milano, L. J., Matthaeus, W. H., & Smith, C. W. 2005, [ApJ](#), **635**, L181
- Datlowe, D. W., & Lin, R. P. 1973, [Solar Physics](#), **32**, 459
- de La Noe, J., & Boischot, A. 1972, [A&A](#), **20**, 55
- Del Zanna, G., Dere, K. P., Young, P. R., Landi, E., & Mason, H. E. 2015, [A&A](#), **582**, A56

- Dennis, B. R. 1985, *Sol. Phys.*, 100, 465
- Doschek, G. A., Warren, H. P., Laming, J. M., et al. 1997, *ApJ*, 482, L109
- Dröge, W. 2000, *Space Sci. Rev.*, 93, 121
- Dröge, W., & Kartavykh, Y. Y. 2009, *ApJ*, 693, 69
- Dröge, W., Kartavykh, Y. Y., Dresing, N., Heber, B., & Klassen, A. 2014, *Journal of Geophysical Research (Space Physics)*, 119, 6074
- Dulk, G. A. 1985, *ARA&A*, 23, 169
- Dulk, G. A., Goldman, M. V., Steinberg, J. L., & Hoang, S. 1987, *A&A*, 173, 366
- Dulk, G. A., Leblanc, Y., Robinson, P. A., Bougeret, J.-L., & Lin, R. P. 1998, *J. Geophys. Res.*, 103, 17223
- Dulk, G. A., & McLean, D. J. 1978, *Sol. Phys.*, 57, 279
- Dulk, G. A., & Suzuki, S. 1980, *A&A*, 88, 203
- Elgaroy, O., & Lyngstad, E. 1972, *A&A*, 16, 1
- Emslie, A. G., Kucharek, H., Dennis, B. R., et al. 2004, *Journal of Geophysical Research (Space Physics)*, 109, A10104
- Emslie, A. G., Dennis, B. R., Shih, A. Y., et al. 2012, *ApJ*, 759, 71
- Ergun, R. E., Larson, D., Lin, R. P., et al. 1998, *ApJ*, 503, 435
- Fainberg, J., Evans, L. G., & Stone, R. G. 1972, *Science*, 178, 743
- Fedorenko, V. N. 1983, *Soviet Ast.*, 27, 640
- Fermi, E. 1949, *Physical Review*, 75, 1169
- Fletcher, L., & Petkaki, P. 1997, *Sol. Phys.*, 172, 267

- Fludra, A., Del Zanna, G., Alexander, D., & Bromage, B. J. I. 1999, *J. Geophys. Res.*, **104**, 9709
- Fokker, A. D. 1965, *Bull. Astron. Inst. Netherlands*, **18**, 111
- Furth, H. P., Killeen, J., & Rosenbluth, M. N. 1963, *The Physics of Fluids*, **6**, 459
- Gamroth, E., Kennedy, J., & Bradley, C. 2011, *Underwater Technology*, **29**, 183
- Gardiner, C. W. 1985, *Springer Series in Synergetics*
- Gary, D. E., & Hurford, G. J. 1989, *Washington DC American Geophysical Union Geophysical Monograph Series*, **54**, 237
- Ginzburg, V. L., & Zhelezniakov, V. V. 1958, *Soviet Ast.*, **2**, 653
- Gontikakis, C., Anastasiadis, A., & Efthymiopoulos, C. 2007, *MNRAS*, **378**, 1019
- Gordovskyy, M., Browning, P., & Vekstein, G. 2010, *The Astrophysical Journal*, **720**, 1603
- Griffiths, D. J. 1962, *Introduction to electrodynamics* (Prentice Hall)
- Haggerty, D. K., & Roelof, E. C. 2002, *ApJ*, **579**, 841
- Hamilton, D. C. 1977, *J. Geophys. Res.*, **82**, 2157
- Hamilton, R. J., & Petrosian, V. 1992, *ApJ*, **398**, 350
- Haug, E. 1975, *Sol. Phys.*, **45**, 453
- . 1997, *A&A*, **326**, 417
- Hewish, A., & Wyndham, J. D. 1963, *MNRAS*, **126**, 469
- Hoang, S., & Steinberg, J. L. 1977, *A&A*, **58**, 287
- Hollweg, J. V. 1968, *AJ*, **73**, 972
- Hollweg, J. V., & Harrington, J. V. 1968, *J. Geophys. Res.*, **73**, 7221

- Holman, G. D. 1985, *ApJ*, 293, 584
- Holman, G. D., Sui, L., Schwartz, R. A., & Emslie, A. G. 2003, *ApJ*, 595, L97
- Holman, G. D., Aschwanden, M. J., Aurass, H., et al. 2011, *Space Sci. Rev.*, 159, 107
- James, T., Subramanian, P., & Kontar, E. P. 2017, *MNRAS*, 471, 89
- Jeffrey, N. L. S., & Kontar, E. P. 2011, *A&A*, 536, A93
- Jokipii, J. R. 1966, *ApJ*, 146, 480
- Kerdraon, A., & Delouis, J.-M. 1997, *The nançay radioheliograph*, ed. G. Trotter (Berlin, Heidelberg: Springer Berlin Heidelberg), 192
- Kippenhahn, R., Weigert, A., & Weiss, A. 2012, *Stellar Structure and Evolution*, Second Edition (Springer-Verlag Berlin Heidelberg)
- Klassen, A., Bothmer, V., Mann, G., et al. 2002, *A&A*, 385, 1078
- Kliem, B. 1994, in *International Astronomical Union Colloquium*, Vol. 142, Cambridge University Press, 719
- Koch, H. W., & Motz, J. W. 1959, *Reviews of Modern Physics*, 31, 920
- Kontar, E. P. 2001a, *Sol. Phys.*, 202, 131
- . 2001b, *A&A*, 375, 629
- Kontar, E. P., Bian, N. H., Emslie, A. G., & Vilmer, N. 2014, *ApJ*, 780, 176
- Kontar, E. P., Emslie, A. G., Massone, A. M., et al. 2007, *ApJ*, 670, 857
- Kontar, E. P., & Jeffrey, N. L. S. 2010, *A&A*, 513, L2
- Kontar, E. P., MacKinnon, A. L., Schwartz, R. A., & Brown, J. C. 2006, *A&A*, 446, 1157
- Kontar, E. P., & Reid, H. A. S. 2009, *ApJ*, 695, L140

- Kontar, E. P., Brown, J. C., Emslie, A. G., et al. 2011, *Space Sci. Rev.*, 159, 301
- Kontar, E. P., Yu, S., Kuznetsov, A. A., et al. 2017, *Nature Communications*, 8, 1515
- Koutchmy, S., & Livshits, M. 1992, *Space Sci. Rev.*, 61, 393
- Kramers, H. A. 1923, *The London, Edinburgh, and Dublin Philosophical Magazine and Journal of Science*, 46, 836
- Krucker, S., Kontar, E. P., Christe, S., & Lin, R. P. 2007, *ApJ*, 663, L109
- Krucker, S., Larson, D. E., Lin, R. P., & Thompson, B. J. 1999, *ApJ*, 519, 864
- Krucker, S., Oakley, P. H., & Lin, R. P. 2009, *ApJ*, 691, 806
- Krupar, V., Kontar, E. P., Soucek, J., et al. 2015, *A&A*, 580, A137
- Krupar, V., Maksimovic, M., Santolik, O., Cecconi, B., & Kruparova, O. 2014, *Sol. Phys.*, 289, 4633
- Kundu, M. R., Bobrowsky, M., & Velusamy, T. 1981, *ApJ*, 251, 342
- Kunstmann, J. E. 1979, *ApJ*, 229, 812
- Labrum, N. R., & Stewart, R. T. 1970, *Proceedings of the Astronomical Society of Australia*, 1, 316
- Laitinen, T., Dalla, S., & Marsh, M. S. 2013, *ApJ*, 773, L29
- Laitinen, T., Kopp, A., Effenberger, F., Dalla, S., & Marsh, M. S. 2016, *A&A*, 591, A18
- Lasuik, J., Fiege, J. D., & Shalchi, A. 2017, *Advances in Space Research*, 59, 722
- Leblanc, Y., Dulk, G. A., & Bougeret, J.-L. 1998, *Sol. Phys.*, 183, 165
- Leblanc, Y., Kuiper, T. B. H., & Hansen, S. F. 1974, *Sol. Phys.*, 37, 215

- Li, B., Cairns, I. H., & Robinson, P. A. 2008, *Journal of Geophysical Research (Space Physics)*, **113**, A06105
- . 2011a, *ApJ*, **730**, 21
- . 2011b, *ApJ*, **730**, 20
- . 2012, *Sol. Phys.*, **279**, 173
- Lin, R. P. 1974, *Space Sci. Rev.*, **16**, 189
- . 1985, *Sol. Phys.*, **100**, 537
- Lin, R. P., Potter, D. W., Gurnett, D. A., & Scarf, F. L. 1981, *ApJ*, **251**, 364
- Lin, R. P., Anderson, K. A., Ashford, S., et al. 1995, *Space Sci. Rev.*, **71**, 125
- Lin, R. P., Dennis, B. R., Hurford, G. J., et al. 2002, *Sol. Phys.*, **210**, 3
- Loi, S. T., Cairns, I. H., & Li, B. 2014, *ApJ*, **790**, 67
- Machado, M. E., Emslie, A. G., & Brown, J. C. 1978, *Sol. Phys.*, **58**, 363
- MacKinnon, A. L., & Craig, I. J. D. 1991, *A&A*, **251**, 693
- Maksimovic, M., Bale, S., Chust, T., et al. 2017, in AAS/Solar Physics Division Meeting, Vol. 48, AAS/Solar Physics Division Meeting, 110.05
- Mann, G., Jansen, F., MacDowall, R. J., Kaiser, M. L., & Stone, R. G. 1999, *A&A*, **348**, 614
- Martínez-Oliveros, J. C., Lindsey, C., Bale, S. D., & Krucker, S. 2012, *Sol. Phys.*, **279**, 153
- Martínez-Oliveros, J. C., Raftery, C., Bain, H., et al. 2015, *Sol. Phys.*, **290**, 891
- Mazur, J. E., Mason, G. M., Dwyer, J. R., et al. 2000, in *American Institute of Physics Conference Series*, Vol. 528, *Acceleration and Transport of Energetic Particles*

- Observed in the Heliosphere, ed. R. A. Mewaldt, J. R. Jokipii, M. A. Lee, E. Möbius, & T. H. Zurbuchen, 47
- McLean, D. J., & Labrum, N. R. 1985, Solar radiophysics: Studies of emission from the sun at metre wavelengths
- Mekhaldi, F., Muscheler, R., Adolphi, F., et al. 2015, *Nature Communications*, 6, 8611
- Mel’Nik, V. N., Konovalenko, A. A., Abranin, E. P., et al. 2005, *Astronomical and Astrophysical Transactions*, 24, 391
- Melnik, V. N., Konovalenko, A. A., Rucker, H. O., et al. 2011, *Sol. Phys.*, 269, 335
- Mel’Nik, V. N., Lapshin, V., & Kontar, E. 1999, *Sol. Phys.*, 184, 353
- Melrose, D. B. 1980a, Plasma astrophysics. Nonthermal processes in diffuse magnetized plasmas. (New York: Gordon and Breach, 1980)
- . 1980b, *Space Sci. Rev.*, 26, 3
- . 2017, *Reviews of Modern Plasma Physics*, 1, 5
- Mercier, C., & Chambe, G. 2012, *A&A*, 540, A18
- Miller, J. A., Larosa, T. N., & Moore, R. L. 1996, *ApJ*, 461, 445
- Miller, J. A., Cargill, P. J., Emslie, A. G., et al. 1997, *J. Geophys. Res.*, 102, 14631
- Miyake, F., Nagaya, K., Masuda, K., & Nakamura, T. 2012, *Nature*, 486, 240
- Morosan, D. E., Gallagher, P. T., Zucca, P., et al. 2014, *A&A*, 568, A67
- Mugundhan, V., Hariharan, K., & Ramesh, R. 2017, *Sol. Phys.*, 292, 155
- Nakajima, H., Nishio, M., Enome, S., et al. 1994, *IEEE Proceedings*, 82, 705
- Newkirk, Jr., G. 1961, *ApJ*, 133, 983

- Palmer, I. D. 1982, *Reviews of Geophysics and Space Physics*, 20, 335
- Parker, E. N. 1958, *ApJ*, 128, 664
- Parks, G. K., & Winckler, J. R. 1969, *ApJ*, 155, L117
- Podesta, J. J., Roberts, D. A., & Goldstein, M. L. 2007, *ApJ*, 664, 543
- Press, W. H., Flannery, B. P., & Teukolsky, S. A. 1986, *Numerical recipes. The art of scientific computing* (Cambridge University Press)
- Priest, E. R., & Forbes, T. G. 2002, *A&A Rev.*, 10, 313
- Pryadko, J. M., & Petrosian, V. 1997, *ApJ*, 482, 774
- . 1998, *ApJ*, 495, 377
- . 1999, *ApJ*, 515, 873
- Qin, G., & Shalchi, A. 2009, *ApJ*, 707, 61
- Ragot, B. R. 2006, *ApJ*, 653, 1493
- Ratcliffe, H., & Kontar, E. P. 2014, *A&A*, 562, A57
- Reames, D. 2017, *Solar Energetic Particles: A Modern Primer on Understanding Sources, Acceleration and Propagation* (Springer International Publishing)
- Reid, H. A. S., & Kontar, E. P. 2010, *ApJ*, 721, 864
- . 2013, *Sol. Phys.*, 285, 217
- . 2015, *A&A*, 577, A124
- . 2017, *A&A*, 606, A141
- Reid, H. A. S., & Ratcliffe, H. 2014, *Research in Astronomy and Astrophysics*, 14, 773
- Reid, H. A. S., & Vilmer, N. 2017, *A&A*, 597, A77

- Reiner, M. J., Fainberg, J., Kaiser, M. L., & Stone, R. G. 1998, *J. Geophys. Res.*, **103**, 1923
- Reiner, M. J., Goetz, K., Fainberg, J., et al. 2009, *Sol. Phys.*, **259**, 255
- Rempel, M. 2011, Solar Convection Zone Dynamics, ed. M. P. Miralles & J. Sánchez Almeida, 23
- Riddle, A. C. 1972, Proceedings of the Astronomical Society of Australia, 2, 98
- Roelof, E. C. 1969, in *Lectures in High-Energy Astrophysics*, ed. H. Ögelman & J. R. Wayland, 111
- Ruiz, M. E., Dasso, S., Matthaeus, W. H., Marsch, E., & Weygand, J. M. 2011, *Journal of Geophysical Research (Space Physics)*, **116**, A10102
- Saint-Hilaire, P., Vilmer, N., & Kerdraon, A. 2013, *ApJ*, **762**, 60
- Saito, K., & Owaki, N. 1967, *PASJ*, **19**, 535
- Saito, K., Poland, A. I., & Munro, R. H. 1977, *Sol. Phys.*, **55**, 121
- Sasikumar Raja, K., Ingale, M., Ramesh, R., et al. 2016, *Journal of Geophysical Research (Space Physics)*, **121**, 11
- Schlickeiser, R. 1989, *ApJ*, **336**, 243
- Schlickeiser, R., & Miller, J. A. 1998, *ApJ*, **492**, 352
- Schwartz, R. A., Csillaghy, A., Tolbert, A. K., et al. 2002, *Sol. Phys.*, **210**, 165
- Shalchi, A. 2006, *A&A*, **448**, 809
- Sheridan, K. V., Labrum, N. R., & Payten, W. J. 1973, *IEEE Proceedings*, **61**, 1312
- Sheridan, K. V., Labrum, N. R., Payten, W. J., Nelson, G. J., & Hill, E. R. 1983, *Sol. Phys.*, **83**, 167
- Shibata, K., & Magara, T. 2011, *Living Reviews in Solar Physics*, **8**, 6

- Shimojo, M., Bastian, T. S., Hales, A. S., et al. 2017, *Solar Physics*, **292**, 87
- Smith, D. F., & Davis, W. D. 1975, *Sol. Phys.*, **41**, 439
- Smith, D. M., Lin, R. P., Turin, P., et al. 2002, *Sol. Phys.*, **210**, 33
- Spangler, S. R. 2002, *ApJ*, **576**, 997
- Stappers, B. W., Hessels, J. W. T., Alexov, A., et al. 2011, *A&A*, **530**, A80
- Steinberg, J. L., Aubier-Giraud, M., Leblanc, Y., & Boischot, A. 1971, *A&A*, **10**, 362
- Steinberg, J. L., Hoang, S., & Dulk, G. A. 1985, *A&A*, **150**, 205
- Stewart, R. T. 1974, *Sol. Phys.*, **39**, 451
- Stix, M. 2004, *The Sun: An Introduction* (Springer-Verlag Berlin Heidelberg New York)
- Sturrock, P. A. 1964, *NASA Special Publication*, **50**, 357
- Sukhodolov, T., Usoskin, I., Rozanov, E., et al. 2017, *Scientific Reports*, **7**
- Suzuki, S., & Dulk, G. A. 1985, *Bursts of Type III and Type V*, ed. D. J. McLean & N. R. Labrum, 289
- Takakura, T., & Shibahashi, H. 1976, *Sol. Phys.*, **46**, 323
- Thejappa, G., & Kundu, M. R. 1994, *Sol. Phys.*, **149**, 31
- Thejappa, G., & MacDowall, R. J. 2010, *ApJ*, **720**, 1395
- Thejappa, G., MacDowall, R. J., & Bergamo, M. 2012, *Journal of Geophysical Research (Space Physics)*, **117**, A08111
- Thejappa, G., MacDowall, R. J., & Kaiser, M. L. 2007, *ApJ*, **671**, 894
- Thompson, M. J., Toomre, J., Anderson, E. R., et al. 1996, *Science*, **272**, 1300
- Ulwencreutz, E. L. 2008, *The Angle-Saxon Chronicle: AD 1 – AD 1154* (Lulu.com)

- Usoskin, I. G., Kromer, B., Ludlow, F., et al. 2013, *A&A*, 552, L3
- van de Hulst, H. C. 1950, *Bull. Astron. Inst. Netherlands*, 11, 135
- van Haarlem, M. P., Wise, M. W., Gunst, A. W., et al. 2013, *A&A*, 556, A2
- Vocks, C., & Mann, G. 2009, *A&A*, 502, 325
- Wang, Y., & Qin, G. 2016, *ApJ*, 820, 61
- Weber, R. R., Fitzenreiter, R. J., Novaco, J. C., & Fainberg, J. 1977, *Sol. Phys.*, 54, 431
- Wedemeyer, S., Bastian, T., Brajša, R., et al. 2016, *Space Science Reviews*, 200, 1
- Wild, J. P. 1967, *Proceedings of the Astronomical Society of Australia*, 1, 38
- Wild, J. P., & McCready, L. L. 1950, *Australian Journal of Scientific Research A Physical Sciences*, 3, 387
- Wild, J. P., Murray, J. D., & Rowe, W. C. 1954, *Australian Journal of Physics*, 7, 439
- Witham, G. B. 1974, *Linear and Non-linear Waves* (New York: Wiley)
- Wohlmuth, R., Plettemeier, D., Edenhofer, P., et al. 2001, *Space Sci. Rev.*, 97, 9
- Wood, P., & Neukirch, T. 2005, *Solar Physics*, 226, 73
- Zaitsev, V. V., Mityakov, N. A., & Rapoport, V. O. 1972, *Sol. Phys.*, 24, 444
- Zharkova, V. V., & Gordovskyy, M. 2005, *Monthly Notices of the Royal Astronomical Society*, 356, 1107
- Zharkova, V. V., Arzner, K., Benz, A. O., et al. 2011, *Space Sci. Rev.*, 159, 357
- Zheleznyakov, V. V., & Zaitsev, V. V. 1970a, *Soviet Ast.*, 14, 47
- . 1970b, *Soviet Ast.*, 14, 250